Study of Lens Arrays for Radiative Near Field Communication in the H-Band

Junyao Tan

谭钧耀

Student number: 5519985

Supervisor: Prof. dr. Nuria Llombart, N.E. Beschoor Plug

Faculty of Electrical Engineering, Mathematics and Computer Science

Delft University of Technology, The Netherlands

24 November 2023

Preface

This master thesis explores the capacity of MIMO arrays for communication in the radiative near field through antenna design. This research applies an in-house MATLAB model based on free space Green's function to calculate the channel matrix, revealing the potential increase of capacity through the use of incoherent arrays with directive antennas in the incoherent range without the need for interference cancellation.

The optimization of the equivalent aperture current and the design of lens antennas are the key points in realizing the ultimate goal of maximizing the capacity between antenna arrays. The accuracy of the channel matrix from the MATLAB model and the performance of the designed lens antennas are validated through full-wave simulation using CST. Furthermore, the internal reflections between the arrays are studied, offering solutions to mitigate the effects of the reflections for future array designs.

This work serves as a feasibility study, providing sufficient confidence in the application of communication systems in the radiative near field without the need for signal processing (e.g. interference cancellation, multi-path cancellation, etc.). Furthermore, the methodology in this thesis offers insights for future antenna designs for different applications. In summary, this study proposes and validates a potential solution for the design of next-generation communication systems.

谭钧耀

Junyao Tan

Delft, November 2023

Acknowledgements

First of all, I would like to thank my supervisor prof. dr. Nuria Llombart for her greatest guidance throughout this year. Despite your busy schedule, you always made efforts to meet with me and patiently answered my questions, sharing your experiences in electromagnetic fields that sparked my ideas.

The sincerest thank you goes to my daily supervisor, Nina Beschoor Plug. Whenever I needed help, you were there. Your support played a crucial role throughout my thesis journey, and your patient and meticulous guidance significantly influenced my academic and research growth. Special thanks for your generously sharing codes and research notes, laying the foundation for much of the content in Chapter 2 of this thesis report.

I also own a thank you to Sjoerd Bosma and Huasheng Zhang for their assistance in antenna design, model construction, and thesis writing.

Additionally, I'd like to thank all the professors in the Terahertz Sensing group for providing interesting and high-quality courses. Your courses sparked my interest in electromagnetic field studies, providing the groundwork for my research.

Finally, thanks to the entire Terahertz Sensing group for creating a relaxed yet cheerful academic atmosphere. I will never forget the lunches, coffees, and the memories in this year.

Study of Lens Arrays for Radiative Near Field Communication in the H-band

This thesis is submitted in partial fulfilment of the requirements for the degree of

MASTER OF SCIENCE

in

ELECTRICAL ENGINEERING

by

Junyao Tan

The work presented in this thesis was performed at:

Terahertz Sensing Group
Department of Microelectronics
Faculty of Electrical Engineering, Mathematics and Computer Science
Delft University of Technology

DELFT UNIVERSITY OF TECHNOLOGY

DEPARTMENT OF ELECTRICAL ENGINEERING

The undersigned herby certify that they have read and recommended to the Faculty of Electrical Engineering, Mathematics and Computer Science for acceptance the thesis entitled "**Study of Len Arrays for Radiative Near Field Communication in the H-band**" by **Junyao Tan** in partial fulfilment of the requirements for the degree of Master of Science.

Dated: November 24, 2023

Chair: _____

Prof. dr. Nuria Llombart

Committee Member: _____

Prof. dr. Andrea Neto

_____

Prof. dr. Marjan Popov

Contents

1 Introduction

In our modern world, the demand for fast data rates is gradually increasing, which motivates us to design a communication system with higher potential capacity. To meet high bit rates, an effective way is to use a higher frequency band in communication [1], because this will give us more spectrum resources. The Institute of Electrical and Electronics Engineers (IEEE) has recently approved a new frequency band known as the H-band in IEEE 802.15.3d standard [2]. The H-band frequency spans from 252GHz to 325GHz, offering around 70GHz bandwidth of spectrum resources. Designing a wireless communication system in this frequency band has become an interesting research topic [3][4][5][6][7]. The antenna, as the transition terminal between the guided and wireless signal, is a key component in a communication system. Its research and design have naturally become a hot spot [8][9][10].

In current communication systems (5G), using a Multiple-Input Multiple-Output (MIMO) antenna array is a technological solution[11][12]. It increases the capacity in a given bandwidth by allowing multiple independent channels to transmit simultaneously over different channels. However, because of the physical limits associated with the radiation and propagation of Electromagnetic waves, the signals can never be independent. This is because the received signals by the multiple antennas will have a certain degree of interference with the other signals transmitted over the same channel. This signal interference can significantly influence the communication data quality. The amount of signal interference is particularly significant in the far field when the antennas are located in the line of sight and array elements are very close. In that case, the signals received (main and interference) can have the same amplitude level. To reduce this interference, existing methods usually rely on complex signal processing techniques, such as singular value decomposition (SVD) precoding, which increases the complexity of the system, especially under high bit rate and high-frequency conditions. This complexity is affordable in the 5G frequency band. But when we need to achieve higher frequencies, such as H-band, there is currently no hardware capable of reaching the required data processing in real-time and the front-end requirements in terms of linearity, noise, and power [13][14].

In [13], it was proposed to use high directivity antennas to form MIMO arrays and communicate in the radiative near field to have a good suppression of the interference directly from the radiation point of view. Antennas operating at high frequencies can reach high directivity with considerably small physical size, which brings us the possibility of developing compact communications systems with very high capacities. At high frequencies, high directivity antennas lead easily to links operating in the radiative near field. Additionally, the high directivity antennas have collimated beams in the radiative near-field, which means most of the energy is received by the desired receiver antenna, increasing the co-coupling and reducing the interference to other signals transmitted over the same near-field channel. This approach only depends on the antenna design, giving us the possibility of achieving low interference without complex data processing, finally resulting in high capacity.

Besides the high potential for interference suppression, another advantage of this approach is its ability to manage multi-path signals and the possibility of realizing secure communications. In communication systems, the impact of multi-path movements is significant. The multi-path signals are caused by the reflections on the environment (e.g. close-by objects), where the signals undergo a different propagation path concerning to the Line of Sight (LoS) signal, arriving at the receiver port at a different instant of time causing a multi-path interference. This can significantly decrease the capacity. Generally, these multi-path signals are from environment reflections and cannot be suppressed physically. At low frequencies, these multi-path effects have some statistical distributions in the time domain, so signal processing techniques are commonly used to cancel them. As introduced before, the beam in the radiative near field is collimated, and most of the energy is captured by the antenna receiving array, with a minor spill of the energy to the external environment. Consequently, multi-path signals are

dominated by internal reflections (reflections from antenna array), rather than external environmental reflections. So, by properly designing the antenna array to decrease the reflections, we can reduce the multi-path effects. Consequently, the complexity needed for signal processing is significantly reduced, and one can envision communication systems operating at very high speeds in the order of Terabytes per second (TBps) [13].

1.1 Communication Scenario

In this thesis, we chose to study a 2×2 MIMO system operating in the LoS where the transmitter and receiver arrays are assumed to be aligned. The goal is to study the effect of the interference, ways of reducing it, and providing an estimation of the bit-rate data capacity. As the object of study, we will focus on lens antennas. This type of antenna can provide high gain and allows easy adjustment of the equivalent current distribution. Although there are currently no specific usage scenarios and design requirements, this choice provides us with the feasibility of this study. The configuration of this scenario is shown in Figure 1.1.

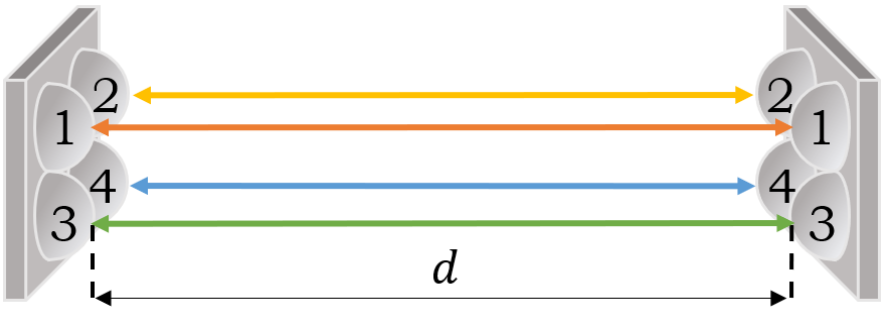

Figure 1.1 The communication scenario in this thesis

In Figure 1.1, the transmitter (Tx) array and the receiver (Rx) array face each other and are separated by a link distance d. There are 4 antennas in each array, and each antenna in the Tx and Rx arrays is numbered in the same way depending on their location in the x/y-plane, therefore facing each other. In this figure, four different communication paths can be identified between each Tx and Rx antenna of the same number.

As for the frequency band, we focus on the recently introduced band by IEEE for LoS communications: $f \in [235GHz, 305GHz]$. This frequency band has 70GHz of bandwidth corresponding to a 20% relative bandwidth. Importantly, the antenna design can be adapted to different frequencies through scaling, which allows us to extend this research to the H-band easily. In this case, the center frequency $f_0 = 270GHz$, and its corresponding wavelength is $\lambda_0 = \frac{c_0}{f_0} = 1.1mm$, where c_0 is the speed of light in the free space. All the scales in this thesis will be in terms of λ_0.

To maintain the high directivity of the lens antenna with affordable time in simulation, we will choose the diameter of the lens antenna to be $D_l = 6\lambda_0 = 6.7mm$ to form the MIMO array. The far field distance is defined as the distance that has $\frac{\pi}{8}$ phase error, calculated as:

$$d_{ff} = \frac{2D^2}{\lambda_0} \qquad [1.1]$$

In this case, this far field distance $d_{ff} = 80mm$. Since the operation distance is in the radiative near field, we are interested in the distance range $d < 80mm$.

1.2 Problem Statement

This thesis aims to provide a feasibility analysis for a radiative near field communication system using a MIMO array based on lens antennas with interference suppression achieved only through the lens antenna design itself. We will not consider some classical approaches (e.g. signal processing, orthogonal polarization of the lens antenna, etc.), instead, we will only focus on the antenna design to prove the feasibility. Since we are designing the communication system, the design criteria for the interference suppression will be the capacity.

The analysis model of such a problem can be based on equivalent current distributions radiating into free space as described in [13]. In particular, according to the equivalence theorem, the radiation of a lens antenna is modelled as that of the equivalent current on the aperture. Using the equivalent current and the free space Green's functions, we can estimate the channel transfer matrix as described in [13]. This analysis model can give us the coupling level between apertures with a certain current distribution in the radiative near field.

The primary objectives to be addressed in this thesis will be:

- Identify the possible working range for the MIMO array, called the interested range.
- Identify the optimized current distribution that provides the highest capacity in the interested range.
- Study the frequency dependence of this current distribution.
- Design a lens antenna to approximate the optimized current distribution using Geometrical Optics (GO) approximation.
- Evaluate the performance of this lens antenna with the optimized current distribution.
- Validate the results with a full wave simulation in CST introducing a power efficiency term.
- Study the effect of the multiple reflections.

1.3 Thesis Outline

The remaining part of this thesis is structured as follows:

- Chapter 2 introduces the background information related to the evaluation of the transfer matrix using equivalent current distributions and free space Green's functions. The transfer matrix is then used to estimate the theoretical capacity in the considered MIMO system.
- Chapter 3 describes the optimization of the current distribution that maximizes the capacity when multiple signals are being sent simultaneously.
- Chapter 4 describes the design and performance of a lens antenna that generates the optimized current distribution in its aperture. The current design is done using Geometrical Optics and it is used to evaluate the capacity via the estimation of the channel matrix. The lens design is validated via full-wave simulation in CST. As a reference, a lens antenna with uniform current distribution taken from the literature is also evaluated.
- Chapter 5 presents the full wave simulation in CST of a 2×2 link based on lens arrays. Two cases are considered: the lens antennas with uniform current distribution and those with

optimized distributions. These simulations are used to validate the lens antenna design, as well as the analysis tools for estimating the channel transfer matrix.

- Chapter 6 studied the effect of reflections. The reflections are categorized into two types to study: reflections in co-coupling and reflections in interference. Moreover, the source of the reflections is discussed, offering recommendations for future work.
- Chapter 7 concludes this thesis and mentions the future work lines.

2 Radiative Near Field Links

As introduced in Chapter 1, the MIMO antenna array can be used to increase the capacity of a communication system by allowing more signals to be transferred simultaneously. The geometry of the studied scenario is shown in Figure 1.1.

Ideally, this system has four independent channels. However, the actual situation is that it cannot ensured that all channels are received independently and some of the power transmitted by the Tx antennas will be received by the Rx antennas of the other channels.

To assess the capacity of a MIMO system, a matrix to define the transmission between the Tx antennas, $\boldsymbol{x}$, and Rx antennas, $\boldsymbol{y}$, is introduced as $\overline{\overline{H}}$ [15]. The Transfer Function Matrix, and the corresponding channel equations is defined as follows:

$$y = \overline{\overline{H}}x + n \qquad [2.1]$$

Where $\boldsymbol{y}$ is the received signals at Rx's, $\boldsymbol{x}$ is the transmitted signals at Tx's, $\overline{\overline{H}}$ is the channel matrix, and n is the zero-mean complex Gaussian noise. Since this Transfer Function Matrix is defined as the transfer between each channel, we will call this as this Transfer Function Matrix as the channel matrix in the rest of this thesis. Here we have a 2×2 MIMO scenario, with four inputs and four outputs. Therefore, the channel matrix H is a 4×4 matrix. If we expand eq. 2.1, the channel equation will change to:

$$\begin{bmatrix} y_1 \\ y_2 \\ y_3 \\ y_4 \end{bmatrix} = \begin{bmatrix} h_{11} & h_{12} & h_{13} & h_{14} \\ h_{21} & h_{22} & h_{23} & h_{24} \\ h_{31} & h_{32} & h_{33} & h_{34} \\ h_{41} & h_{42} & h_{43} & h_{44} \end{bmatrix} \begin{bmatrix} x_1 \\ x_2 \\ x_3 \\ x_4 \end{bmatrix} + \begin{bmatrix} n_1 \\ n_2 \\ n_3 \\ n_4 \end{bmatrix} \qquad [2.2]$$

Where x_i is the input signal at the i_{th} Tx antenna, y_i is the output signal at the i_{th} Rx antenna and h_{ji} is the coupling between these two antennas. According to the definition of channels, h_{11}, h_{22}, h_{33} and h_{44} are the co-couplings and the rest of them are the interferences. Based on the law of conservation of energy, the coupling level $|h_{ij}|$ is a number between 0 to 1.

Independent channels ideally have an extremely large isolation between them. Therefore, we want to maximize the isolation of these channels so that we can maximize the received power at the desired antenna and minimize the interference in other channels. For link distances corresponding to the radiative near field of both the Tx and Rx antenna $d < d_{ff} = 2D^2/\lambda$, the radiated fields of directive antennas are collimated as there is barely any energy spreading. Therefore, it is possible to exploit spatial multiplexing to create independent channels.

The channel matrix is very important as it gives all the information necessary to express the performance of the array in terms of signal, interference, noise levels, and finally, in terms of a metric that we would like to optimize, capacity.

To calculate the channel matrix and the capacity of the near field links with the lens array, the coupling of the antenna array and its capacity is modelled analytically as described in [13]. We will first model the lens antenna as the equivalence current on its equivalent aperture, described in Section 2.1; then we will introduce how to calculate the coupling in the radiative near field, described in Section 2.2; finally, we will study the channel matrix and calculate the capacity, described in Section 2.3.

2.1 Modelling of Lens Antennas

In this section, we will introduce the modelling of the lens antennas. We will use an equivalent current to replace the behavior of the lens antenna, described in Section 2.1.1, and then evaluate the power efficiency between the lens feed and the equivalent current as described in Section 2.1.2. Finally, we will discuss the modelling of the theoretical currents in Section 2.2.3.

2.1.1 Equivalent Aperture Current

Based on the equivalence theorem, the radiation of the lens antenna can be modelled as the radiation of its equivalent current on the aperture. The aperture of the equivalent current is located just on top of the lens antenna as shown in Figure 2.1.

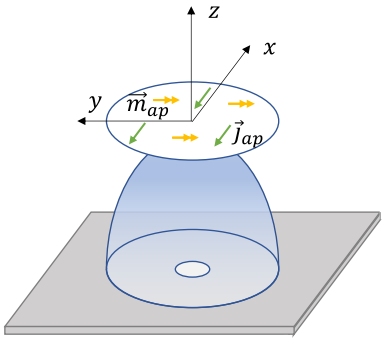

Figure 2.1 Schematic of lens antenna and its equivalent aperture current distribution

The equivalent aperture current distributions can be modelled as a pair of electric and magnetic current as follows:

$$\vec{j}(\vec{\rho}) = \hat{z} \times \vec{h}_{ap}(\vec{\rho})\text{domain}(\vec{\rho}, S_0) \quad [2.3]$$

$$\vec{m}(\vec{\rho}) = \vec{e}_{ap}(\vec{\rho}) \times \hat{z}\text{domain}(\vec{\rho}, S_0) \quad [2.4]$$

where $[\vec{e}_{ap}, \vec{h}_{ap}]$ is the electromagnetic (EM) aperture field radiated by the lens and $domain(\vec{\rho}, S_0)$ is a function that defines the aperture domain, i.e. $domain(\vec{\rho}, S_0) = 1$ when $\vec{\rho} \in S_0$ and is zero otherwise. The aperture field radiated by an electrically large lens antenna towards the broadside can be represented locally by a plane wave with non-uniform aperture distributions where the magnetic field verifies the following condition:

$$\vec{h}_{ap}(\vec{\rho}) = \hat{z} \times \frac{\vec{e}_{ap}(\vec{\rho})}{\zeta_0} \quad [2.5]$$

Therefore the equivalent current can be expressed via distributed coherent Huygens' sources as follows:

$$\vec{j}(\vec{\rho}) = \hat{z} \times \vec{h}_{ap}(\vec{\rho})\text{domain}(\vec{\rho}, S_0) \quad [2.6]$$

$$\vec{m}(\vec{\rho}) = -\vec{h}_{ap}(\vec{\rho})\zeta_0\text{domain}(\vec{\rho}, S_0) \quad [2.7]$$

Where ζ_0 is the free space characteristic impedance.

It is possible to model the transmission of the lens antenna with GO approximation when the lens antenna is electrically large. The aperture of the equivalent current becomes to a circular aperture:

$$\text{domain}(\vec{\rho}, S_0) = circ\left(\vec{\rho}, \frac{D_{ap}}{2}\right) \quad [2.8]$$

Where the diameter D_{ap} is the same as the diameter of the lens antenna D_l. With the equivalence theorem and the GO approximation, the radiation of the lens antenna is modelled as the radiation of the equivalent current on a circular aperture on top of the lens antenna. See 4.2.1 to find more details about the GO approximation.

Then we can replace Figure 2.1 with Figure 2.2, and we can evaluate the coupling between the lens antennas via the coupling between equivalent aperture currents.

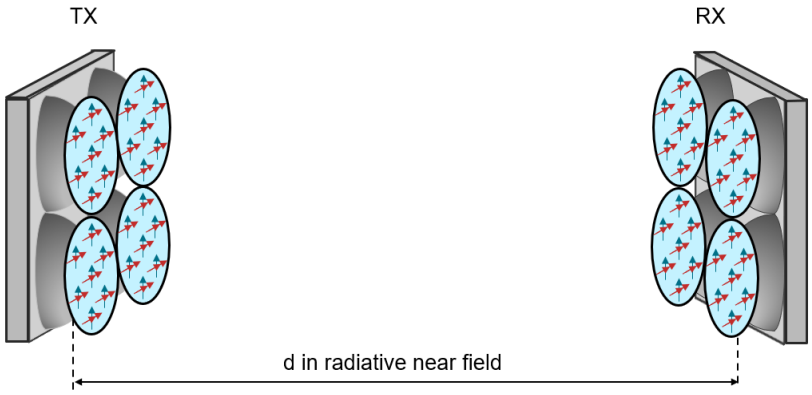

Figure 2.2 Schematic of lens array Tx-Rx coupling using equivalent aperture currents

2.1.2 Lens Radiation Efficiency

To represent the coupling and interference levels properly, the current distributions should also be representative in terms of power radiated by the feed. The radiation efficiency of the lens antenna represents the power on the aperture with respect to (w.r.t.) that is given by the lens feed. For any lens antenna design, the radiation efficiency η_{rad} is less than 100%. The radiation efficiency is therefore defined as the ratio of the radiated power to the input power:

$$\eta_{rad} = \frac{P_{rad}}{P_{in}} \qquad [2.9]$$

Where P_{ap} is the power radiated by the lens antenna on the aperture, and P_{in} is the input power to the lens antenna. This efficiency will be calculated in Sections 4.3.3.2 and 4.4.3.2.

2.1.3 Normalization of the Current Distribution

Since we modelled the lens antenna as the equivalent current on the circular domain, we can now study the theoretical current distribution and find the theoretical current distribution as the target of the antenna design. The theoretical current distribution considered in this thesis is the uniform as a reference, and then the focused radial prolate spheroidal wave functions as introduced in [16] and the focused Gaussian beam will be studied in Chapter 3. To study these current distributions, we need to have a common expression and normalization of the current. For all cases, we assume a normalization of the magnetic field to directly obtain the impedance values when evaluating the coupling between apertures in Section 2.2.3. the normalization is the following:

$$\vec{h}_{ap}(\vec{\rho}) = \frac{I_0}{D_{ap}} f(\vec{\rho})\hat{y} \qquad [2.10]$$

Where $f(\vec{\rho})$ represents the distribution normalized to one. Therefore, the electric and magnetic aperture currents can be defined as:

$$\vec{j}(\vec{\rho}) = -\frac{I_0}{D_{ap}}\vec{f}(\vec{\rho})circ\left(\vec{\rho},\frac{D_{ap}}{2}\right)\hat{x} \quad [2.11]$$

$$\vec{m}(\vec{\rho}) = -\zeta_0\frac{I_0}{D_{ap}}\vec{f}(\vec{\rho})circ\left(\vec{\rho},\frac{D_{ap}}{2}\right)\hat{y} \quad [2.12]$$

The Fourier Transform (FT) of these currents can be expressed as a function of the FT of the distribution $f(\vec{\rho})$ and the domain function as:

$$\vec{J}(\vec{k}) = -\frac{I_0}{D_{ap}}e^{-jk_0\hat{k}\cdot\vec{r}_i}F(\hat{k}) \quad [2.13]$$

where $F(\hat{k}) = F(k_\rho,\alpha) = F(k_x,k_y) = \iint f(\vec{r}')\text{domain}(\vec{r},S_0)e^{jk_0\hat{k}\cdot\vec{r}}d\vec{r}$, $\vec{k} = k_0\hat{k} = k_x\hat{x} + k_y\hat{y}$, and k_0 is the propagation constant in free space (change with frequency). Therefore, the corresponding FT for all currents can be written compactly as follows:

$$\vec{J}(\vec{k}) = -\frac{I_0}{D_{ap}}e^{-jk_0\hat{r}\cdot\vec{r}_i}F_{tx}(\hat{k})\hat{x} \quad [2.14]$$

$$\vec{M}^i_{tx}(\vec{k}) = -\zeta_0\frac{I_0}{D_{ap}}e^{-jk_0\,\hat{r}\cdot\vec{r}_i}F_{tx}(\hat{k})\hat{y} \quad [2.15]$$

From eq. 2.11, 2.12, 2.14, and 2.15, electric and magnetic the current distributions and its FTs only depend on the distribution $\vec{f}(\vec{\rho})$. This distribution is the term that we need to study and optimize. Here let us show an example of the uniform current distribution.

The uniform current distribution is the ideal current distribution in the far field, providing the maximum directivity with a given size of aperture. The distribution is:

$$f(\vec{\rho}) = 1 \quad [2.16]$$

The amplitude and the phase of this distribution are constant over the aperture domain. This current distribution will be used to evaluate the radiated field, coupling, channel matrix, and the capacity in this chapter as an example.

2.2 Evaluation of the Coupling in the Radiative Near Field

From eq. 2.3 and 2.4, we have represented the lens antenna radiation via an equivalent current on a circular aperture located on top of the lens. In this section, we are going to calculate the coupling between two aperture currents as shown in **Error! Reference source not found.**. The locations of the T x and Rx apertures are arbitrary. We will first show the radiated field, in Section 2.2.1, second we calculate the power radiated as shown in Section 2.2.2, and finally we will show the coupling in Section 2.2.3.

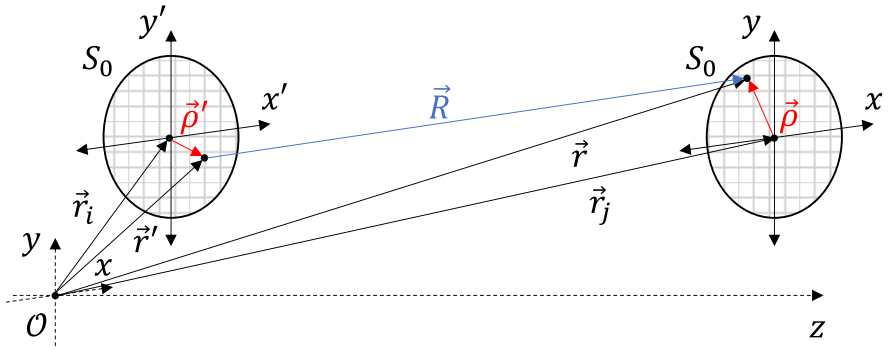

Figure 2.3 Geometry for the evaluation of the coupling between two aperture current distributions

2.2.1 Radiated Field from Arbitrary Current Distribution

We need to calculate the field radiated by the Tx aperture first. The radiated fields $\left[\vec{e}^{i}_{tx}(\vec{r}), \vec{h}^{i}_{tx}(\vec{r})\right]$ from an arbitrary current distribution at an observation point $\vec{r}$ is calculated as the spatial convolution of the equivalent current distribution $\left[\vec{j}^{i}_{tx}(\vec{\rho}'), \vec{m}^{i}_{tx}(\vec{\rho}')\right]$ with the free space Green's function over the equivalent domain S_0:

$$\vec{e}^{i}_{tx}(\vec{r}) = -jk_0\zeta_0 \iint_{S_0} \left(\tilde{I} - \vec{\nabla}\vec{\nabla}\right)\vec{j}^{i}_{tx}(\vec{\rho}')\frac{e^{-jk_0R}}{4\pi R}d\vec{r}' + jk_0 \iint_{S_0} \left(\vec{\nabla}\times\tilde{I}\right)\vec{m}^{i}_{tx}(\vec{\rho}')\frac{e^{-jk_0R}}{4\pi R}d\vec{r}' \qquad [2.17]$$

$$h(\vec{r}) = -\frac{jk_0}{\zeta_0} \iint_{S_0} \left(\tilde{I} - \vec{\nabla}\vec{\nabla}\right)\vec{m}^{i}_{tx}(\vec{\rho}')\frac{e^{-jk_0R}}{4\pi R}d\vec{r}' - jk_0 \iint_{S_0} \left(\vec{\nabla}\times\tilde{I}\right)\vec{j}^{i}_{tx}(\vec{\rho}')\frac{e^{-jk_0R}}{4\pi R}d\vec{r}' \qquad [2.18]$$

The parameters from eq. 2.17 and 2.18 are shown in Figure 2.4, where $\vec{R} = \vec{r} - \vec{r}'$ is the vector from the source point to the observation point, k_0 is the propagation constant in free space.

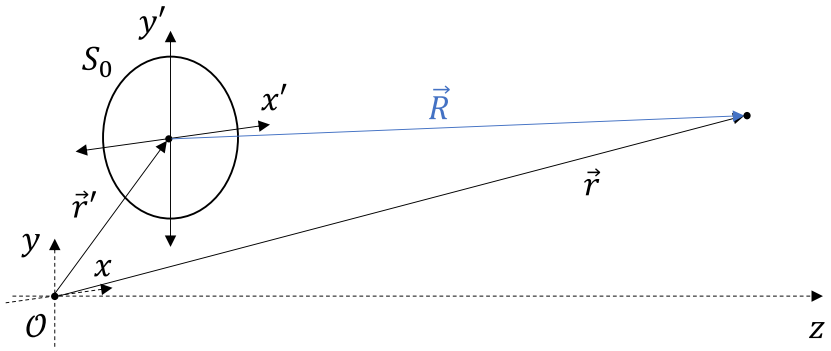

Figure 2.4 Vector definitions for the calculation of the radiated field between two points

In eq. 2.17 and 2.18, for $\vec{R} = \vec{r} - \vec{r}'$, if $R > 1/k_0$, the term in the Green's function can be simplified using $\vec{\nabla} \simeq -jk_0\hat{R}$. This approximation corresponds to using Radiative Green's Function (RGF) for the elementary contributions of eq. 2.17 and 2.18, and can be used when two apertures are located at a separation larger than $1/k_0$, which is appropriate for our interested range. With this approximation, eq. 2.17 and 2.18 can be simplified as:

$$\vec{e}^{i}_{tx}(\vec{r}) = -jk_0\zeta_0 \iint_{S_0} \left(\tilde{I} - \hat{R}\hat{R}\right)\vec{j}^{i}_{tx}(\vec{\rho}')\frac{e^{-jk_0R}}{4\pi R}d\vec{\rho}' + jk_0 \iint_{S_0} \left(\hat{R}\times\tilde{I}\right)\vec{m}^{i}_{tx}(\vec{\rho}')\frac{e^{-jk_0R}}{4\pi R}d\vec{\rho}' \qquad [2.19]$$

$$\vec{h}_{tx}^{i}(\vec{r}) = -\frac{jk_0}{\zeta_0}\iint_{S_0}(\tilde{I}-\hat{R}\hat{R})\vec{m}_{tx}^{i}(\vec{\rho}')\frac{e^{-jk_0R}}{4\pi R}d\vec{\rho}' - jk_0\iint_{S_0}(\hat{R}\times\tilde{I})\vec{j}_{tx}^{i}(\vec{\rho}')\frac{e^{-jk_0R}}{4\pi R}d\vec{\rho}' \quad [2.20]$$

Substitute eq. 2.11 and 2.12 to eq. 2.19 and 2.20:

$$\vec{e}_{tx}^{i}(\vec{r}) = \frac{jk_0\zeta_0 I_0}{D_{ap}}\iint_{S_0}(\tilde{I}-\hat{R}\hat{R})\hat{x}f_{tx}(\vec{\rho}')\frac{e^{-jk_0R}}{4\pi R}d\vec{\rho}' - \frac{jk_0 I_0}{D_{ap}}\iint_{S_0}(\hat{R}\times\tilde{I})\hat{y}f_{tx}(\vec{\rho}')\frac{e^{-jk_0R}}{4\pi R}d\vec{\rho}' \quad [2.21]$$

$$\vec{h}_{tx}^{i}(\vec{r}) = \frac{jk_0 I_0}{D_{ap}}\iint_{S_0}(\tilde{I}-\hat{R}\hat{R})\hat{y}f_{tx}(\vec{\rho}')\frac{e^{-jk_0R}}{4\pi R}d\vec{\rho}' + \frac{jk_0 I_0}{D_{ap}}\iint_{S_0}(\hat{R}\times\tilde{I})\hat{x}f_{tx}(\vec{\rho}')\frac{e^{-jk_0R}}{4\pi R}d\vec{\rho}' \quad [2.22]$$

Eq. 2.19 and 2.20 can be used to calculate the radiated fields of an aperture in all cases (e.g. GO currents, equivalent currents from CST), where eq. 2.21 and 2.22, as a simplification, can only be used to calculate the field radiated by a theoretical current with distribution $f_{tx}(\vec{\rho}')$.

The points on the aperture plane are defined as $\vec{\rho}' = \vec{r}' - \vec{r}_i$, shown in Figure 2.5. This allows us to calculate the radiated field by only defining the position of the apertures $\vec{r}_i$ and $\vec{r}$, then we can automatically have the vector of the points on Tx aperture $\vec{r}_i$ and the vector between the radiating points and the observation points as $\vec{R} = \vec{r} - \vec{r}_i - \vec{\rho}'$. These notations are indicated in Figure 2.5.

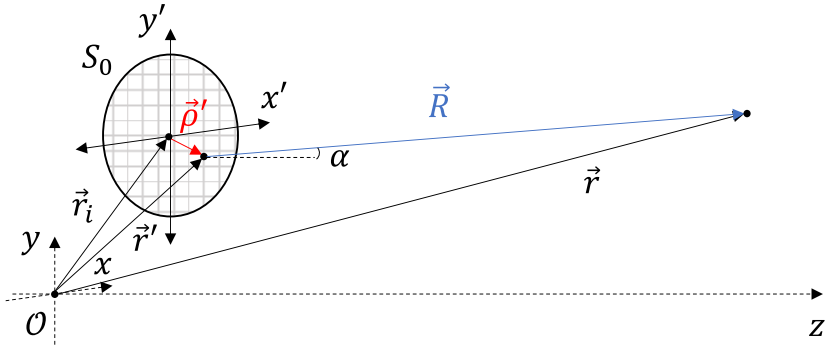

Figure 2.5 Vector definitions on transmitting aperture used for calculating the radiated field in observation point $\vec{r}$

Since we are mainly focusing on the radiative near field coupling in this thesis, this approximation for radiative near field will be used to calculate the radiated field. With eq. 2.21 and 2.22, the field radiated by a uniform current with a circular aperture with $D_{ap} = 6\lambda_0$ is shown in Figure 2.6. It can be observed that the field radiated by the uniform current has several side lobes also in the radiative near field.

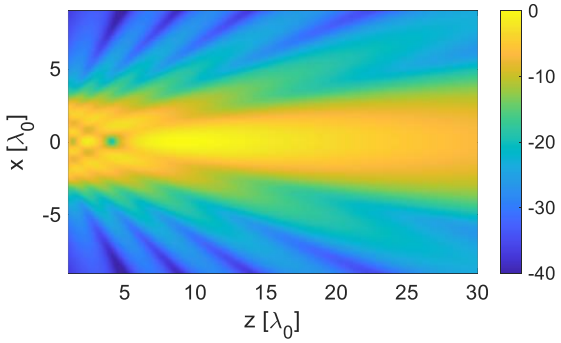

Figure 2.6 Field radiated by a uniform current aperture with $6\lambda_0$ diameter

Even though we are not interested in the far field radiation in this thesis, it is still relevant to calculate it. The far field is helpful to calculate the power radiated by the current source. We will implement some approximations on the expression to simplify the calculation of the fields in the far field.

In the far field, the amplitude term from eq. 2.21 and 2.22 is approximated same:

$$\frac{1}{R} = \frac{1}{|\vec{r} - \vec{r}'|} \approx \frac{1}{|\vec{r} - \vec{r}_i|} \quad [2.23]$$

Where $|\vec{r} - \vec{r}_i|$ is the distance from the observation point to the center of the Tx aperture.

The phase term is simplified as:

$$\vec{R} = |\vec{r} - \vec{r}'| = r - r'(\hat{r}' \cdot \hat{r}) = r - \vec{r}' \cdot \hat{r} \quad [2.24]$$

With these approximation, the expression for the radiated field at the observation point is:

$$\vec{e}^i_{tx}(\vec{r}) = -jk_0\zeta_0 \frac{1}{4\pi R} \iint_{S_0} \vec{J}^i_{tx}(\vec{\rho}') e^{-jk_0 R} d\vec{\rho}' + jk_0(\hat{z} \times \tilde{I}) \frac{1}{4\pi R} \iint_{S_0} \left[\zeta_0 \hat{z} \times \vec{m}^i_{tx}(\vec{\rho}')\right] e^{-jk_0 R} d\vec{\rho}' \quad [2.25]$$

$$\vec{h}^i_{tx}(\vec{r}) = -\frac{jk_0}{\zeta_0} \frac{1}{4\pi R} \iint_{S_0} \left[\zeta_0 \hat{z} \times \vec{J}^i_{tx}(\vec{\rho}')\right] e^{-jk_0 R} d\vec{\rho}' - jk_0(\hat{z} \times \tilde{I}) \frac{1}{4\pi R} \iint_{S_0} \vec{m}^i_{tx}(\vec{\rho}')\, e^{-jk_0 R} d\vec{\rho}' \quad [2.26]$$

Substitute eq. 2.11 and 2.12 to eq. 2.25 and 2.26:

$$\vec{e}^i_{tx}(\vec{r}) = \frac{jk_0\zeta_0 I_0}{D_{ap}} \frac{e^{-jk_0 R}}{2\pi R} F_{tx}(\hat{k})\hat{x} \quad [2.27]$$

$$\vec{h}^i_{tx}(\vec{r}) = \frac{jk_0 I_0}{D_{ap}} \frac{e^{-jk_0 R}}{2\pi R} F_{tx}(\hat{k})\hat{y} \quad [2.28]$$

Where $\vec{F}^i_{tx}(\vec{k})$ is the FT of the source distribution function $\vec{f}(\vec{\rho})$.

Eq. 2.25 and 2.26 can be used to calculate the far field of aperture in all cases (e.g. GO currents, equivalent currents from CST), where eq. 2.27 and 2.28, as a simplification, can only be used to calculate the field radiated by a theoretical currents.

Eq. 2.25 to 2.28 are only validate when an observation point is located in the far field of a transmitting domain if it satisfies the following conditions:

$$R > 10D_{ap} \quad [2.29]$$

$$R > \frac{2D_{ap}^2}{\lambda_0} \quad [2.30]$$

With eq. 2.27, the electric field radiated by the uniform current distribution on $6\lambda_0$ circular aperture in a far field distance $r = 1m$ is shown in Figure 2.7. Since the current distribution is rotationally symmetric, the radiated field is also rotationally symmetric. As a result, the far field pattern in the E plane is only plotted.

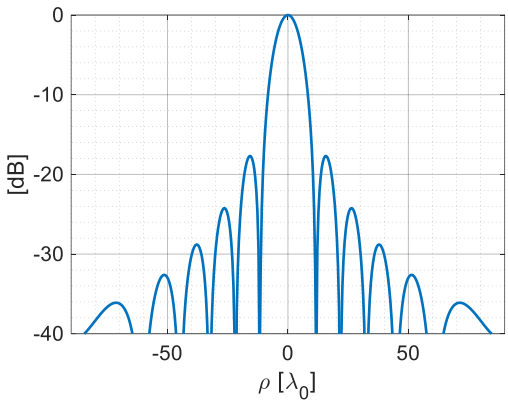

Figure 2.7 The far field pattern of the uniform current with $6\lambda_0$ aperture

2.2.2 Radiated Power from Arbitrary Current Distribution

The radiated fields carry an active average power. This average power can be evaluated via as the Poynting vector as:

$$\vec{S}_{av}(\vec{r}) = \frac{1}{2}\mathcal{R}e\left\{\vec{e}^{i}_{tx}(\vec{r}) \times \left(\vec{h}^{i}_{tx}(\vec{r})\right)^{*}\right\} \quad [2.31]$$

Where $*$ indicate the complex conjugate, and the electric and magnetic fields $\vec{e}^{i}_{tx}(\vec{r})$ and $\vec{h}^{i}_{tx}(\vec{r})$ are the fields radiated by the current. The total power radiated can be calculated as the integral of the Poynting vector on a surface:

$$P_{rad} = \iint_{S} \vec{S}_{av}(\vec{r}) \cdot \hat{n} dS \quad [2.32]$$

It is important to find the surface S to take the integral. An accurate way is to calculate by integrating the Poynting vector over a spherical surface enclosing the aperture with far field radius as follows:

$$P_{rad} = \frac{1}{2\zeta_0}\iint_{4\pi} \left|E_{ff}(\theta,\phi)\right|^2 r^2 \sin\theta \, d\theta d\phi \quad [2.33]$$

However, when the aperture current distribution cannot be FT analytically, this integral will take a long time to calculate the radiated power with eq. 2.32. And this situation happens a lot in antenna design. As a result, this thesis use a simplifier approximation to calculate the radiated power, by integrating the Poynting vector over the aperture plane. This methods is only accurate for the electrically large aperture, and will be more efficient if the FT of the current distribution is not analytically defined. Our case is electrically large since the aperture is with diameter of $D_a = 6\lambda_0$. As a results, we are going to calculate the power with this approach. In this approximation, the power radiated is calculated as:

$$P_{rad} \approx \frac{1}{2}\iint_{S_0} \left[\vec{j}^{i}_{tx}(\vec{\rho}') \times \left(\vec{m}^{i}_{tx}(\vec{\rho}')\right)^{*}\right] \cdot \hat{z} d\vec{\rho}' \quad [2.34]$$

Substitute eq. 2.11 and 2.12 to eq. 2.34, the power of the theoretical currents is calculated as:

$$P_{rad} \approx \frac{\zeta_0 |I_0|^2}{2}\iint_{S_0} |f_{tx}(\vec{\rho}')|^2 d\vec{\rho}' \quad [2.35]$$

Where S_0 is the aperture surface. Eq. 2.34 can used in all cases when we need to calculate the power radiated by the aperture currents (e.g. GO currents, etc.), and eq. 2.35 can be used when we need to calculate the power of theoretical currents with distribution $f_{tx}(\vec{\rho}')$.

2.2.3 Coupling between Two Apertures: Reaction Integral

The coupling coefficient determines the voltage transfer efficiency between two apertures (equivalent to the *S* parameters). Let us start to model the lens antenna in reception, and it is equivalent for transmission. The equivalent circuit of the Rx aperture is shown in Figure 2.8.

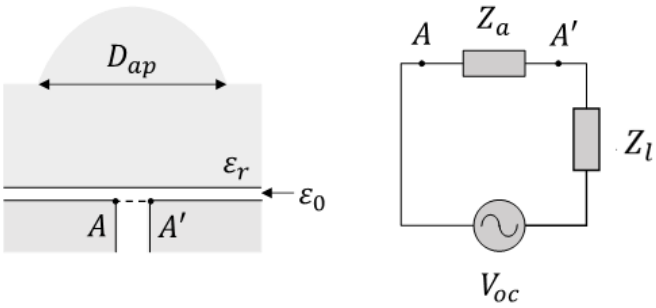

Figure 2.8 Equivalent Thevenin circuit of the Rx aperture

Assuming the Rx antenna is impedance perfectly matched ($Z_a = R_{rad} + jX_a = Z_l^*$), the power received at the load of the antenna is calculated as:

$$P_l = \frac{|V_{oc}|^2}{8R_{rad}} \quad [2.36]$$

Where R_{rad} is the radiation resistance of the Rx antenna. In Tx mode, we can also use the resistance R_{rad} and the exciting current I_0 to determine the radiated power:

$$P_{rad} = \frac{1}{2}|I_0|^2 R_{rad} \quad [2.37]$$

Therefore, the power received at the load of the Rx antenna is calculated as:

$$P_l = \frac{|V_{oc} I_0|^2}{16P_{rad}} \quad [2.38]$$

Where V_{oc} is the open circuit voltage, meaning the voltage induced on the Thevenin circuit terminals, and is the fields radiated by the Tx antenna on the Rx aperture. The term $V_{oc}I_0$ is calculated as a reaction integral between the radiated fields of the Tx antenna on the Rx aperture and the equivalent current on the Rx aperture [22].

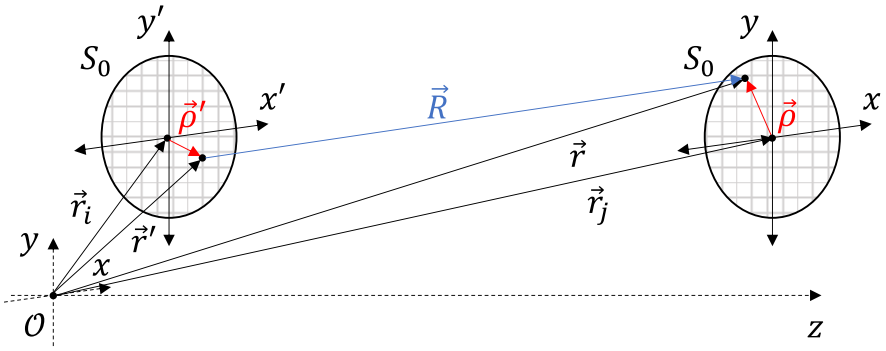

Figure 2.9 Vector definitions used with observation grid in the Fresnel region, at $z = d$, of the domain of the radiating equivalent currents used to calculate the coupling between two apertures.

Assuming two apertures, where the Tx aperture is located at $\vec{r}_i$ and the Rx aperture is located at $\vec{r}_j$, shown in Figure 2.9.

The coupling between two apertures is assumed as Line of Sight (LoS), and the reaction integral on the Rx plane between the field radiated by the Tx antenna with aperture spanned by $\vec{\rho}'$ and the current distribution on the Rx aperture spanned by $\vec{\rho}$ as:

$$V_{oc}^{i} I_0^{j} = \iint_{S_0} \left[\vec{h}_{tx}^{i}(\vec{\rho} - \vec{r}') \cdot \vec{m}_{rx}^{j}(\vec{\rho}) - \vec{e}_{tx}^{i}(\vec{\rho} - \vec{r}') \cdot \vec{j}_{rx}^{j}(\vec{\rho}) \right] d\vec{\rho} \qquad [2.39]$$

Where the Tx and Rx antennas are assumed to be the same, and the reaction integral is integrated with the Rx domain.

We can calculate the coupling according to eq. 2.39 with two approximations:

- Line-of-Sight propagation
- Impedance match (No reflections)

The approximation of LoS requires no multi-path effect such as reflection signals in this model, and the approximation of impedance match requires 100% radiation efficiency of the lens antenna, where both of them are ideal in this model. With these approximations, the reaction integral is calculated as eq. 2.39, and the radiated power calculated as eq. 2.34, the coupling between two apertures is calculated as:

$$h_{ij} = \sqrt{\frac{P_l}{P_{rad}}} = \sqrt{\frac{|V_{oc} I_0|^2}{16 P_{rad}^2}} \qquad [2.40]$$

Eq. 2.40 represent the coupling between lens apertures, and P_{rad} represent the power radiated by the aperture. If the radiation efficiency is less than 100%, to calculate the coupling between lens antennas, the coupling between lens antennas is the product of the radiation efficiency and the coupling between apertures:

$$h_{ij}^{lens} = \sqrt{\frac{|V_{oc} I_0|^2}{16 P_{in}^2}} = \eta_{rad} h_{ij} \qquad [2.41]$$

Eq. 2.41 will be used in Chapter 5 to validate the MALTAB model with CST simulation. See details in Section 5.1.2.

2.3 Channel Matrix & Capacity

In Section 2.2, we derived the coupling between two apertures. Since we are going to study a MIMO system shown in Figure 1.1, in this section, we will introduce the matrix of a set of couplings between one aperture on Tx and one aperture on Rx, the channel matrix.

We will study and simplify the channel matrix in Section 2.3.1; study the coupling and interference levels in Section 2.3.2 and then study the SIR, SNR, and SNIR in Section 2.3.3.

2.3.1 Simplification of Channel Matrix

Since the Rx array is the same as the Tx array, the channel matrix holds a symmetry property, where $h_{ij} = h_{ji}$; the antenna i on the Tx always faces to the antenna i on the Rx directly, $h_{ii} = h_{11}$; if the current distributions on the apertures are also rotationally, from the geometry of our MIMO system in Figure 1.1, we have more equivalent couplings such as $h_{12} = h_{13}$. With this property, the channel matrix can be simplified as:

$$\bar{\bar{H}} = \begin{bmatrix} h_{11} & h_{12} & h_{12} & h_{14} \\ h_{12} & h_{11} & h_{14} & h_{12} \\ h_{12} & h_{14} & h_{11} & h_{12} \\ h_{14} & h_{12} & h_{12} & h_{11} \end{bmatrix} \quad [2.42]$$

This simplified channel matrix is in two conditions:

- The coupling is only based on the LoS propagation
- The current distribution of each aperture is rotationally symmetric

With these simplifications, we only need to calculate the coupling h_{11}, h_{12} and h_{14} in the later part of this thesis. Here, we plot an example of the channel matrix of the MIMO scenario over link distance d at 270GHz with the uniform current, shown in Figure 2.10. Based on the symmetry property, we only need to plot h_{11}, h_{12} and h_{14}.

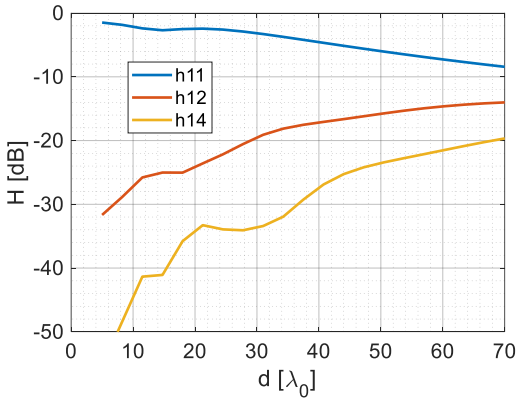

Figure 2.10 The channel matrix entries for uniform current with 6λ aperture at 270 GHz vs the link distance d

From Figure 2.10, the co-coupling h_{11} decrease with distance, and the interference h_{12} and h_{14} increase with distance. In general, the co-coupling level is higher than the interference level because the distance corresponds to the radiative near field (i.e. $d < d_{ff} = 72\lambda_0$).

As introduced in Section 2.2.3, the coupling h_{ij} is frequency-dependent. We choose a typical distance, $d = 30\lambda_0$, and then plot the channel matrix at this distance over different frequencies, shown in Figure 2.11.

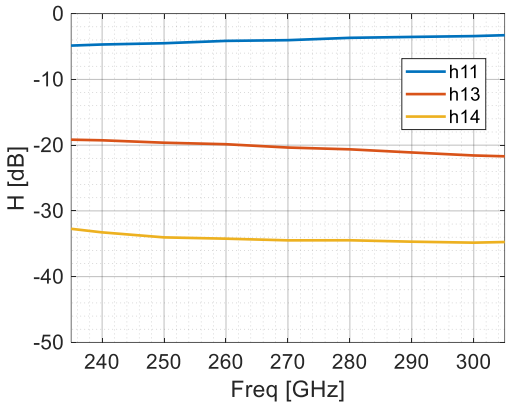

Figure 2.11 The channel matrix of uniform currents with 6λ aperture at $d = 30\lambda_0$ vs frequency

From Figure 2.11, the channel matrix is almost stable in frequency, with only around 2dB changes in 70GHz bandwidth. And the channel matrix at 270GHz matches the result in Figure 2.10. This gives us enough confidence to assume the coupling has a small frequency dependence for optimizing the current distributions at 270GHz for the later study.

2.3.2 Co-coupling and Interference Levels

The co-coupling should be higher than the interferences for operating the system with multiple signals simultaneously. Let us make an example of the Rx antenna Rx 1 in Figure 1.1. For this Rx antenna, the coupling h_{11} is its co-coupling, and the h_{21}, h_{31} and h_{41} are its interferences. The total interference level is calculated as the sum of these interferences, assuming the signals transmitted are random:

$$I(f) = |h_{12}(f)|^2 + |h_{13}(f)|^2 + |h_{14}(f)|^2 \qquad [2.43]$$

The co-coupling and interference levels over different distances at 270GHz are shown in Figure 2.12.

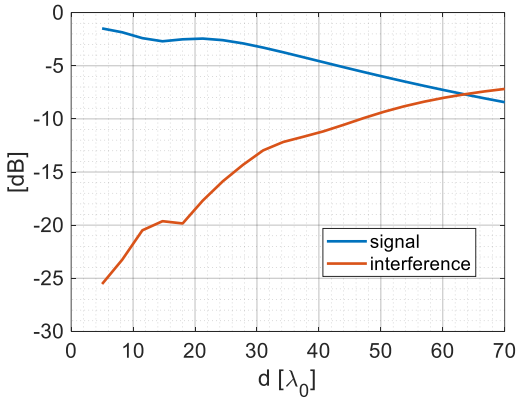

Figure 2.12 The signal and interference levels at 270 GHz

From Figure 2.12, the interference level is higher than the signal level at around $d = 64\lambda_0$. The distance $d = 64\lambda_0$ is close to the far field distance $d_{ff} = 72\lambda_0$, and this validates that we should keep our system in the radiative near field. But it is still not enough to only keep the interference level higher

than the signal level, see Section 2.3.3 to find more detailed studies about the signal, interference, and noise levels.

2.3.3 SIR, SNR and SNIR

There are two unwanted terms: the interference and the noise. We are going to study the impact of these two unwanted terms on the quality of the channel.

The noise is the thermal noise, also known as Johnson-Nyquist noise, which is an inherent and unavoidable component of the communication system. The thermal noise spectrum is calculated as:

$$N(f) = k \cdot T \cdot NF \left[\frac{W}{Hz}\right] \quad [2.44]$$

Where $k = 1.38 \times 10^{-23}\, J \cdot K^{-1}$ is the Boltzmann's constant, T is the temperature in kelvin and NF is the noise figure. In this thesis, the temperature is assumed as $T = 300K$ and the noise figure is set as $NF = 15dB$. These assumptions are based on [13].

Let us to introduce three terms about the quality of the channel: Signal-to-Interference ratio (SIR), Signal-to-Noise ratio (SNR), Signal-to-Noise-and-Interference ratio (SNIR) calculated as:

$$SIR(f) = \frac{P_S(f)}{P_I(f)} \quad [2.45]$$

$$SNR(f) = \frac{P_S(f)}{N(f)} \quad [2.46]$$

$$SNIR(f) = \frac{P_S(f)}{N(f) + P_I(f)} \quad [2.47]$$

Where P_S is the power spectral density of the received signals and P_I is the power spectral density of the received interferences. These two terms depend on the channel matrix and the input power spectral density. For example, the power spectral density of the signal and the power spectral density of interference for Rx antenna 1 is calculated as follows:

$$P_S(f) = P_t(f)|h_{11}(f)|^2 \left[\frac{W}{Hz}\right] \quad [2.48]$$

$$P_I(f) = \sum_{i \neq 1} P_t(f)|h_{i1}(f)|^2 \left[\frac{W}{Hz}\right] \quad [2.49]$$

Where $P_t(f)$ is the transmitted spectral power density, $h_{11}(f)$ is the co-coupling of Rx antenna 1 and $h_{i1}(f)$s are the interferences of Rx antenna 1. Assuming the channel matrix is independent of frequency, and taking the value at the center frequency $h_{ij}(270GHz)$ into eq. 2.45-2.49, we can have the SIR, SNR, and SNIR at 270GHz, shown in Figure 2.13.

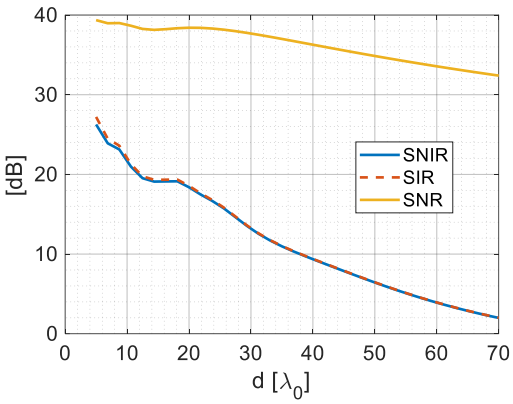

Figure 2.13 The SIR, SNR and SNIR at 270 GHz

From the definition of SIR, SNR, and SNIR, their level should be as high as possible for the high quality of the channel. From Figure 2.13, the SNR is much higher than the SIR and SNIR, and the level of SIR is almost equal to SNIR. This means that the interference level has a dominating effect on the quality of the channel. Combining the fact that the noise is unavoidable, it is important to decrease the interference level to increase the quality of the channel. From Figure 2.13, at the distance $d = \frac{d_{ff}}{2} = 36\lambda_0$, the SNIR is around 12dB, which is almost the lowest possible SNIR for a channel. As a result, we define this distance as the incoherent distance and define the incoherent range as $d \in [0, \frac{d_{ff}}{2}]$. In the later part of this thesis, the interested range will be located in this incoherent range. More specifically, the interested range in this thesis $d \in [10\lambda_0, 30\lambda_0]$. To better illustrate the result and its change over distance, the results from the channel matrix model will be presented within the link distance range of $d \in [5\lambda_0, 40\lambda_0]$.

2.3.4 Capacity for Near Field Links

In Section 2.3.3, we calculated the channel matrix and then use the channel matrix to calculate the SIR, SNR and SNIR to evaluate the quality of the channel. In this section, we use the channel capacity for quantifying the quality of the channel.

The Shannon channel capacity [17] (called as capacity in the later part of the thesis) is a fundamental concept developed by Claude E. Shannon in information theory. It determines the theoretical maximum data rate that can be transmitted with error-free through a channel. From Shannon capacity, [18] derived the capacity for MIMO antenna arrays taking in account the bandwidth, SNIR, calculated as follows:

$$C = \sum_{i=1}^{4} \int_{235GHz}^{305GHz} \log_2\left(1 + \frac{P_t(f)|h_{ii}(f)|^2}{N(f) + \sum_{j\neq i} P_t(f)\left|h_{ij}(f)\right|^2}\right) df \left[\frac{bit}{s}\right] \qquad [2.50]$$

Where $h_{ii}(f)$s are the co-coupling levels and $h_{ij}(f)$s are the interference levels in the channel matrix. The transmitted power $\int_{235GHz}^{305GHz} P_t(f)df$ is set as -10 dBm based on [13].

We can assume the channel matrix is independent with frequency, applying $h_{ij}(270GHz)$ for entire frequency band to calculate the capacity, called as the capacity at 270GHz. We also calculate the capacity with the channel matrix over frequency $h_{ij}(f)$ to calculate the capacity. These two results are shown in Figure 2.14.

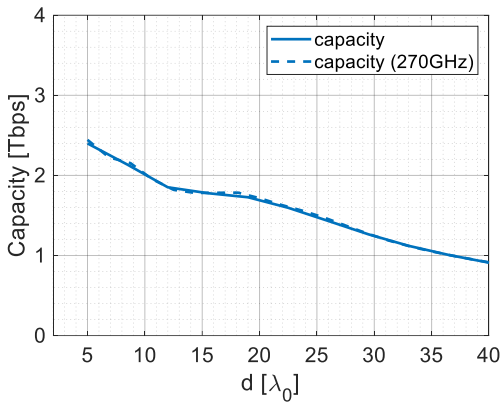

Figure 2.14 Capacities of uniform current with spectral channel matrix (solid line) and with channel matrix at 270GHz (dash line)

From Figure 2.14, the capacities considering with and without the frequency dependence of the channel matrices are well matched, meaning that the influence of the frequency dependence of the channel matrix onto the capacity is negligible. And the capacity is more than 1Tbps over our interested range, which has high data rate potential.

3 Optimized Current Distribution

In Chapter 2 we introduced the methodology to estimate the capacity in radiative near field link composed by a Tx and a Rx 2×2 lens arrays. Results of the achievable capacity were provided assuming a uniform current distribution. In Chapter 2, we saw that for our application, the array in which the elements radiate a uniform field is interference-limited. In this chapter, we will derive an optimized current distribution that maximizes the signal coupling and minimizes the interference levels in this multi-channel link.

We will revise the theoretical expression of the ideal current distribution in Single Input Single Output (SISO) in the near field link in Section 3.1 derived in [16]. Then we show its current distribution and coupling results in Section 3.2, and then we find that the possible match between this ideal current and Gaussian based current distribution, shown in Section 3.3. After studying the SISO, we apply this ideal current distribution for a MIMO scenario, shown in Section 3.4, and then find the optimized current distribution for our application scenario, shown in Section 3.5.

3.1 Ideal Current Distribution in a LoS Link in the Fresnel Zone

We revise the work from G. Borgiotti [16] here. He focused on the problem of maximizing the wireless power transfer between two apertures in a LoS link located in the Fresnel zone. He derived the ideal current distribution in a square aperture for maximum power transfer. In this section, we introduce this current distribution, which optimizes the coupling between two apertures in the radiative near field, called ideal current distribution. Figure 3.1 shows a schematic diagram of the SISO link between two square apertures in a LoS.

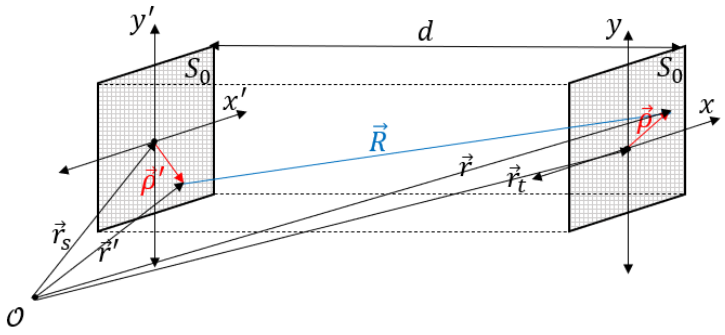

Figure 3.1 The schematic diagram of the coupling between two apertures

From Figure 3.1, two square apertures are faced to each other with link distance d. Starting from eq. 2.19 and 2.20, several assumptions [16] on the current distributions and the radiated field can be made to have the fields radiated by the source on an observation point $\vec{r}$ in the Fresnel zone of the aperture [16]:

$$\vec{e}^{i}_{tx}(\vec{r}) \approx -jk_0\zeta_0(\tilde{I}-\hat{z}\hat{z})\frac{1}{2\pi d}e^{-jk_0 d}e^{-\frac{jk_0|\vec{\rho}|^2}{2d}}\iint_{S_0}\vec{J}^{i}_{tx}(\vec{\rho}')e^{-\frac{jk_0|\vec{\rho}'|^2}{2d}}e^{\frac{jk_0}{d}\vec{\rho}\cdot\vec{\rho}'}d\vec{\rho}'$$

$$+jk_0(\hat{z}\times\tilde{I})\frac{1}{2\pi d}e^{-jk_0 F}e^{-\frac{jk_0|\vec{\rho}|^2}{2d}}\iint_{S_0}\vec{m}^{i}_{tx}(\vec{\rho}')\,e^{-\frac{jk_0|\vec{\rho}'|^2}{2d}}e^{\frac{jk_0}{d}\vec{\rho}\cdot\vec{\rho}'}d\vec{\rho}' \qquad [3.1]$$

$$\vec{h}_{tx}^{i}(\vec{r}) \approx -\frac{jk_0}{\zeta_0}(\tilde{I}-\hat{z}\hat{z})\frac{1}{2\pi d}e^{-jk_0 d}e^{-\frac{jk_0|\vec{\rho}|^2}{2d}}\iint_{S_0}\vec{m}_{tx}^{i}(\vec{\rho}')e^{-\frac{jk_0|\vec{\rho}'|^2}{2d}}e^{\frac{jk_0}{d}\vec{\rho}\cdot\vec{\rho}'}d\vec{\rho}'$$

$$-jk_0(\hat{z}\times\tilde{I})\frac{1}{2\pi d}e^{-jk_0 d}e^{-\frac{jk_0|\vec{\rho}|^2}{2d}}\iint_{S_0}\vec{j}_{tx}^{i}(\vec{\rho}')\,e^{-\frac{jk_0|\vec{\rho}'|^2}{2d}}e^{\frac{jk_0}{d}\vec{\rho}\cdot\vec{\rho}'}d\vec{\rho}' \qquad [3.2]$$

Where $\vec{r}$ is the observation point, k_0 is the propagation constant in free space, $\vec{\rho}$ is the radial component which spans the entire area of the circular aperture, and d is the link distance between the Tx and Rx apertures.

These simplified expressions can be used as long as:

$$2.5D_{ap} < d \qquad [3.3]$$

$$\frac{D_{ap}^4}{2\lambda} < d^3 \qquad [3.4]$$

Eq. 3.3 and 3.4 indicate the Fresnel zone. With eq. 3.1 and 3.2, we can rewrite the reaction integral as:

$$(V_{oc}I_0)^{ij} = C\int_{S_{rx}} j_{rx}^{j}(\vec{\rho})e^{-\frac{jk_0|\vec{\rho}|^2}{2d}}\iint_{S_{tx}} j_{tx}^{i}(\vec{\rho}')e^{-\frac{jk_0|\vec{\rho}'|^2}{2d}}e^{j\frac{k_0}{d}\vec{\rho}\cdot\vec{\rho}'}d\vec{\rho}'d\vec{\rho} \qquad [3.5]$$

Where $C = \frac{jk_0\zeta_0}{\pi d}e^{-jk_0 d}$.

We find that both integrals have an expression for the current distribution as well as a phase focusing term. Therefore, to simplify the expression even further we define the current expressions in the following manner:

$$f_{tx}(\vec{\rho}') = j_{tx}^{i}(\vec{\rho}')e^{-\frac{jk_0|\vec{\rho}'|^2}{2d}} \qquad [3.6]$$

$$f_{rx}(\vec{\rho}) = j_{rx}^{j}(\vec{\rho})e^{-\frac{jk_0|\vec{\rho}|^2}{2d}} \qquad [3.7]$$

It is important to note that this $f_{tx}(\vec{\rho}')$ is a new defined function, not the distribution function in Chapter 2.

Therefore, the coupling integral eq. 3.5 can be written as:

$$(V_{oc}I_0)^{ij} = C\int_{S_{rx}} f_{rx}(\vec{\rho})\iint_{S_{tx}} f_{tx}(\vec{\rho}')e^{j\frac{k}{d}\vec{\rho}\cdot\vec{\rho}'}d\vec{\rho}'d\vec{\rho} \qquad [3.8]$$

We can recognize it as a double integral in the form of a Fourier Transform (FT) of eq. 3.6 and 3.7 which is defined as:

$$F_{tx}(\vec{k}_\rho) = \iint_{S_0} f_{tx}(\vec{\rho}')e^{j\frac{k_0}{d}\vec{\rho}\cdot\vec{\rho}'}d\vec{\rho}' \qquad [3.9]$$

$$F_{rx}(\vec{k}'_\rho) = \iint_{S_0} f_{rx}(\vec{\rho})e^{j\frac{k_0}{d}\vec{\rho}\cdot\vec{\rho}'}d\vec{\rho} \qquad [3.10]$$

Where $\vec{k}_\rho = \frac{k_0}{d}\vec{\rho}$ and $\vec{k}'_\rho = \frac{k_0}{d}\vec{\rho}'$. With the FT term $F_{tx}(\vec{\rho})$ and $F_{rx}(\vec{k}'_\rho)$, the expression for the coupling of two apertures in the Fresnel region is simplified to:

$$V_{oc}^{i} I_{0}^{j} \approx C \iint_{S_0} f_{rx}(\vec{\rho}) F_{tx}(\vec{k}_{\rho}) d\vec{\rho} \quad [3.11]$$

We need to maximize the integral in eq. 3.11 to maximize the coupling between two apertures in the Fresnel region. We can then define the idea Tx current and Rx current such as to maximize the following integrals:

1) Transmitter current:

$$\left| \iint_{S_0} f_{tx}(\vec{\rho}') F_{rx}(\vec{k}_{\rho}') d\vec{\rho}' \right|^2 \quad [3.12]$$

2) Receiver current:

$$\left| \iint_{S_0} f_{rx}(\vec{\rho}) F_{tx}(\vec{k}_{\rho}) d\vec{\rho} \right|^2 \quad [3.13]$$

It is widely known that the FT of the current with complex conjugate to the current function can maximize these functions. To find the expression of these functions, we are going to use the domain functions and re-write these functions into a form of FT:

$$\mathrm{Domain}_{\mathrm{tx}}(\vec{k}_{\rho}) = FT\{\mathrm{domain}_{\mathrm{tx}}(\vec{\rho}')\} = \iint_{S_0} e^{j\frac{k_0}{d}\vec{\rho}\cdot\vec{\rho}'} d\vec{\rho}' \quad [3.14]$$

$$\mathrm{Domain}_{\mathrm{rx}}(\vec{k}_{\rho}') = FT\{\mathrm{domain}_{\mathrm{rx}}(\vec{\rho})\} = \iint_{S_0} e^{j\frac{k_0}{d}\vec{\rho}\cdot\vec{\rho}'} d\vec{\rho} \quad [3.15]$$

Where $domain_{tx}(\vec{\rho}')$ describe the aperture domain for Tx, $domain_{rx}(\vec{\rho})$ describe the aperture domain for Rx, and $Domain_{tx}(\vec{k}_{\rho})$ and $Domain_{rx}(\vec{k}_{\rho}')$ are their FTs.

With eq. 3.9, 3.10, 3.14 and 3.15, the equation that we want to find its optimal form to maximize the coupling become:

1) Transmitter current:

$$f_{tx}(\vec{\rho}') = \mathrm{domain}_{\mathrm{tx}}(\vec{\rho}') F_{rx}^{*}(\vec{k}_{\rho}') \quad [3.16]$$

where,

$$F_{rx}^{*}(\vec{k}_{\rho}') = \iint_{S_0} f_{rx}^{*}(\vec{\rho}) e^{-j\frac{k_0}{d}\vec{\rho}\cdot\vec{\rho}'} d\vec{\rho} \quad [3.17]$$

2) Receiver current:

$$f_{rx}(\vec{\rho}) = \mathrm{domain}_{\mathrm{rx}}(\vec{\rho}) F_{tx}^{*}(\vec{k}_{\rho}) \quad [3.18]$$

where,

$$F_{tx}^{*}(\vec{k}_{\rho}) = \iint_{S_0} f_{tx}^{*}(\vec{\rho}') e^{-j\frac{k_0}{d}\vec{\rho}\cdot\vec{\rho}'} d\vec{\rho}' \quad [3.19]$$

Let us start from substituting eq. 3.18 into eq. 3.17:

$$F_{rx}^{*}(\vec{k}_{\rho}') = \iint_{-\infty}^{\infty} \text{domain}_{\text{rx}}(\vec{\rho}) F_{tx}(\vec{k}_{\rho}) e^{-j\frac{k_0}{d}\vec{\rho}\cdot\vec{\rho}'} d\vec{\rho} \quad [3.20]$$

Therefore, the expression for $f_{tx}(\vec{\rho}')$ becomes:

$$f_{tx}(\vec{\rho}') = \text{domain}_{\text{tx}}(\vec{\rho}') \iint_{-\infty}^{\infty} \text{domain}_{\text{rx}}(\vec{\rho}) F_{tx}(\vec{k}_{\rho}) e^{-j\frac{k_0}{d}\vec{\rho}\cdot\vec{\rho}'} d\vec{\rho} \quad [3.21]$$

The term inside the double integral can be regarded as the FT of the multiplication of two functions in the spectral domain. We can re-write this equation as a form of convolution, shown as follows:

$$f_{tx}(\vec{\rho}') = \text{domain}_{\text{tx}}(\vec{\rho}') \int_{-\infty}^{\infty} \text{Domain}_{\text{rx}}(\vec{\rho}' - \vec{\tau}) f_{tx}(\vec{\tau}) d\vec{\tau} \quad [3.22]$$

It is equivalent to the function on Rx:

$$f_{rx}(\vec{\rho}) = \text{domain}_{\text{rx}}(\vec{\rho}) \int_{-\infty}^{\infty} \text{Domain}_{\text{tx}}(\vec{\rho} - \vec{\tau}) f_{rx}(\vec{\tau}) d\vec{\tau} \quad [3.23]$$

Boyd and Kogelnik solved this equation for a system of confocal resonators [19]. This paper shows that there are a set of modes with orthogonal distributions, corresponding to the current distribution on different apertures. The solution of eq. 3.22 and 3.23 should have the form of:

$$\frac{2c}{pi}[R_{0n}^{1}(c,1)]^2 S_{0n}(c,t) = (-1)^n \int_{-1}^{1} \frac{\sin[c(t+s)]}{\pi(t+s)} S_{0n}(c,s) ds \quad [3.24]$$

Where $R_{0n}^{1}(c,1)$ is the radial prolate spheroidal wave functions of order n and $S_{0n}(c,t)$ is the prolate spheroidal wave function of order n, and c is a constant.

If we consider the FT of a square aperture:

$$\text{Domain}(\vec{\rho}) = \frac{2\sin\left[\frac{k_0 x}{d}\frac{D_{ap}}{2}\right]}{\frac{k_0 x}{d}} \frac{2\sin\left[\frac{k_0 y}{d}\frac{D_{ap}}{2}\right]}{\frac{k_0 y}{d}} \quad [3.25]$$

Equation 3.22 and 3.23 becomes:

$$f_{tx}(\vec{\rho}') = \text{domain}(\vec{\rho}') S_{00}(c,x') S_{00}(c,y') \quad [3.26]$$

$$f_{rx}(\vec{\rho}) = \text{domain}(\vec{\rho}) S_{00}(c,x) S_{00}(c,y) \quad [3.27]$$

With $c = \frac{k_0}{d}\frac{D_{ap}^2}{4}$. Substituting 3.26 and 3.27 to 3.6 and 3.7, we have the final expression of the ideal current distribution of square apertures at Tx and Rx:

$$\vec{J}_{tx}(\vec{\rho}') = \text{domain}(\vec{\rho}') S_{00}(c,|\vec{\rho}'|) e^{-\frac{jk_0|\vec{\rho}'|^2}{2d}} \quad [3.28]$$

$$\vec{J}_{rx}(\vec{\rho}) = \text{domain}(\vec{\rho}) S_{00}(c,|\vec{\rho}|) e^{-\frac{jk_0|\vec{\rho}|^2}{2d}} \quad [3.29]$$

Where domain($\vec{\rho}'$) refers to the aperture domain, should be square aperture from [16]. $S_{00}(c, |\vec{\rho}'|)$ is the spheroidal wave equation of order zero, k_0 is the propagation constant in free space, d is the distance between two apertures, and $c = \frac{k_0}{d}\frac{D_{ap}^2}{4}$.

S. Takeshita [20] found that eq. 3.28 and 3.29 also work well in circular aperture. Considering that most common lens antennas are with circular aperture, in this thesis we will define domain($\vec{\rho}$) as the circular aperture with diameter $D_{ap} = 6\lambda$.

In eq. 3.28 and 3.29, $S_{00}(c, |\vec{\rho}'|)$ is the amplitude distribution and $e^{-\frac{jk_0|\vec{\rho}'|^2}{2d}}$ is the phase distribution. The physical meaning of this phase distribution is to focus on the Rx antenna plane. The amplitude and the phase distribution depend on the distance between two apertures d. This result matches with the result from G.Borgiotti [16], saying that the signal must focus on the Rx aperture to obtain a conjugate match between the field radiated by the Tx and the current on the Rx.

However, he only focused on the maximum power transfer in a SISO link, but he did not study the signal and interference level in the MIMO scenario. This leaves us space for the study, shown in 3.5.

3.2 Distribution and Coupling of Ideal Current Distribution

In this section, we will first show the ideal current distribution derived in the previous section, and then calculate the channel matrix between this current distribution according to eq. 3.28 and 3.29 in MATLAB using the ideal current. The simulated coupling results will be then compared with the coupling of the uniform current. We consider here circular apertures. The spheroidal wave of order zero is rotationally symmetric. It can therefore be shown that the coupling between two circular apertures in the LoS located in the Fresnel regions is optimized for the following current distribution:

$$f(\vec{\rho}) = \mathrm{circ}(|\vec{\rho}|, \frac{\mathrm{D}}{2}) S_{00}(c, |\vec{\rho}|) e^{-\frac{jk_0|\vec{\rho}|^2}{2d}} \qquad [3.30]$$

Where $c = \frac{k_0}{d}\frac{D_{ap}^2}{4}$. Eq. 3.30 is called the ideal current distribution in this thesis. The ideal current distribution changes with the link distance between two apertures. Since the scenario of this thesis is with distance $d \in [10\lambda_0, 30\lambda_0]$, we choose to study the current distribution with distance $d = 10\lambda_0$ and $d = 30\lambda_0$. Both amplitude and phase distribution will be shown. The normalized amplitude distributions at two typical distances, $d = 10\lambda_0$ and $d = 30\lambda_0$ at 270 GHz are shown in Figure 3.2.

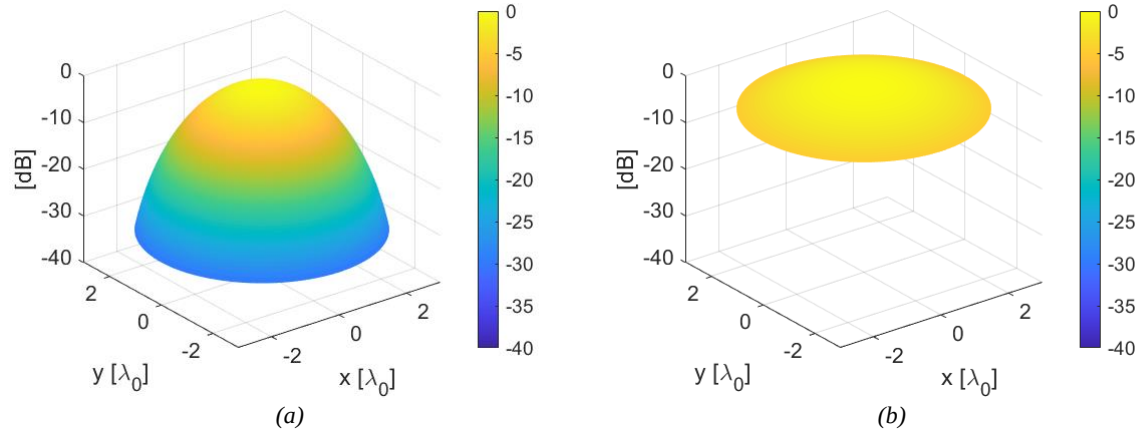

Figure 3.2 The amplitude of the ideal current distribution fixed at (a) $d = 10\lambda_0$ and (b) $d = 30\lambda_0$

From Figure 3.1, the amplitude distribution is a rotationally symmetric distribution, in which the amplitude of the current at the center of the aperture is maximum and then decreases with ρ, and $\vec{\rho}$ is the radial component which spans the entire area of the circular aperture. This distribution is a tapered distribution. Comparing the amplitude distributions at two distances, the taper level is higher when two apertures are closer and the level decreases with link distance. We define a taper level, which is the ratio between the amplitude at the edge and the amplitude at the center of the aperture, and we plot the taper level over distances in Figure 3.3.

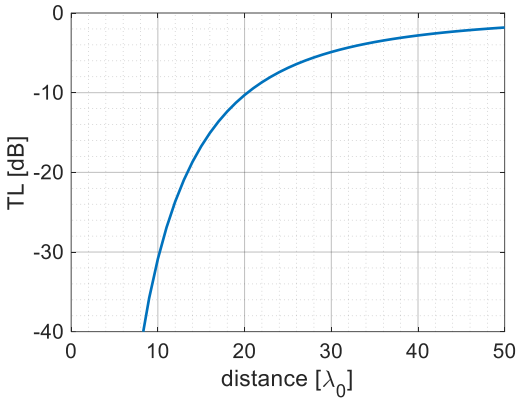

Figure 3.3 The taper level of ideal current distribution

From Figure 3.3, the ideal current distribution is less amplitude taper when two apertures are far away from each other, and the taper level is around -2dB taper at $d = 50\lambda_0$.

In Figure 3.4, the phase profile of the ideal current distribution is plotted. The phase distribution is a rotationally symmetric distribution, and the phase changes more when the distance between apertures is closer. As the Tx and Rx apertures are focused on each other, the phase term will focus at infinite and the phase distribution will be equivalent to the uniform distribution (unfocused) when two apertures are far away.

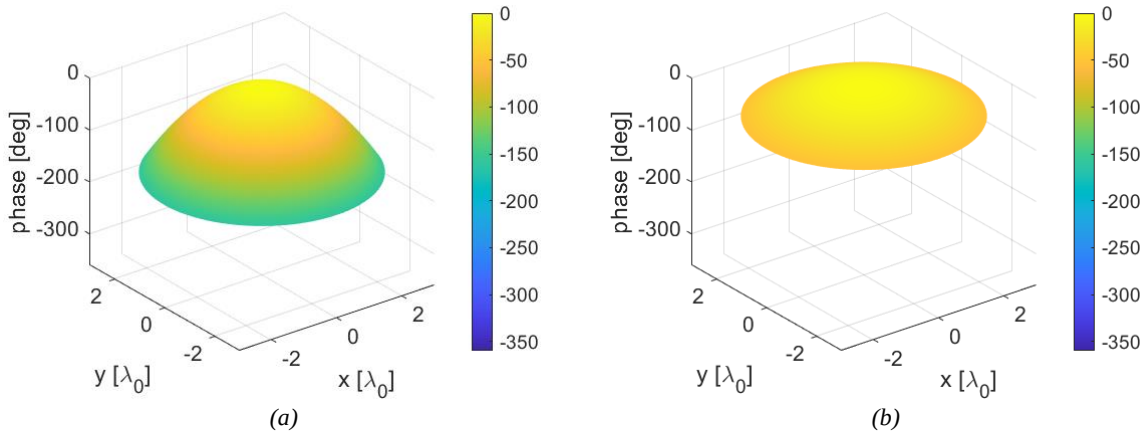

Figure 3.4 The phase distribution of the ideal current fixed at (a) $d = 10\lambda_0$ and (b) $d = 30\lambda_0$

Let us define a phase difference level, which is the difference between the phase at the edge and the phase at the center of the aperture, and we plot the phase difference level over distances in Figure 3.3.

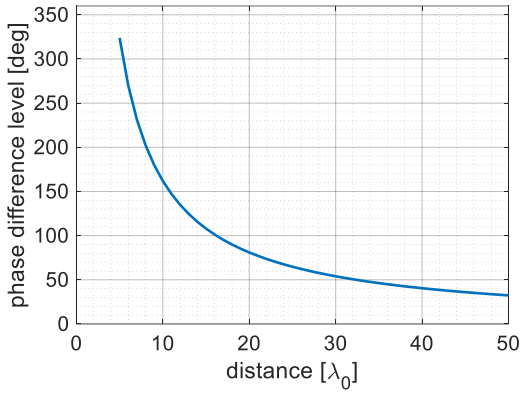

Figure 3.5 The phase difference level of ideal current distribution

From Figure 3.5, the phase difference of the ideal current distribution is less when two apertures are far away from each other. Combing Figure 3.3 and Figure 3.5, when two apertures are far away from each other, we can approximate this current distribution as a uniform distribution.

As mentioned in Chapter 2, the electric currents and the magnetic currents are defined as eq. 2.11 and 2.12. Substituting eq. 3.30 into eq. 2.11 and 2.12, we have the electric current and magnetic current with ideal current distribution, called as ideal current.

Next, we want to study the coupling of the ideal currents at 270GHz. The coupling at 270GHz is calculated according to eq. 2.41. The coupling of uniform current are also shown in Figure 3.6 as a reference.

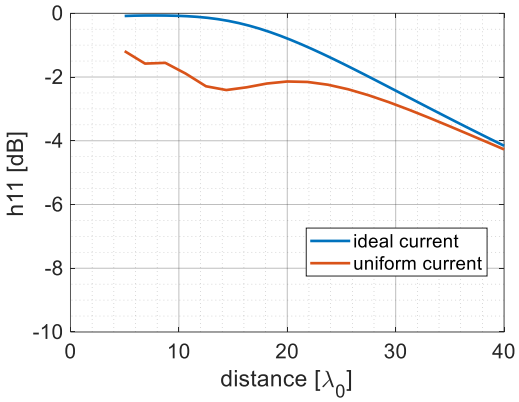

Figure 3.6 The coupling of ideal current and uniform current at 270GHz in SISO

From Figure 3.6, the coupling of the ideal current is around 100% in close near field and then decreases over distance. Compared with the uniform current, the ideal one has significant advantages in the close-near field ($d < 20\lambda_0 \approx 0.28d_{ff}$). The performances of these two currents are similar at $d > 40\lambda_0 \approx 0.56d_{ff}$, when reaching more than half of the far field distance. Meanwhile, this shows that the uniform current is equivalent to the ideal current when the distance is far enough.

We will then plot the field radiated by the ideal current. Same as what we did in the previous part of this section, we choose $d = 10\lambda_0$ and $d = 30\lambda_0$ to fix the current distribution and then plot the field radiated by these two ideal currents with fixed distributions. The electric fields radiated by the ideal currents fixed at $d = 10\lambda_0$ and $d = 30\lambda_0$ at 270GHz are calculated from eq. 2.27, shown in Figure 3.7.

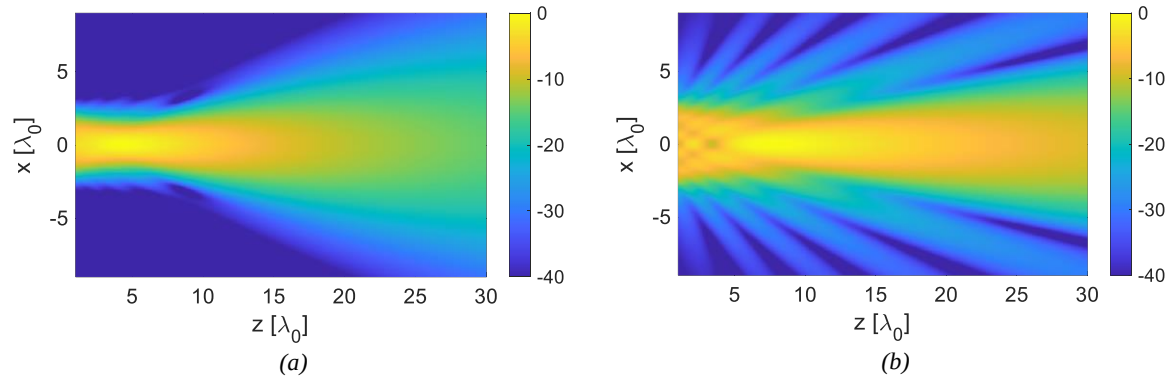

Figure 3.7 The electric field radiated by the ideal currents fixed at (a) $d = 10\lambda_0$, (b) $d = 30\lambda_0$

From Figure 3.7, the field radiated by the current distribution at $d = 10\lambda_0$ has wider main beam, and almost has no side lobes; the field radiated by the current distribution at $d = 30\lambda_0$ has narrower main beam, but also has more side lobes.

3.3 Fitting of Ideal Current Distribution with Gaussian Distribution

The angular prolate spheroidal wave function is uncommon in antenna design. It does not have an analytical expression and requires a numerical evaluation of the function to generate and to simulate. As a result, we would like to find an analytically known function to fit to the spheroidal wave function in the expression of the ideal current distribution. For this, we will use the Gaussian function as this function to fit the angular prolate spheroidal function in literature. S. Takeshita [20] and G. D. Boyd and H. Kogelnik [19] studied Gaussian distributions to replace the angular prolate spheroidal wave function with reasonable accuracy for circular apertures.

The Gaussian beam over a circular aperture is defined as:

$$g(\vec{\rho}') = e^{-\frac{|\vec{\rho}'|^2}{w_0^2}} \qquad [3.31]$$

Where $\vec{\rho}'$ is the radial component which spans the entire area of the circular aperture and w_0 is the waist of the Gaussian beam. w_0 can be defined as the taper level of this Gaussian beam and the diameter of the aperture, and is calculated as:

$$w_0 = \sqrt{\frac{8.686}{TL}}\frac{D_{ap}}{2} \qquad [3.32]$$

Where TL is the taper level, defined as the ratio between the amplitude at the edge and the amplitude at the center of the aperture.

Replacing spheroidal wave equation in eq. 3.28 and 3.29 by the Gaussian beam in eq. 3.31, the ideal current distribution becomes:

$$f(\vec{\rho}) = circ\left(\vec{\rho}, \frac{D}{2}\right) e^{-\frac{|\vec{\rho}'|^2}{w_0^2}} e^{-\frac{jk_0|\vec{\rho}'|^2}{2d}} \qquad [3.33]$$

We need to find the appropriate expression for w_0 to match the eq. 3.28 and 3.29. After multiple simulations, the w_0 is chosen to:

$$w_0 = \sqrt{2}\lambda_0(0.08\frac{d}{\lambda_0} + 0.5) \quad [3.34]$$

Where d is the distance between two apertures, and λ_0 is the free space wavelength at the center frequency.

The agreements of these two current amplitude distributions (calculated as eq. 3.30 and eq. 3.33 respectively) with $d = 10\lambda_0$ and $d = 30\lambda_0$ are shown in Figure 3.8.

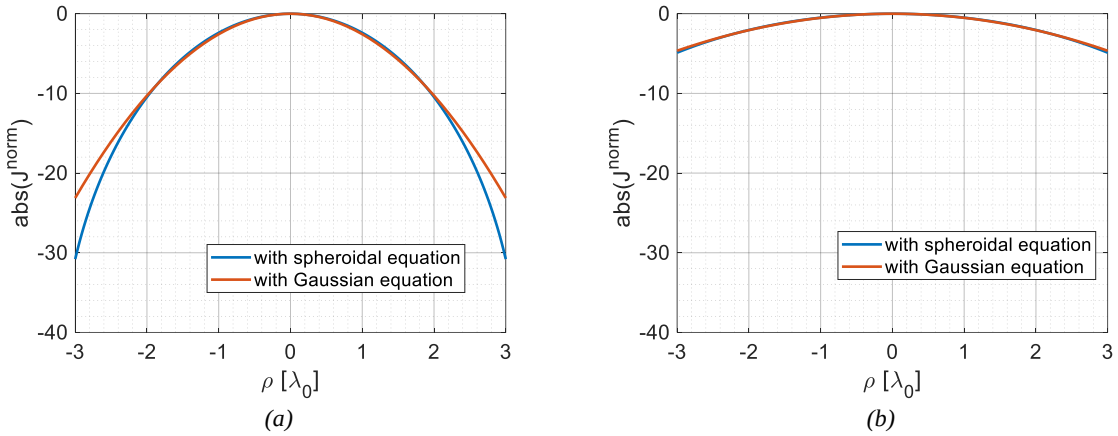

Figure 3.8 The amplitudes of ideal current distribution fixed (a) with $d = 10\lambda_0$ and (b) with $d = 30\lambda_0$ applying eq. 3.30 (blue solid line) and in eq. 3.33 (red solid line)

From Figure 3.8, the amplitudes of the ideal current distributions applying spheroidal equation as eq. 3.30 and the of the one applying Gaussian beam as eq. 3.33 are in a good agreement.

We can also calculate the taper levels of the ideal current distribution applying spheroidal equation as eq. 3.30 and the one applying Gaussian beam as eq. 3.33 over link distance, shown in Figure 3.9. As mentioned before, the taper level is defined as the ratio of the amplitude at the edge to the amplitude at the center.

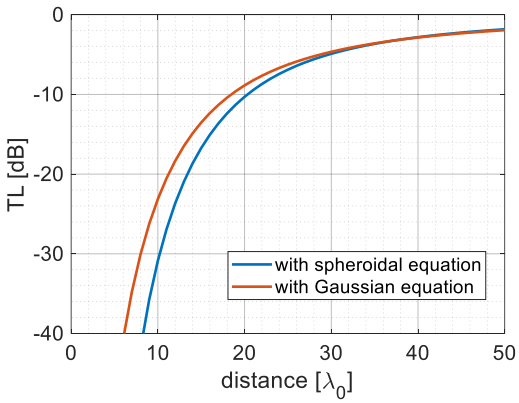

Figure 3.9 The taper level of the ideal current distribution applying Gaussian beam as eq. 3.33 (blue solid line) and applying spheroidal equation as eq. 3.30 (red solid line)

From Figure 3.9, we find some mismatch in the taper level at the shorter distance. This is because these two distributions are different. To have the match of the distribution in the middle of the aperture, we sacrifice the match of the distribution in the edge, however the coupling is not affected as it will be shown next.

Next, we would like to compare the coupling between apertures with the distribution from eq. 3.30 and 3.33, shown in Figure 3.10.

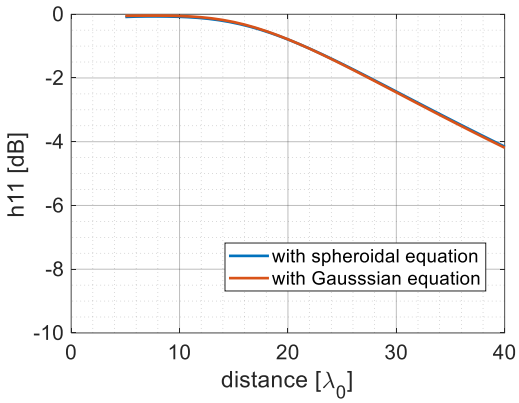

Figure 3.10 The h_{11} with ideal current distribution in (a) eq. 3.28 and in (b) eq. 3.33

In Figure 3.10, we see an excellent agreement between the coupling of the ideal current distribution with the spheroidal equation and the coupling of the ideal current distribution with the Gaussian beam. Based on this agreement, we can use eq. 3.33 to represent the ideal current distribution in the radiative near field. This will be more efficient in coupling simulation in MATLAB, and will also help us to design the antenna (see Chapter 4). Since the coupling results are almost unchanged, in the rest part of the thesis, we will still call this current distribution as the ideal current distribution, but calculated with the Gaussian beam, as eq. 3.33. Equivalently, the currents with this ideal current distribution by Gaussian will still be named as the ideal current in the rest of this thesis.

3.4 Using the Ideal Current Distribution in a MIMO Scenario

In this section we evaluate the channel matrix according to eq. 2.41 using the previously described ideal current via the Gaussian fit function. The uniform current will be used as a reference to study the improvement in coupling. Since we already validated the spectral stability of the channel matrix in Section 2.3, we will only calculate the channel matrix at 270GHz. As introduced in Chapter 2, based on the symmetry of the channel matrix, it is sufficient to only show h_{11}, h_{12} and h_{14}, where h_{11} represents the coupling and h_{12} and h_{14} represents the interferences.

We will first look at the coupling and interference levels in Figure 3.11. From the definition of the channel model, introduced in Chapter 2, the h_{11} is the coupling, the h_{12} and h_{14} are the interferences. From Figure 3.11, by comparing the channel matrix of the ideal current to that of the uniform current, we can see that for the ideal current, the coupling h_{11} is increased and interferences h_{12} and h_{14} are decreased.

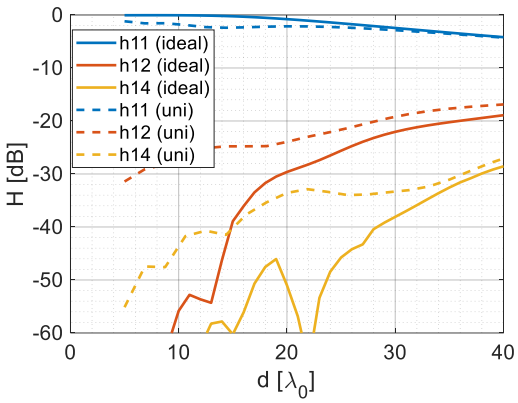

Figure 3.11 The channel matrix of the ideal current (solid lines) and the one of uniform current (dash lines)

From eq. 2.50, with fixed bandwidth BW, number of elements M, power input to the array P_{tx} and noise level N, the capacity only depends on the channel matrix. In particular, higher coupling h_{11} and lower interferences h_{12} and h_{14} will increase the capacity. From Figure 3.11, the coupling of ideal current has high coupling h_{11} and lower interference h_{12} and h_{14}, which should provide us a higher capacity. Figure 3.12 shows the capacity of the ideal current and the one of the uniform current.

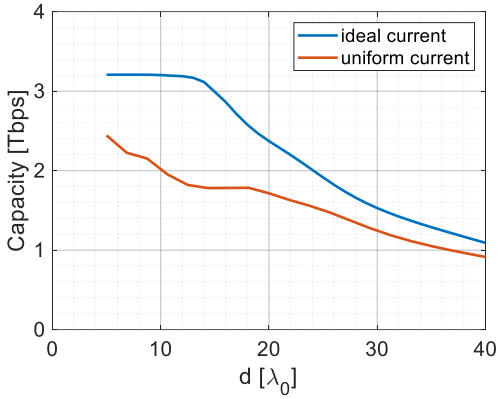

Figure 3.12 The capacity of the ideal current distribution and the one of uniform current distribution

From Figure 3.12, the ideal current will provide us with better capacity than the results from uniform current. The advantage of using the ideal current distribution is more significant when the distance is less than $d = 20\lambda_0 = 0.28d_{ff}$, and the capacity is more or less doubled when using the ideal current.

3.5 Parametric Study for Optimization of Ideal Current Distribution

The results of the previous section show that the ideal current has a significant increase in capacity, compared to that of the uniform current. However, this ideal current changes over distance, which cannot be implemented in scenarios when the distance is not fixed. Moreover, the ideal current is only ideal for a SISO link, not when there are several antennas creating interference such as in the 2×2 MIMO case. In this section, we are going to find an optimized current distribution for the entire range of considered distances, that will maximize the coupling and capacity.

To find the optimal parameters for this distribution (i.e. taper level and focusing distance), we will first randomly choose a parameter to fix the ideal current distribution and check the coupling and capacity,

shown in Section 3.5.1, and we will then do the parametric study to find the optimal parameters to fix the ideal current distribution, shown in Section 3.5.2.

3.5.1 Fixed Ideal Current Distribution

As introduced in Chapter 3, both of the amplitude and phase distributions of the ideal current change with distance. We are interested in the behavior of the array in the incoherent range $d \in [10\lambda_0, 30\lambda_0]$, defined in Chapter 2, and therefore want to study in the limits of this range. We start by fixing the ideal current to a very small link distance, $d = 10\lambda_0 = 0.14d_{ff}$. The current amplitude and phase distributions are shown in Figure 3.13.

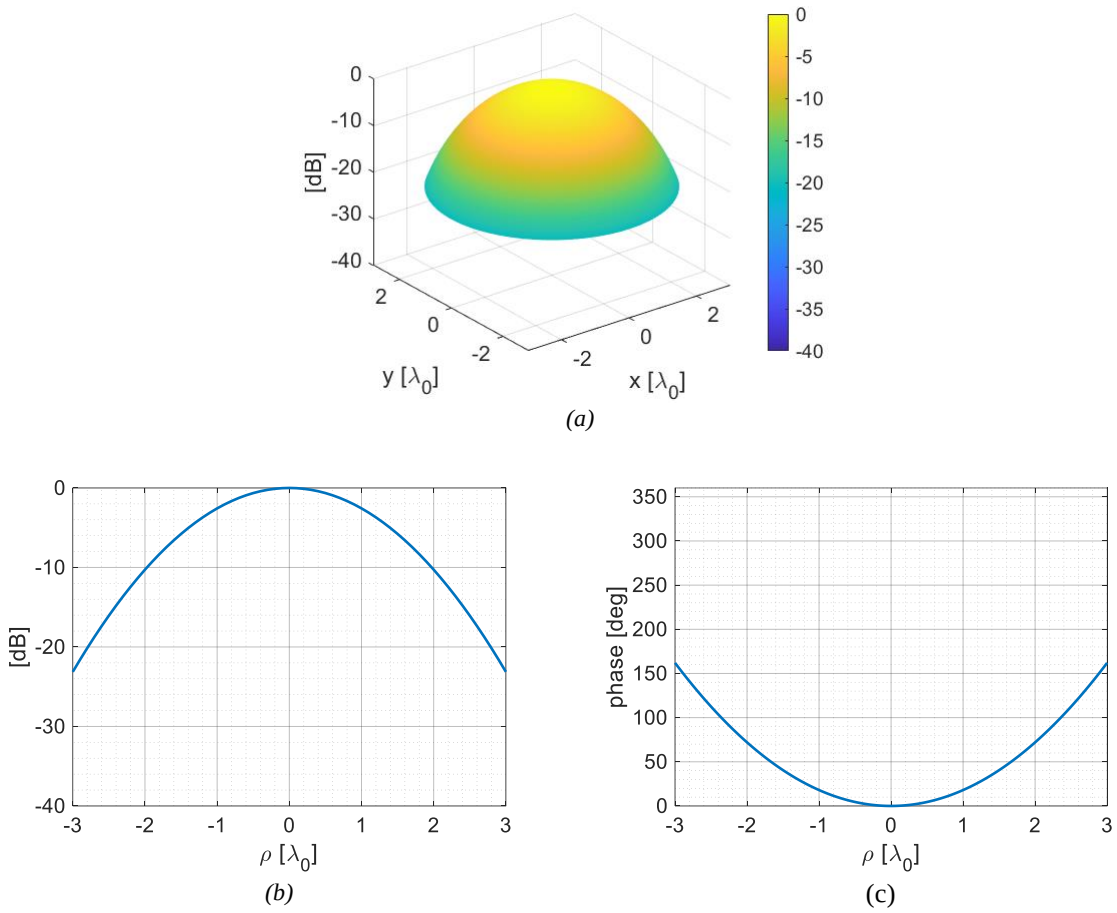

Figure 3.13 The amplitude of the fixed ideal current distribution in (a) 2-D and (b) 1-D and the (c) phase distribution

The field radiated by this current is shown in Figure 3.7(a).

With the fixed ideal current shown in Figure 3.13, the channel matrix of fixed ideal current and the one of uniform current at 270GHz calculated according to eq. 2.41 are shown in Figure 3.14.

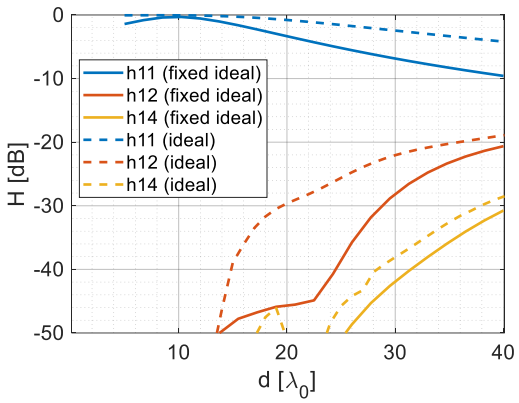

Figure 3.14 The channel matrix of the fixed ideal current distribution (solid lines) and the one of the ideal current distribution (dash lines)

From Figure 3.14, compared with the channel matrix of the ideal current, the channel matrix of fixed ideal current has a better suppression on the interference levels h_{12}, h_{13} and h_{14}. As for the coupling, h_{11}, the fixed ideal current distribution has less coupling than the ideal current.

Based on the eq. 2.52 and the channel matrix of the fixed ideal current in Figure 3.14, assuming the spectral channel matrix is constant at the channel matrix at 270GHz, the capacity at 270GHz of the fixed ideal current is calculated, shown in Figure 3.15. the capacities of the uniform current and the ideal current from Figure 3.12 are also plotted to compare.

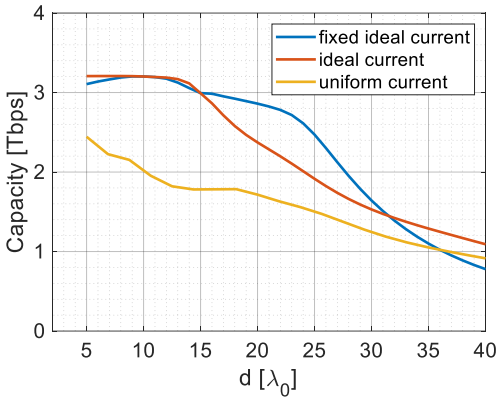

Figure 3.15 The capacities of the fixed ideal current (blue line), ideal current (red line) and uniform current (yellow)

From Figure 3.15, compared with the capacity of ideal current, the capacity of fixed ideal current has almost the same capacity when the distance between two arrays $d < 15\lambda_0 = 0.21d_{ff}$, but the high capacity remains farther distance, to $d = 25\lambda_0 = 0.35d_{ff}$ where the capacity of the ideal current already drop after $d = 15\lambda_0 = 0.21d_{ff}$. Compared with the capacity of the uniform current, the capacity of the ideal distribution is approximately double that of the uniform distribution in the interested range.

From the capacity shown in Figure 3.15, we find that the ideal current is not the optimal current in the interested range $d \in [10\lambda_0, 30\lambda_0]$ in MIMO scenario, and a fixed current can provide even better capacity.

3.5.2 Parametric Study

We found that a fixed ideal current is helpful to further increase the capacity in the interested range compared with the ideal current in Section 3.5.1, but the choice of the fixed parameters was not justified. We will do the parametric study in this section to find the optimal parameters to fix the ideal current distribution. According to eq. 2.50, the capacity depends on the SNIR, and the highest capacity is equivalent to the highest SNIR. We are going to study the SNIR and find the distribution with the best SNIR, and calculate the corresponding capacity.

According to the definition of the ideal current distribution, the ideal current depends on the link distance between Tx and Rx apertures d. Since the interested range is $d \in [10\lambda_0, 30\lambda_0]$, we are going to fix the distribution at three distances: $d = 10\lambda_0, 20\lambda_0, 30\lambda_0$. The SNIRs of these three current distributions are calculated as eq. 2.47, shown in Figure 3.16.

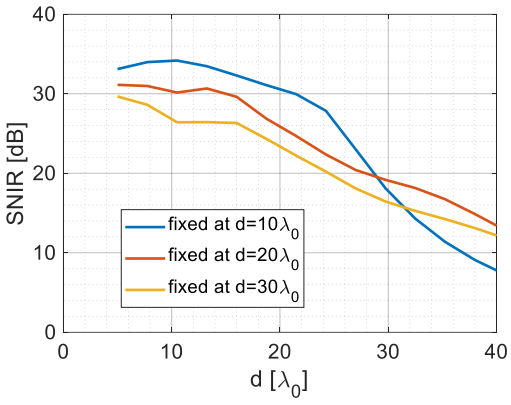

Figure 3.16 The SNIRs of the ideal current fixed at $d = 10\lambda_0$ (blue solid line), $d = 20\lambda_0$ (red solid line), and $d = 30\lambda_0$ (yellow solid line)

From Figure 3.16, in the interested range $d \in [10\lambda_0, 30\lambda_0]$, the current fixed at $d = 10\lambda_0$ have highest SNIR than the other two, and we know that we want to find the fixed point somewhere between $10\lambda_0$ and $20\lambda_0$. We will then look into smaller steps in this range. Figure 3.17shows the SNIR of the current fixed at $d = 10\lambda_0, 11\lambda_0, 12\lambda_0, 13\lambda_0, 14\lambda_0, 15\lambda_0$.

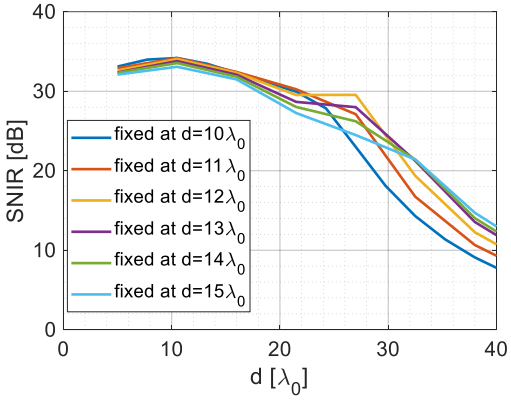

Figure 3.17 The SNIRs of the ideal current distribution fixed at $d = 11\lambda_0$~$15\lambda_0$

From Figure 3.17, we find that the current optimized at $d = 12\lambda_0$ has the best SNIR, where the current optimized at $d = 11\lambda_0$ and $d = 13\lambda_0$ has less SNIR, but not much less. Here, we fix the amplitude and the phase both at one distance, but it might be helpful to select different distances to fix for the amplitude and phase distribution. We call the distance to fix the amplitude as amplitude distance d_a, and the distance to fix the phase as phase distance d_p. Since we already find that the optimized range should be

in $d \in [10\lambda_0, 15\lambda_0]$, we will set the amplitude distance d_a and the phase distance d_p in this range. Figure 3.17 shows the SNIR of some group of distances.

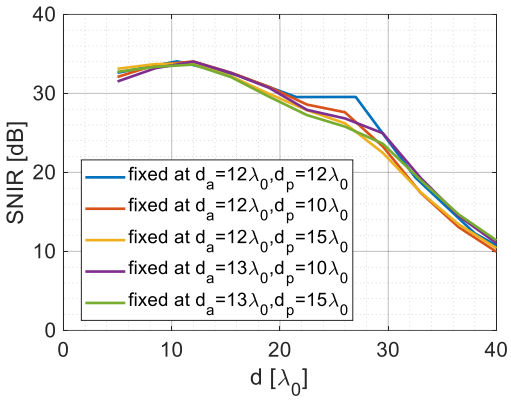

Figure 3.18 The SNIRs of a set of chose parameters

From Figure 3.18, we find that the ideal current fixed at $d_a = 12\lambda_0$ and $d_p = 12\lambda_0$ is the best current. However, this requires a taper level of 19 dB, which is quite hard to realize with a lens antenna. Therefore, we decided to choose the parameter groups: $d_a = 13\lambda_0$ and $d_p = 10\lambda_0$. This requires the taper level to be -16dB, which is achievable.

It is easier to define this current distribution based on its physical meaning. This current has a Gaussian distribution in amplitude with a taper level of -16dB, focusing at a distance $d = 10\lambda_0$. This current distribution with these parameters is named as the optimized current distribution in the following part of this thesis.

Its amplitude and phase distributions of the optimized current distribution are shown in Figure 3.19.

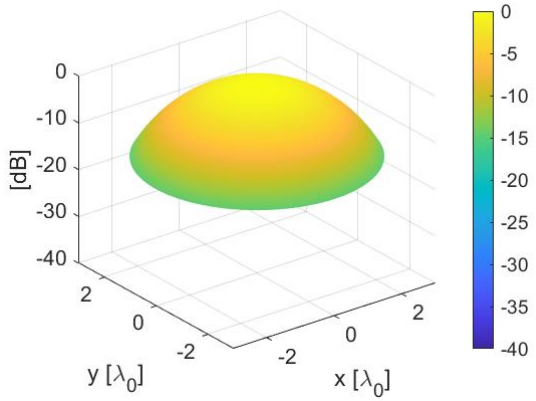

Figure 3.19 The amplitude of the optimized current distribution in 2-D

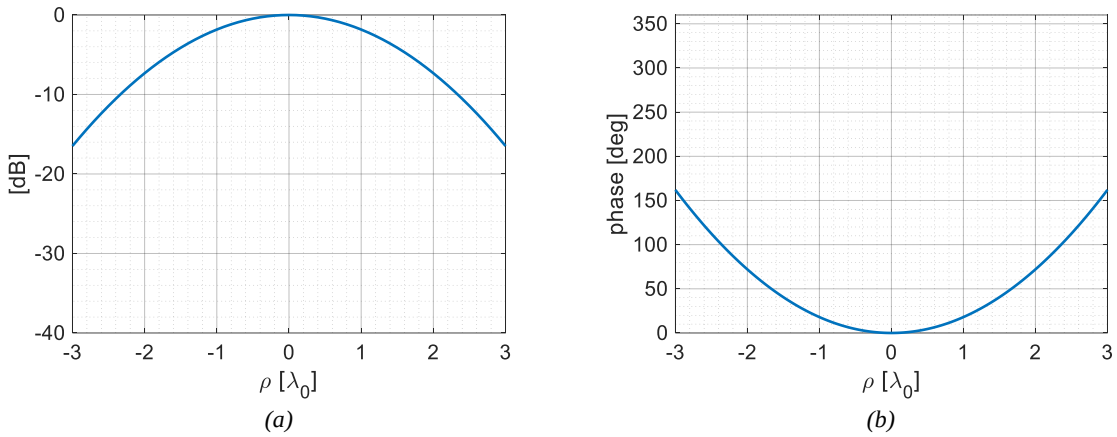

Figure 3.20 The (a) amplitude and (b) phase of the optimized current distribution in 1-D

Figure 3.20 shows the optimized current distribution with 16dB taper in amplitude and 160° phase level. The current calculated from eq. 2.12 and 2.13 with this optimized current distribution in Figure 3.19 and Figure 3.20 is called as optimized current in this thesis. The electric field radiated by this optimized current at 270GHz is shown in Figure 3.21.

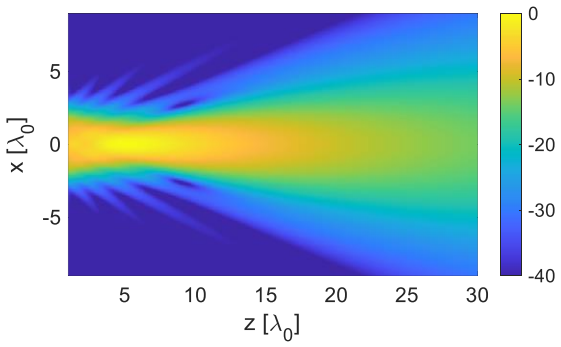

Figure 3.21 The electric field radiated by the optimized current in the radiative near field

In Figure 3.21, the field has a wide main lobe and has almost no side lobe in the radiative near field.

The channel matrix of the optimized current and one of the uniform current at 270GHz over link distance is shown in Figure 3.22.

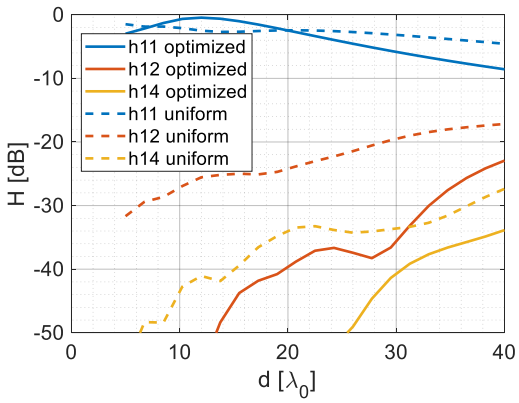

Figure 3.22 The channel matrices of the optimized current (solid lines) and the uniform current (dash lines)

In Figure 3.22, h_{11} is the co-coupling, h_{12} and h_{14} are the interferences. Compared with the channel matrix of uniform current, the co-coupling h_{11} of optimized current is higher in range $d \in$

$[10\lambda_0, 20\lambda_0]$, but lower in range $d \in [20\lambda_0, 30\lambda_0]$; the interferences h_{12} and h_{14} of optimized current are better suppressed over the entire distance range. With the results from Figure 3.22, we can calculate the capacities of the optimized current and the uniform current according to eq. 2.50 and the parameter introduced in Chapter 2 with the channel matrix at 270GHz. Figure 3.23 shows the capacity of the optimized current at 270GHz. We also plot the capacities of the ideal current and uniform current at 270GHz from Figure 3.12 to compare.

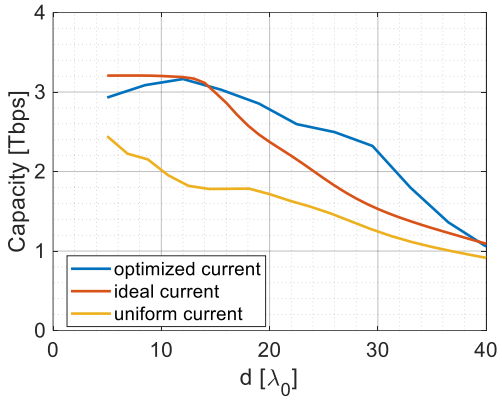

Figure 3.23 The capacities of the optimized current distribution (blue), ideal current distribution (red) and uniform current distribution (yellow) at 270GHz

In Figure 3.23, the capacity of the optimized current is more or less double than the one of the uniform current, shows a significant improvement over the entire consider range. Compared with the ideal current, the capacity of optimized current works better in range $d \in [20\lambda_0, 30\lambda_0]$. With the optimized current, the capacity reach around 3Tbs over the interested range.

3.5.3 Frequency Behaviour of the Optimized Current Distribution

We discussed the performance of the optimized current at the center frequency. However, the performance changes over different frequencies. Now, we will study the frequency behavior over the frequency band [235GHz, 305GHz]. Since we already reached the best performance at the center frequency by parameter study, we want the channel matrix and the capacity of this current distribution at other frequencies as good as the ones at the center frequency, which means we want the performance to be frequency-independent. However, this is impossible because the radiation of the current is frequency-dependent according to eq. 2.21 and 2.22. But we still want the frequency-dependence to be as low as possible. So it is essential to check the frequency-dependence. we will plot the channel matrix over frequency at $d = 10\lambda_0$ and $d = 30\lambda_0$ of the optimized current and the uniform current to check the frequency-dependence, shown in Figure 3.24.

The optimized current distribution at each frequency is calculated as eq. 3.33. From this equation, the amplitude distribution is fixed over frequency, -16 dB taper with Gaussian distribution; the phase term $e^{-\frac{jk_0|\vec{\rho}'|^2}{2d}}$ is changed with frequency, but its physical meaning is always focusing at $10\lambda_0$.

Since we know that h_{11} represent the co-coupling, and h_{12} and h_{14} are the interferences, and we already knew the level of h_{12} and h_{14} in section 3.5.2, we will plot the level of the co-coupling and the one of interference here to check the frequency-dependence.

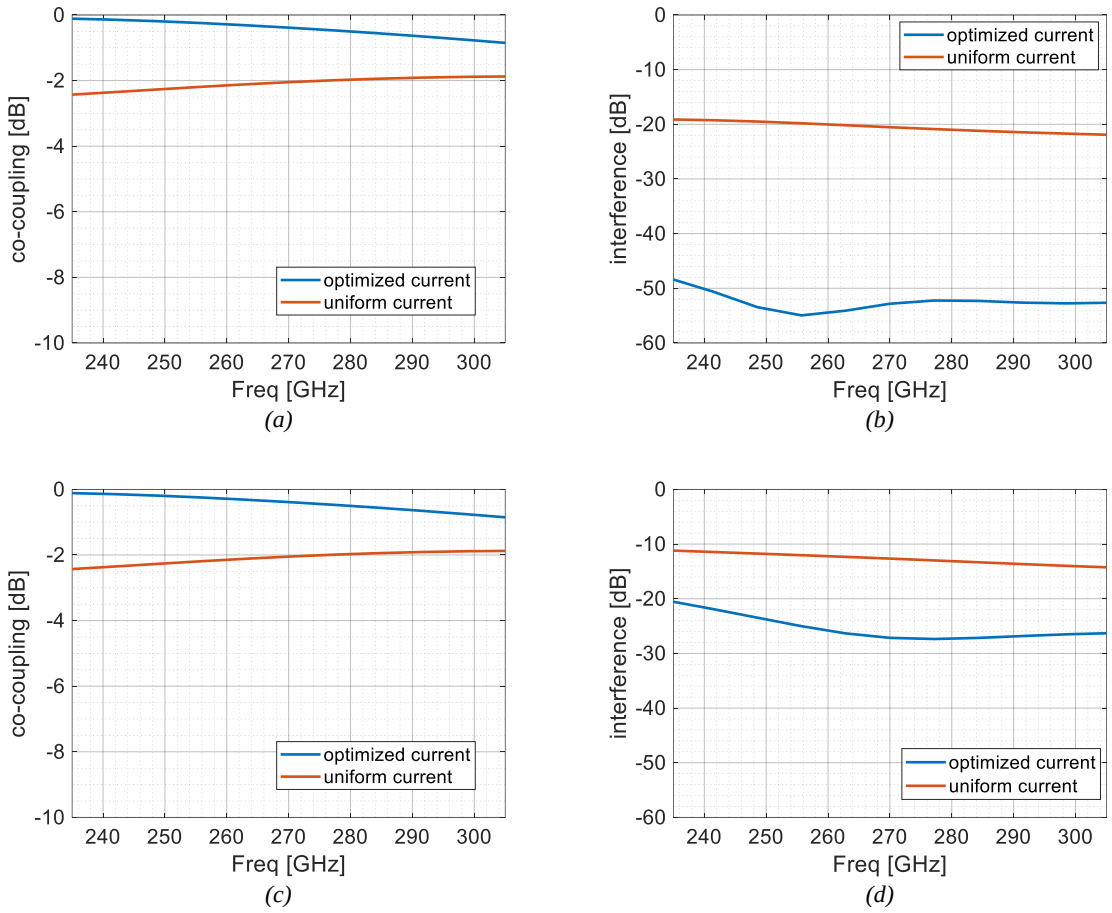

Figure 3.24 The co-coupling levels at (a) $d = 10\lambda_0$ and (b) at $d = 30\lambda_0$, and the interference levels at (c) $d = 10\lambda_0$ and (d) at $d = 30\lambda_0$ of optimized current (blue solid line) and uniform current (red solid line) over frequency

From Figure 3.24, the co-coupling and the interference levels over frequency is relative stable over frequency, changing smoothly. With these co-coupling and interference levels, we can calculate the capacities of optimized current and uniform current, and compare them with the ones at 270GHz, shown in Figure 3.25.

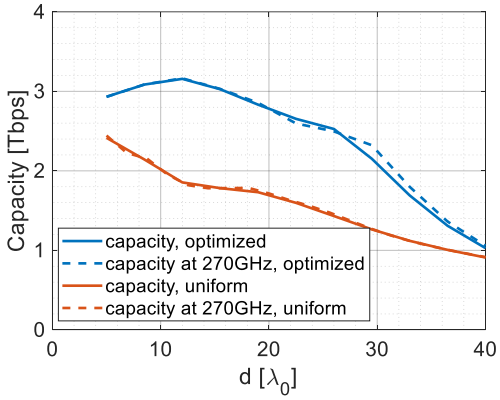

Figure 3.25 The capacities at 270 GHz (dash lines) and spectrally capacities (solid lines) of the optimized current (blue lines) and the uniform current (red lines)

From Figure 3.25, the capacities of the of optimized current and uniform current have negligible frequency-dependence, which is as what we expect. With these results, we can confidently use this optimized current in our frequency band and assume it is frequency-independent. However, this

simulation assumes that the current distribution is unchanged over frequency, which is impossible if we implement an antenna to approximate the current. The design of the antenna will be shown in Chapter 4.

4 Lens Antenna Design

In Chapter 3, we found the optimized current to provide the maximum capacity in the interested distance range. In this chapter, we are going to design a lens antenna to synthesize and then validate the optimized current. The scope is to validate the model with full-wave simulations and study the impact of multiple reflections and scattering. As done in the previous chapters, we want to use the uniform current as a reference. Therefore, we want to have a lens antenna design for this uniform distribution as well. For this scope, we would use leaky-wave elliptical lens antennas [21]. These antennas can generate equivalent current with different distributions (e.g., uniform distribution, Gaussian distribution, etc.) with uniform phase on a circular aperture. To have a focusing antenna in the near-field, a hyperbolic lens will be designed on top of the leaky-wave elliptical lens antennas.

In Section 4.1, we will introduce and revise the principle of operation of an elliptical lens antenna with leaky-wave (LW) feed; in Section 4.2, we will describe the design methodology used to realize the desired currents; in Section 4.3, we present the design and validation of the lens antenna to synthesize the uniform current distribution; whereas in section 4.4, we will present the design and validation of the lens antenna to synthesize the optimized current distribution; finally in Section 4.5, the estimation of the capacity will be shown.

4.1 LW Lens Antennas

LW antennas are one type of the commonly used quasi-optical antennas in high-frequency applications. They achieve high aperture efficiency and low losses by illuminating the upper part of the lens with a directive primary beam [21][22]. Due to the high directivity in this primary pattern and its low loss properties, they have been widely used in multiple application areas such as Fly's eyes[22] and lens phased array [23].

A LW elliptical lens antenna consists of a LW feed (usually fed by Double-slot antennas [24] or waveguide aperture [25] with a resonant air cavity) with an elliptical lens integrated on top and the phase center of the LW feed located at the lower focus of the elliptical lens surface. The geometry of the LW elliptical lens antenna is shown in Figure 4.1. The LW feed consists of a half-wavelength air cavity between the ground plane of the feeds and the semi-infinite dielectric with relative permittivity of ϵ_r. This LW feed allows the propagation of the TM_1/TE_1 LW modes, which will contribute to radiate more directive beam, and this directive beam will help us to avoid the critical angle problem present in integrated antennas. The maximum angle θ_{max} represents the angular truncation of the lens. The largest truncation angle is related to the critical angle of the elliptical lens. The fields that are illuminated out of the maximum truncation angle θ_{max} cannot propagate parallelly to the broadside, which means that only the fields with illuminating angle $\theta < \theta_{max}$ are effective. A LW feed radiates most of the energy below this critical angle [22] and, therefore constitutes an efficient feed for integrated lenses. Moreover, LW feeds are helpful for primary beam shaping for different applications (i.e., higher aperture efficiency lens [22][23] or lens antenna with Gaussian beam [26]).

The LW air cavity also allows the propagation of the TM_0 mode. This mode is nearly independent of frequency and the thickness of the air cavity. The angular radiation peak of the TM_0 LW mode is at larger angles and therefore will decrease the illumination efficiency of the lens. Therefore, one needs a good suppression of the TM_0 mode. It is possible to suppress this mode by choosing the correct feed, such as in [1, 2, 3, 6].

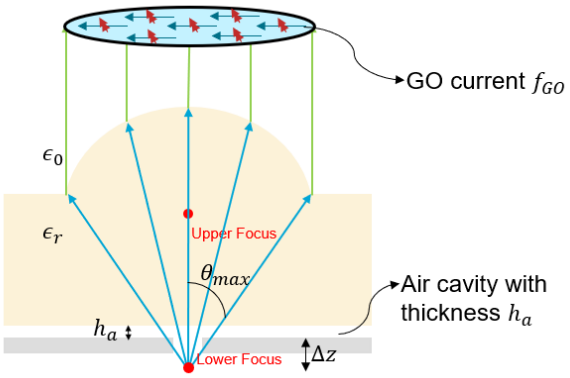

Figure 4.1 An example of the elliptical lens antenna

Several feeding structures for the LW lens antenna provide good suppression of the TM_0 mode, such as the double iris-slots antennas [22] and waveguide aperture with corrugations [23], which are widely used in the lens antenna design. The current distribution on the feeding aperture of the double-slot iris antennas can be analytically defined, which makes it more convenient to design. The geometry of the double-slot iris feed is shown in Figure 4.2.

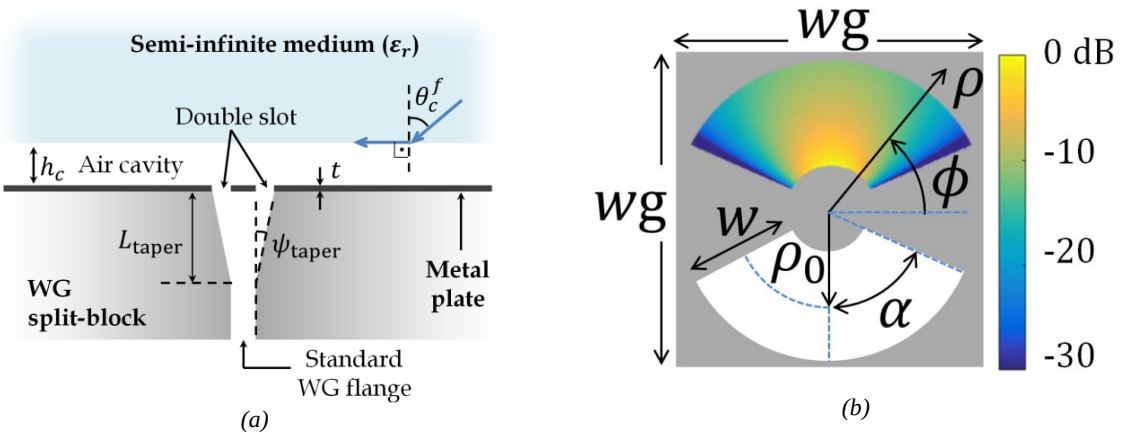

Figure 4.2 The geometry of the double-slot iris feed in (a) side view and (b) top view [2]

And the current distribution of the analytically approximated as [22]:

$$\vec{m}_s(\rho,\phi) \approx \frac{1}{\rho}\cos\left[\frac{\pi}{2\alpha}\left(\phi \pm \frac{\pi}{2}\right)\right] rect\left(\phi \pm \frac{\pi}{2}, 2\alpha\right) rect\left(\rho - \frac{\rho_0}{2}, w\right)\hat{x} \qquad [4.1]$$

All the parameters are displayed in Figure 4.2.

Previously, these LW lens antennas have been designed to achieve high aperture efficiency, which can approximate the uniform current distribution. We will scale the design of [23] as the reference for the uniform current distribution, which will be discussed in 4.3. Then, we will design the lens antenna to approximate the optimized current distribution following the methodology described in 4.2.

4.2 Lens Antenna Design Methodology

In this section we will describe the design and verification methods of the lens antenna.

4.2.1 GO Current Evaluation

The Geometrical Optics (GO) technique is commonly used in high-frequency scattering scenarios. The scattered fields can be approximated by only the transmitted fields when the scatter surface is electrically large enough (for elliptical surface, $D_l > 3\lambda$). In this method, the EM waves are approximated in terms of ray's propagation, allowing us to evaluate the radiation of the lens antenna asymptotically.

The ray's propagations inside and outside of the lens are related, and the relationship between the inside and outside is the transmission and reflection on the lens surface. The transmission and reflection on the lens surface are modelled as the flat-surface-incident for each ray in the GO tool [26] analytically. This allows us to study the radiation of the lens antenna with only the primary field inside the dielectric lens analytically. We can use the GO fields $\vec{E}_{GO}$ and $\vec{H}_{GO}$ on top of the lens antenna to evaluate the radiation effect, where the aperture of the GO field is circular aperture, having the same diameter as the lens. The GO field is shown in Figure 4.1. When the feed is located at the focus of the lens, the aperture GO fields can be modeled analytically using the following expression [22]:

$$\vec{E}_{GO}(P) = \tilde{T}(Q) \cdot \vec{E}_p(Q) S(Q) e^{-jk_0 r'} \quad [4.2]$$

$$\vec{H}_{GO}(P) = \frac{1}{\zeta_0} \hat{r}' \times \vec{E}_t(P) \quad [4.3]$$

Where $\vec{E}_p(Q)$ is the primary source radiate the primary field inside the dielectric, $\tilde{T}(Q)$ is the transfer function on the lens surface and $S(Q)$ is a spreading factor. The derivation and calculation eq. 4.2 and 4.3 are detailly introduced in [28], known as the GO model.

In the GO model, the propagation from the primary field inside the antenna to the GO aperture field is done. Then, applying the equivalence theorem, we can have the equivalent current on the lens aperture:

$$\vec{J}_{GO} = \hat{z} \times \vec{H}_{GO} \quad [4.4]$$

$$\vec{m}_{GO} = -\hat{z} \times \vec{E}_{GO} \quad [4.5]$$

Where $\hat{z}$ is the broadside direction of the lens antenna, $\vec{J}_{GO}$ and $\vec{m}_{GO}$ are the equivalent electric and magnetic currents respectively, named as GO current.

The GO tool models the transmission through the elliptical surface using the primary fields radiated by the feed in the far field. The far field of the feed in the dielectric can be evaluated analytically using well-known spectral domain methods. The field can then be expressed via a spectral Green's function and the FT of the current distribution, such as [22]. The radiated feeds can then be evaluated using the transmission line model in stratified material as shown in Figure 4.3.

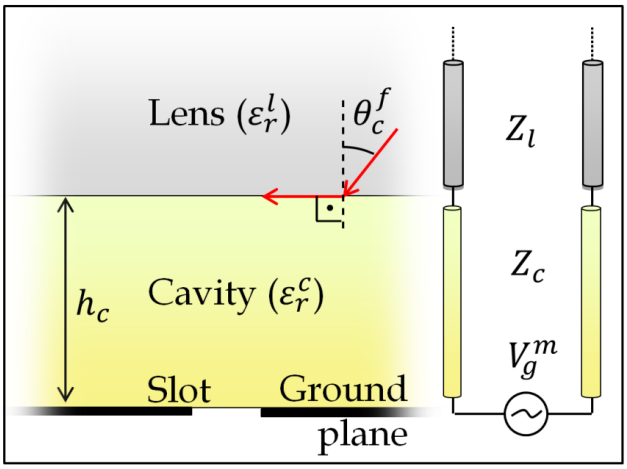

Figure 4.3 Transmission line model in stratified material [29]

Where the lens material is semi-infinite and the current distribution on the Slot is known.

Then, applying the spectral Green's function (SGF), the primary field is calculated as follows (only show the electric fields radiated by the electric current):

$$\vec{E}(\vec{r}) = \frac{1}{(2\pi)^2} \iint_{-\infty}^{\infty} G_{SGF}^{ej}(k_x, k_y, z, z') J_{FT}(k_x, k_y) e^{-jk_x x} e^{-jk_y y} dk_x dk_y \qquad [4.6]$$

Where $\vec{r}$ is the vector from the far field observation point to the source, G_{SGF}^{ej} is the SGF, J_{FT} is the FT of the current, k_x and k_y are the x and y component of the propagation constant.

GO model approximate the transmission through the elliptical surface, and the spectral domain methods analytically calculate the primary fields radiated by certain feed current distribution inside of the lens. These two approaches allow us to design only the feed, and then, with the defined geometry of the lens, we can adjust the GO current distribution by only adjusting the feed geometry. This whole process can be done analytically and efficiently in MATLAB.

Now, the lens antenna is modeled as the equivalent current on the circular aperture with the same diameter as the lens. If we set the lens diameter D_l the same as the diameter of the theoretical current distribution we will synthesize, D_{ap}, we can design the lens antenna by comparing the difference between its GO current and the theoretical current.

4.2.2 Methodology

In Section 4.2.1, we described the evaluation of the GO current defined over a circular aperture on top of the lens with the same diameter. This GO current can be analytically calculated in MATLAB with the given geometry of the lens and the feed. We also understood that we could design the lens antenna by comparing the difference between the GO current and the theoretical current. In this section, we will introduce the lens antenna design methods and steps, and then to introduce the terms that we need to compare.

Let us first focus on the lens antenna design. The optimized current distribution in Chapter 3 contains both amplitude term (-16dB Gaussian taper) and phase term (focusing at $10\lambda_0$). To synthesize this current distribution, we will implement an elliptical lens antenna to approximate the amplitude distribution with a uniform phase, and then use a hyperbolic lens antenna to approximate the phase focusing term.

The design of the elliptical lens antenna is done in MATLAB. This process contains two parts: to calculate the primary fields radiated by the LW feed and to calculate the GO current based on the primary fields. The Geometry of the LW lens antenna and the current distribution of the double-slot iris feed are shown in Figure 4.1 and Figure 4.2 respectively. The diameter of the lens antenna D_l is set as the same as the diameter of the aperture D_{ap}, and the rest of the antenna design is basically to play with the parameters shown in Figure 4.1 and Figure 4.2. The final design of the elliptical lens antenna has aims at having a GO current distribution close to the amplitude of the optimized current distribution in Section 3.5. Moreover, the reflection coefficient of the feed Γ should be less than -10dB. This designing process will be described in Section 4.4.

The hyperbolic lens antenna is located on the GO aperture of the elliptical lens antenna to provide the near-field focalization. Its focusing performance is frequency-independent and only depends on the material and the curve. Its parameters can be designed analytically. The analysis of the hyperbolic lens antenna is implemented in FW simulation in CST. Before that, to still study analytically the designed antenna, we are going to trust the performance of the hyperbolic antenna and use a theoretical phase term as the phase distribution contributed by the hyperbolic antenna. In other words, the GO current of the entire antenna system is the product of the GO current of the elliptical lens antenna and the theoretical focusing phase term:

$$f_{GO} = f_{GO}^{ell} e^{-\frac{jk_0|\vec{\rho}'|^2}{2\cdot 10\lambda_0}} \quad [4.7]$$

Where f_{GO}^{ell} is the GO current of the elliptical lens antenna, k_0 is the propagation constant in free space, and $\vec{\rho}'$ is the radius on aperture plane. We will then call f_{GO} as the focused GO current in the rest of this thesis. f_{GO} is actually a function of frequency, because the GO current of the elliptical lens antenna f_{GO}^{ell} changes over different frequencies, and the phase term $e^{-\frac{jk_0|\vec{\rho}'|^2}{2\cdot 10\lambda_0}}$ also contains frequency-dependent term k_0. Even the phase term contains frequency-dependent term k_0, its physical meanings at different frequencies are always to focus at $d = 10\lambda_0$.

Since the GO current of the elliptical lens antenna varies with frequency, we will match the focused GO current at the center frequency 270GHz to the optimized current distribution first. Assuming that we successfully design a lens antenna, our next step is to compare the difference between the focused GO current of the lens antenna and the amplitude of optimized current distribution at the center frequency. It is not enough to only compare the distribution, we also need to compare the field radiated in the far field and the near field, and to calculate the channel matrix over distance with eq. 2.40, as what we did for the optimized current distribution in Figure 3.22. For our convenience, we will only compare the distribution of the electric current of the GO current with the optimized current distribution, and only compare the electric field radiated by the GO current with the one radiated by the optimized current.

Since the hyperbolic lens antenna is frequency independent, the GO current of the elliptical lens antennal f_{GO}^{ell} is the term that varies over frequency. To study the frequency behavior of the lens and calculate the channel matrix of the focused GO current over frequency, we need to calculate the focused GO currents at different frequencies from eq. 4.7, and then apply these focused GO currents at different frequencies to calculate the channel matrix at different frequencies.

4.3 Lens Antenna for Uniform Distribution

As introduced in Section 4.2.2, we will use the LW elliptical lens antenna proposed by [23] to synthesize the uniform current distribution. Although this antenna is an existing design, it is still necessary to introduce the parameters and to analyse its performance, as shown in Section 4.3.1 and Section 4.3.2 respectively. Then, in Section 4.3.3 we will introduce the CST simulation results.

4.3.1 Design Process and Final Parameters

This design from [23] is shown in Figure 4.4. The lens antenna is fed by a circular waveguide with corrugations. The lens material is high density poly-ethylene (HDPE), with relative permittivity$\epsilon_r = 2.3$, the leaky-wave air cavity is $h_a = \frac{\lambda_0}{2}$, the truncation angle is $\theta_{max} = 36.5°$, dimension of the circular waveguide $d_{wg} = 0.95\lambda_0$ and the phase center is $\Delta z = -0.66\lambda_0$. as mentioned before, LW lens antennas need a good suppression on the TM_0 mode to provide high aperture efficiency, and the suppression techniques used in this paper [23] is to add corrugations on the ground plane. According to multiple simulations [23], 8 corrugations with parameters: $d = 0.33\lambda_0$, $p = 0.23\lambda_0$, $w = 0.11\lambda_0$, $r_0 = 0.69\lambda_0$ can provide optimal suppression of the TM_0 leaky-wave mode. All the parameters are displayed in Figure 4.4.

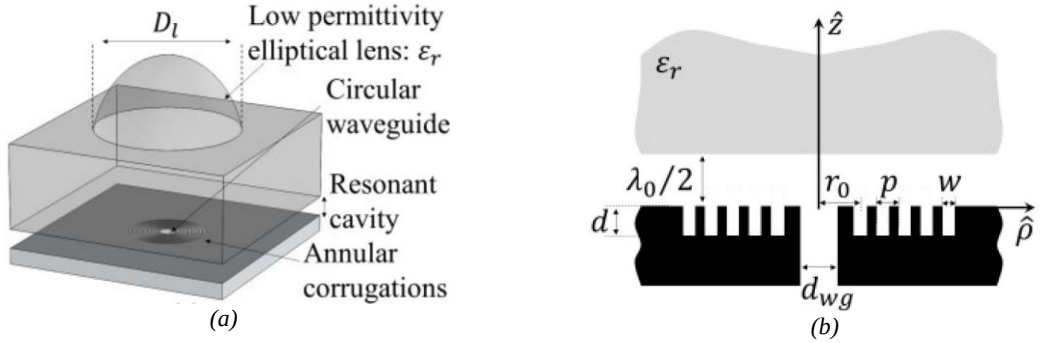

Figure 4.4 The (a) elliptical lens and (b) its feed in [23]

Since the frequency band and aperture diameter are different in our design, all design parameters which are dependent on the frequency and the lens diameter must be scaled. The dimensions of the design are scaled to fit our frequency band $f \in [235,305]GHz$ and the diameter of the lens is set to $D_l = 6\lambda_0$.

In addition to the design of [23], to decrease the effect of reflections, a matching layer (ML) is added on top of the lens cap, with relative permittivity $\epsilon_{rm} = 1.51$ and thickness $h_m = \frac{\lambda_m}{4}$, where λ_m is the wavelength in the ML material. Since we are not going to fabricate, we chose the relative permittivity of the ML as the theoretically optimal permittivity ϵ_{rm}, but did not consider whether this material exists in the real world. A perfect electric conductor (PEC) is placed surrounding the lens aperture to have a more accurate validation with the previously described GO model. The view of this lens antenna in CST is shown in Figure 4.5.

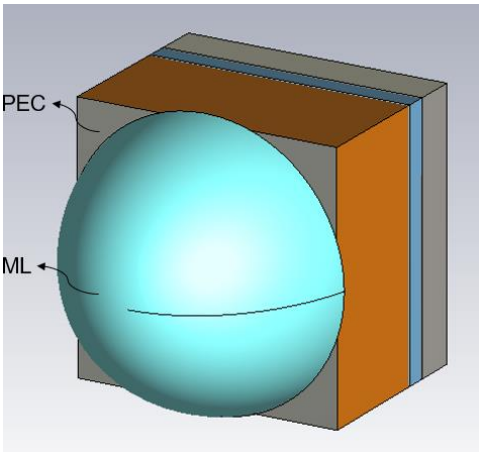

Figure 4.5 The view of the lens antenna to synthesize uniform currents in CST

4.3.2 GO Aperture Performance

In this section, we will evaluate the GO current of this antenna, and calculate the fields radiated by this GO current. We will also evaluate the channel matrix. All these simulations take place in MATLAB except for the primary fields. This is because that the primary field radiated by the LW feed with corrugations is not analytically modelled because of the presence of the corrugations, which means that we cannot calculate the primary field in MATLAB as described in Section 4.2.2. The primary fields of the LW feed are simulated via CST Microwave studio (called CST in the rest of the thesis), shown in Figure 4.6. To assume a semi-infinite dielectric, the background material is filled with dielectric, and the boundary conditions at the x, y, and z directions are all set as open. The frequency band is limited in $f \in [235GHz, 305GHz]$. The waveguide port is located one wavelength below the feed (in the waveguide), shown in Figure 4.6. The far field monitors at different frequencies are implemented to have the primary field information of this structure.

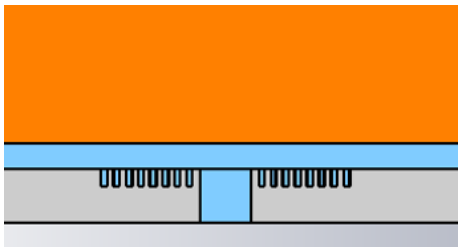

Figure 4.6 CST simulation of feeding structure

4.3.2.1 Performance at 270GHz

With the primary fields at each frequency from CST, using the GO tool, the GO current of this lens antenna at each frequency is calculated. We will first compare the current distribution of the GO current at the center frequency $f = 270GHz$. To the The amplitude and phase distribution of this GO current at $f = 270GHz$ are shown in Figure 4.7.

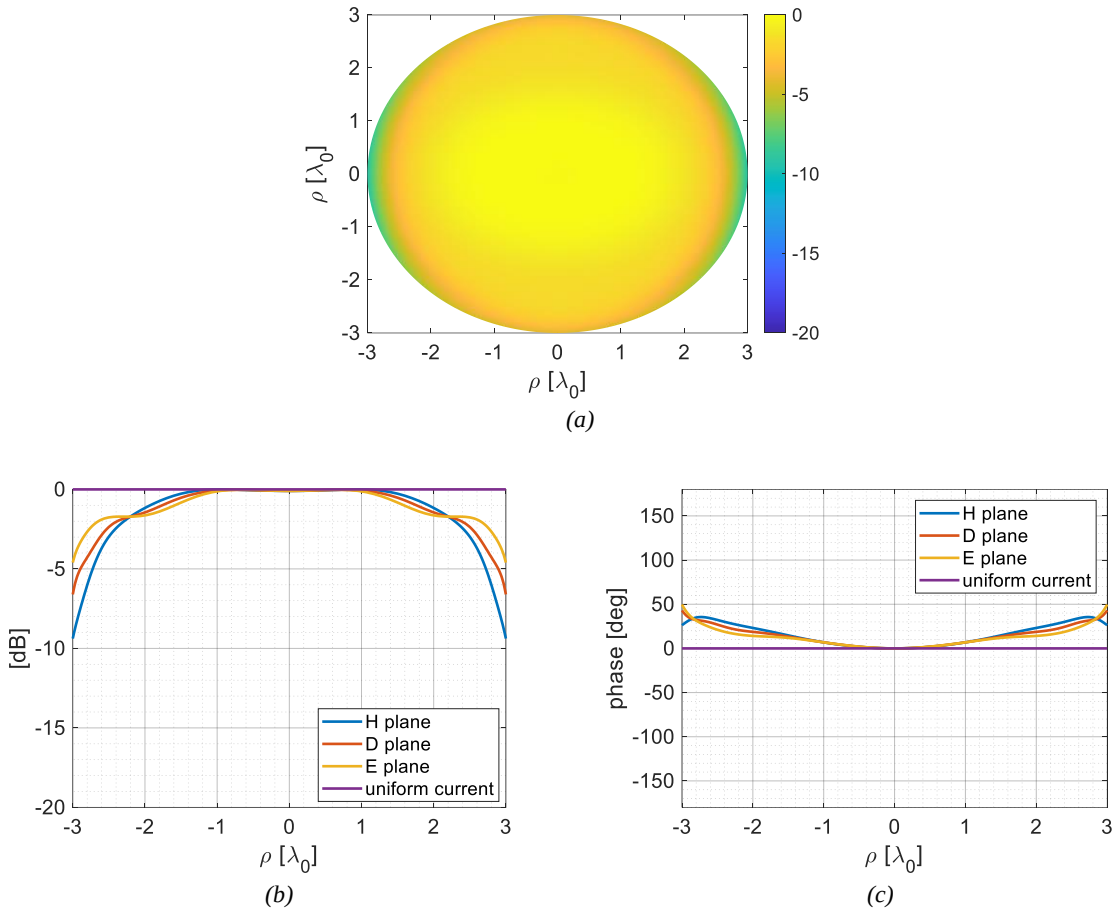

Figure 4.7 The amplitude (a) in 2-D, (b) in 1-D and the (c) phase of the GO current at 270GHz

From Figure 4.7, the amplitude and phase of the GO current are approximately distributed uniformly in both amplitude and phase. On the GO aperture, for the amplitude, the GO current is almost 0 dB in the radius range $\rho \in [0,2\lambda_0]$, and then decreases to -10 dB, -8 dB, and -6 dB at $\rho = 3\lambda_0$ in the H, D, and E planes respectively; the phase distribution have 40° phase variation; and both distributions in the E, D, and H planes are acceptably symmetry.

Now we know the GO current at 270GHz is similar to the uniform current distribution. Next, we will compare the difference between the electric field radiated by the GO current at 270GHz and the one radiated by the uniform current to the free space in the far field at $r = 1m$ and on a Rx aperture plane in the near field with link distance $d = 10\lambda_0$. These results are shown in Figure 4.8 and Figure 4.9 respectively. The black circles in Figure 4.9 are the Rx aperture position.

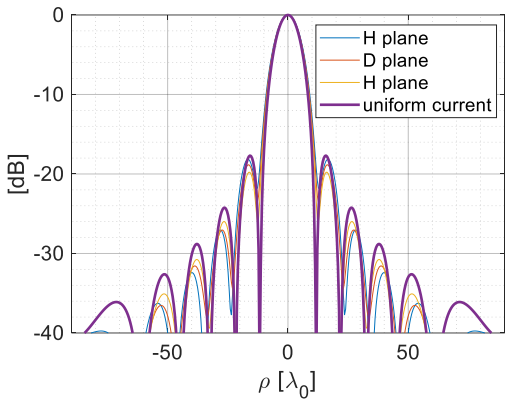

Figure 4.8 The far field pattern radiated by the GO current at 270GHz in H, D and H plane, and the far field radiated by the uniform current at 270GHz

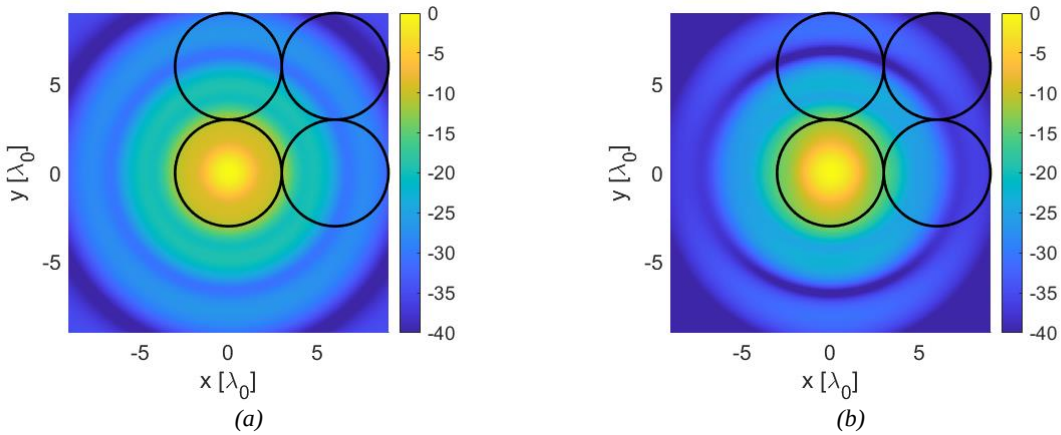

Figure 4.9 the field radiated by the (a) uniform current and (b) GO current at 270GHz on 2-D plane with distance of $10\lambda_0$

Since the uniform current is symmetric in the H, D and E planes, the far field of only the H plane is shown. From Figure 4.8, the far field patterns of the GO current are almost symmetric in the E, D, and H planes, and the far field patterns have similar directivity, side lobe, and main beam width to the Airy pattern. From Figure 4.9, the fields radiated by the uniform current and the GO current are similar on the plane with a near-field distance to the aperture. Figure 4.8 and Figure 4.9 show that the radiated fields of the ideal current and GO current are similar, and the difference is because the GO current is not entirely uniform current.

With the good agreement in both the current distribution and the radiated field in the far and near field at the center frequency 270GHz, we are confident to use the GO current at the center frequency to synthesize the uniform current. Figure 4.10 shows channel matrix agreement between the uniform current distribution and the GO currents of the used lens antenna, giving us enough confidence to use this antenna to synthesize the uniform current distribution. There are some differences between the interferences of these two currents when link distance is close, and then becoming more or less the same when arrays are farther.

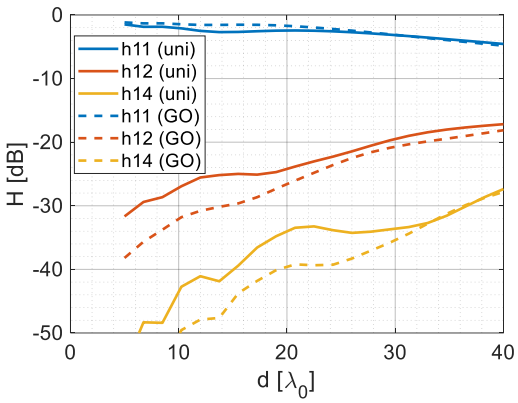

Figure 4.10 The channel matrix of uniform current and GO current at 270 GHz

4.3.2.2 Frequency Dependence

However, it is not enough to only study the channel matrix at the center frequency. We still need to study the frequency behavior over the entire frequency band. The first group of terms that we will study for the frequency behavior are the taper efficiency η_t, reflection efficiency η_{ref}, and spillover efficiency η_s. The taper efficiency η_t described the ratio between the directivity of the GO field and a uniform circular aperture, calculated as:

$$\eta_t = \frac{1}{A}\frac{\left|\iint_A \vec{E}_{GO}^{co}(\rho',\phi')dA\right|^2}{\iint_A \left|\vec{E}_{GO}(\rho',\phi')\right|^2 dA} \quad [4.8]$$

Where A is the aperture area, $\vec{E}_{GO}$ is the electrical field on the GO aperture, E_{GO}^{co} is the co-polarized field, ρ' and ϕ refers to the position on the aperture area. η_t can also be regarded as the similarity of the GO aperture to the uniform distributed aperture. The reflection efficiency η_{ref} is the efficiency of power reflected at the lens surface, and the spillover efficiency η_s is the efficiency of power captured by the lens surface in the truncation angle θ_0.

In general, the reflection efficiency and the spillover efficiency of the lens antenna refer to the loss, and both should be as high as possible. For the taper efficiency, the antenna to approximate the uniform current distribution should have taper efficiency as high as possible since the taper efficiency of uniform current is 1.

The product of these three efficiencies is the aperture efficiency:

$$\eta_{ap} = \eta_t \eta_s \eta_{ref} \quad [4.9]$$

And in this section, we want the aperture efficiency as high as possible. The efficiencies are calculated in GO tool over the entire bandwidth in MATLAB, shown in Figure 4.11.

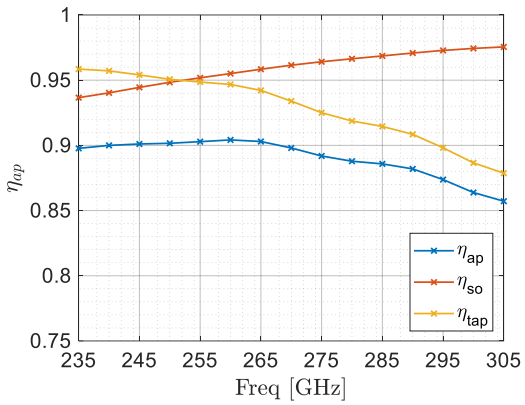

Figure 4.11 The aperture efficiency, spill over efficiency and taper efficiency of the GO current

From Figure 4.11, the antenna has high aperture efficiency over the entire operation frequency band, which means that this antenna should be able to synthesize the uniform current distribution over the entire operation band.

The GO current distribution changes with frequency. To study the frequency dependence, it is essential to see how the GO current distribution changes and the magnitude of this change. Figure 4.12 and Figure 4.13 shows the GO currents at 240GHz and 300GHz respectively. From Figure 4.12 and Figure 4.13, the change in the current distribution is not significant for our uniform lens, which gives us enough confidence to apply these GO currents at each frequency to calculate the channel matrix.

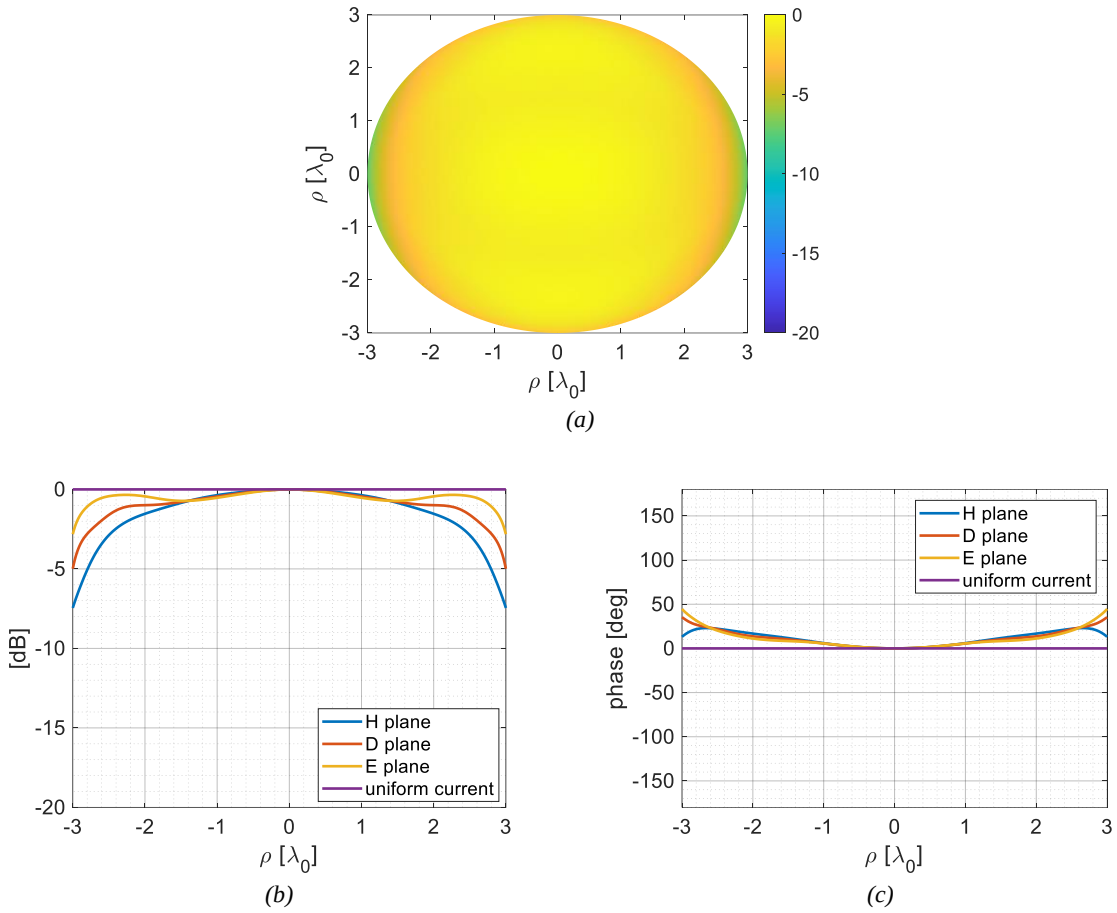

Figure 4.12 The amplitude (a) in 2-D, (b) in 1-D and the (c) phase of the GO current at 240GHz

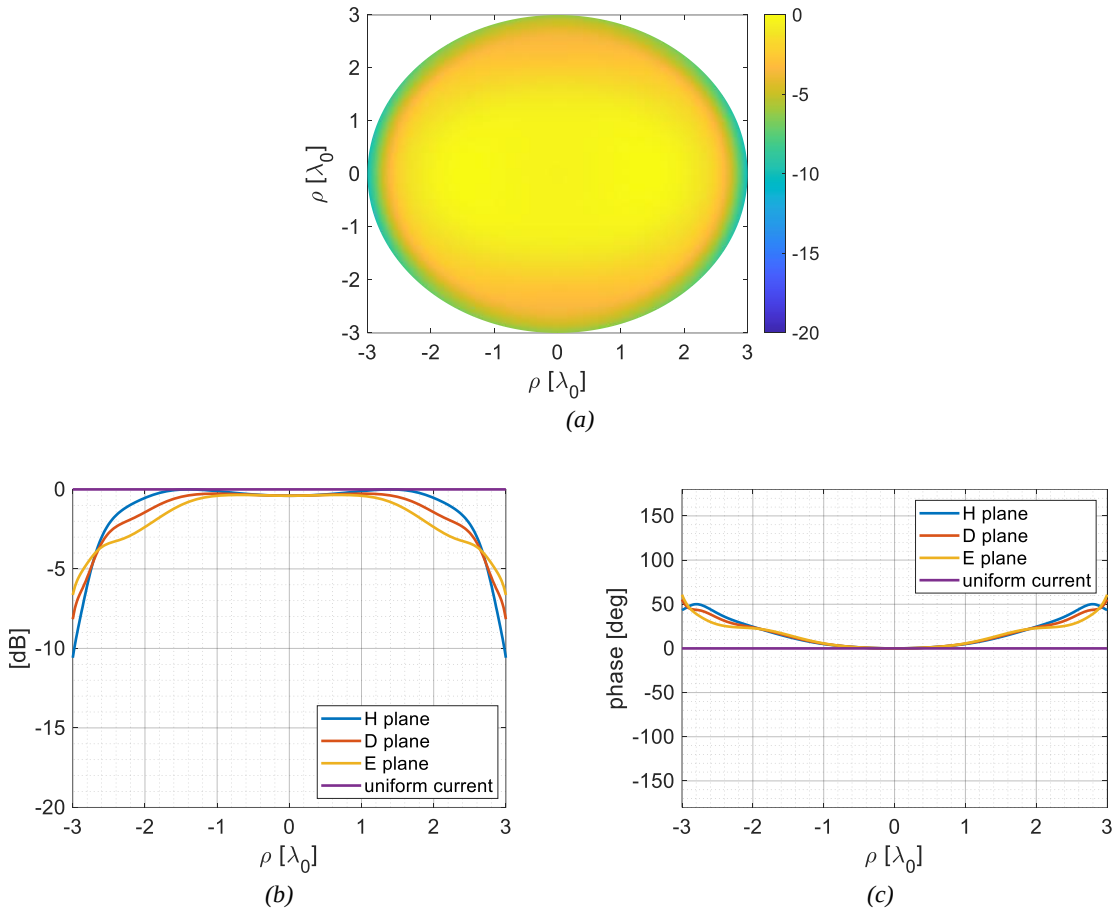

Figure 4.13 The amplitude (a) in 2-D, (b) in 1-D and the (c) phase of the GO current at 300GHz

With the GO currents at different frequency, we can calculate and compare the channel matrix of the uniform current distribution and of the GO current over frequency according to eq. 2.40. since our interested range is located in $d \in [10\lambda_0, 30\lambda_0]$, we choose three typical link distance $d = 10\lambda_0, 30\lambda_0, 30\lambda_0$ to study the coupling over frequency. When applying this equation, the uniform distribution does not change with frequency, but the GO current changes with frequency as shown in Figure 4.7, Figure 4.12, and Figure 4.13. The channel matrices of uniform current distribution and GO currents are shown in Figure 4.14.

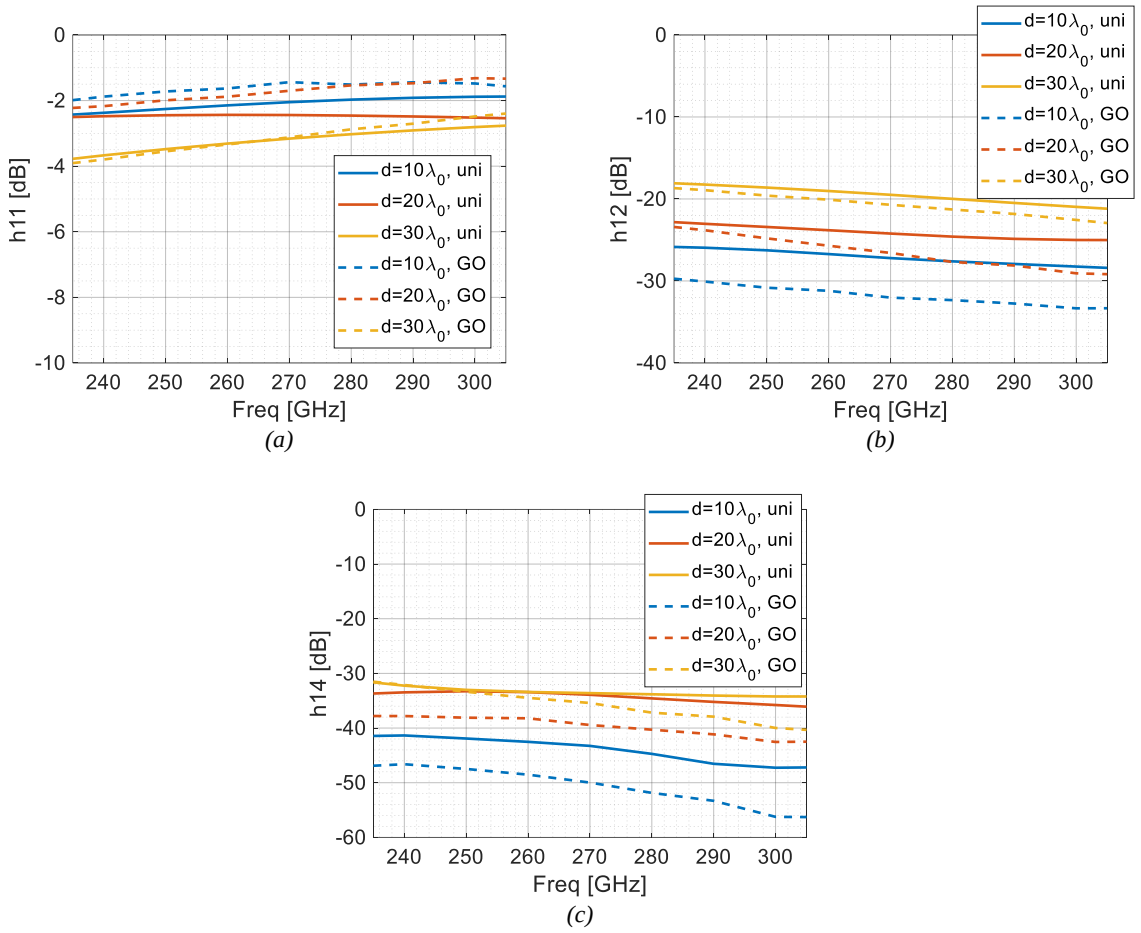

Figure 4.14 The (a) h_{11}, (b) h_{12} and (c) h_{14} of uniform current distribution (solid lines) and of GO current (dash lines) over three link distances

From Figure 4.14 the agreements of the coupling over frequency between the uniform current and the GO current are not good, with around 1dB difference in co-coupling term and 5dB difference in interference term. As mentioned before, this lens antenna [23] has a good agreements of radiation performance with the uniform current distributions. This tell us that in the near field, the study should be more accurate.

4.3.3 CST Simulations for Individual Lens Antenna

In this section, will study the results from CST simulation of individual lens antennas in reflection coefficient, far field and near field and radiation efficiency.

4.3.3.1 Reflection Coefficient

The reflection coefficient is an essential parameter in antenna design and should be at least lower than -10 dB to have less reflection loss at the port, and the reflection coefficient can only be simulated from CST. The simulation for the LW feed with infinite dielectric shown in Figure 4.6 above can provide us the reflection coefficient of this antenna. From the same simulation in Figure 4.6, we can have the S_{11} of the feeding structure, and this S_{11} is equivalent to the reflection coefficient Γ of this antenna, shown in Figure 4.15. From Figure 4.15, the LW feed is well impedance matched, with the reflection coefficient Γ below -15dB for the entire frequency band.

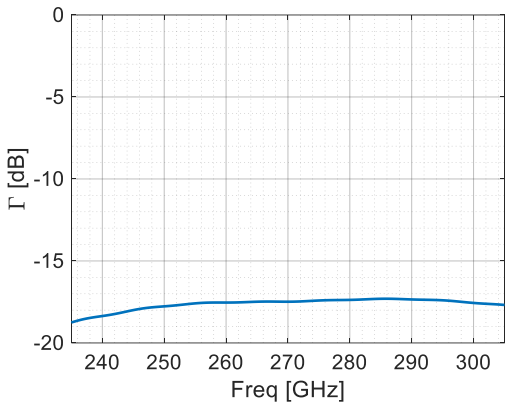

Figure 4.15 The reflection coefficient of the feed

4.3.3.2 Radiation Efficiency

We need to calculate the radiation efficiency of the lens antenna according to eq. 2.9. To find this efficiency, we will simulate the individual lens antenna from Section 4.3.2 in CST, and the view in CST is shown in Figure 4.5. The simulation is performed in a time domain solver. The background material is filled with vacuum, and the boundary conditions at the x, y, and z direction are all set as open (add space). To avoid the impact of the reflections, the simulation terminates when $t = 0.12ns$. The frequency band is limited in $f \in [235GHz, 305GHz]$. Same as the simulation of the feeding structure, the waveguide port is located one wavelength below the feed (in the waveguide). The input power is set to be $P_{in} = 0.5W$.

We will export the field distribution on the aperture plane from CST to calculate the radiated power by integrating the Poynting vector on the aperture plane as eq. 2.34. The side view of the simulation and the power distribution on GO aperture at 270 GHz are shown in Figure 4.16.

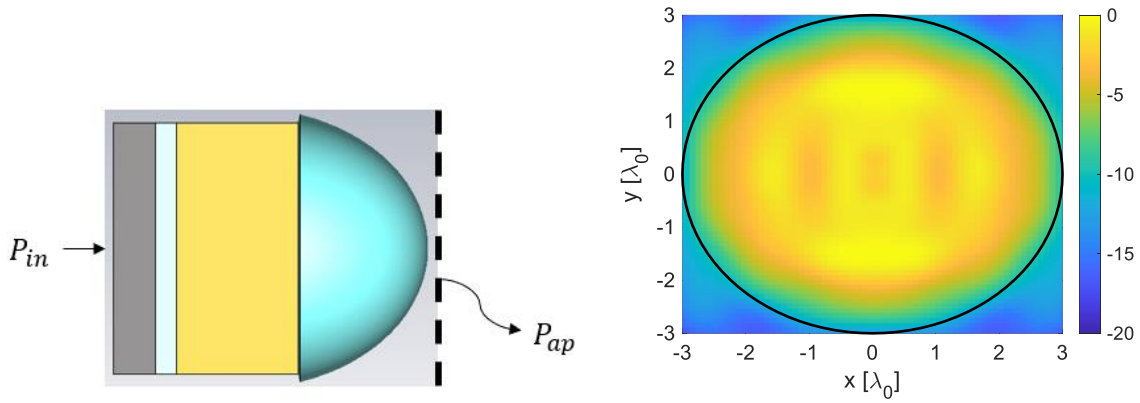

(a) *(b)*

Figure 4.16 The (a) side view in CST and the (b) GO current distribution on aperture at 270 GHz

From Figure 4.16, the power distribute in the aperture circle, and looks uniform with ripples because still some reflections remain . With these simulations, applying eq. 2.9 at each frequency, the radiation efficiency of the lens antenna at each frequency is shown in Figure 4.17.

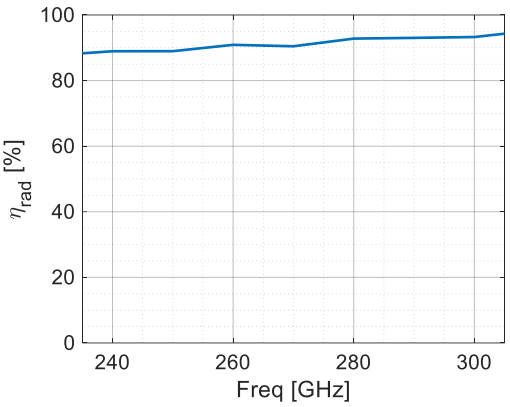

Figure 4.17 The radiation efficiency of the lens antenna to approximate the uniform current distribution

From Figure 4.17, the radiation efficiency is around 90% over frequency. This efficiency will be used in Chapter 5 to compare the channel matrix results and the CST simulation results.

4.3.3.3 Far Field Pattern and Radiated Field in the Near Field Range

We can have the far field pattern and field distribution in the near field from this simulation with a far field monitor and a field monitor at each frequency. We show an example of the far field pattern and the radiated field on a plane on top of the lens antenna with a near field distance $d = 10\lambda_0$ at 270GHz in Figure 4.18.

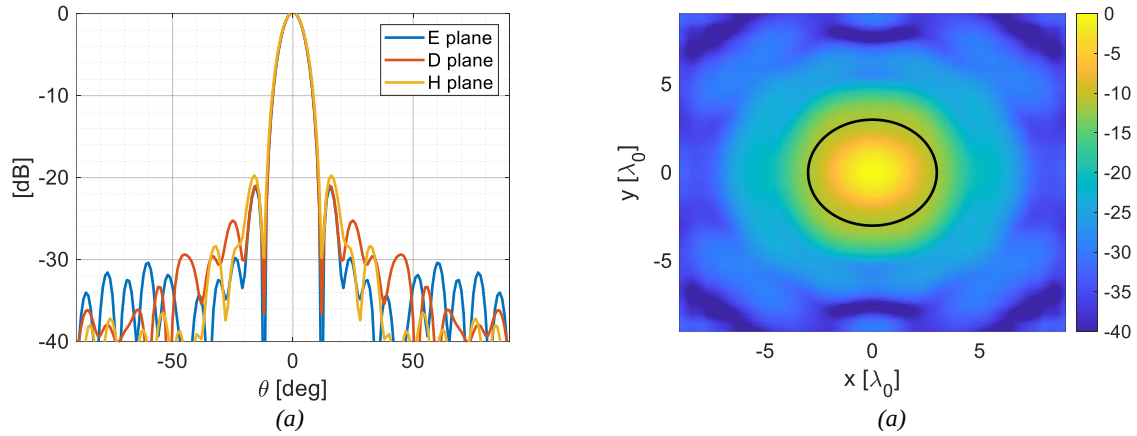

Figure 4.18 The (a) far field pattern and the (b) field distribution on a plane on top of the lens aperture with distance of $d = 10\lambda_0$ (the black circle refers to the position of the aperture) at 270 GHz

Comparing Figure 4.18(a) with Figure 4.8, Figure 4.18(a) consists more side lobe when $\theta > 50°$. This is because of the effect of the primary wave that spills out of the lens cap and radiates to the far field. The Near field results in Figure 4.18(b) are less continuous than in Figure 4.9, and this is because Figure 4.18(b) has the effect of reflections even if we truncate the time to simulate.

4.4 Lens Antenna for Optimized Current Distribution

In this section we will synthesize the optimized current with lens antenna. The design of this lens will be discussed in Section 4.4.1, the performance of this lens will be shown in Section 4.4.2 and then the CST results will be presented in Section 4.4.3.

4.4.1 Design Process and Final Parameters

The optimized current distribution of our scenario requires a -16dB Gaussian taper and a phase focus at $10\lambda_0$. As introduced in Section 4.2.2, we will implement a lens antenna to approximate the amplitude distribution and then put a hyperbolic lens antenna to approximate the phase focusing.

4.4.1.1 Elliptical Lens Antenna Design

As introduced in 4.1, we will design the LW elliptical lens antenna with the double-slot iris feed. Since the current distribution of the slots can be analytically defined as described in eq. 4.1, the primary fields radiated by the feed inside the lens can be calculated with spectral domain methods, and the GO currents on top of the lens are then calculated efficiently with in-house GO tool in MATLAB [27]. This process is full-analytical, as shown in Section 4.2.2.

The design of the elliptical lens antenna starts from the uniform LW elliptical lens antenna design of [22]. The design is shown in Figure 4.19. In particular, the material of the lens is high density polyethylene (HDPE) with relative permittivity $\epsilon_r = 2.3$, the geometrical values of the feeds are set to $\alpha = 65.5°$, $\rho_0 = 0.54\lambda_0$, $w = 0.3\lambda_0$, the thickness of the air cavity $h_a = 0.56\lambda_0$, where all these parameters and the feed geometry are shown in Figure 4.2, and the diameter of the lens $D_l = 28\lambda_0$, the truncation angle $\theta_{max} = 40°$. Since our frequency band and diameter of the lens are different from the frequency band of that paper [reference], all the dimensions of the design have been scaled to fit our frequency band, $f \in [235,305]GHz$ and the diameter of the lens is set to $D_l = 6\lambda_0$.

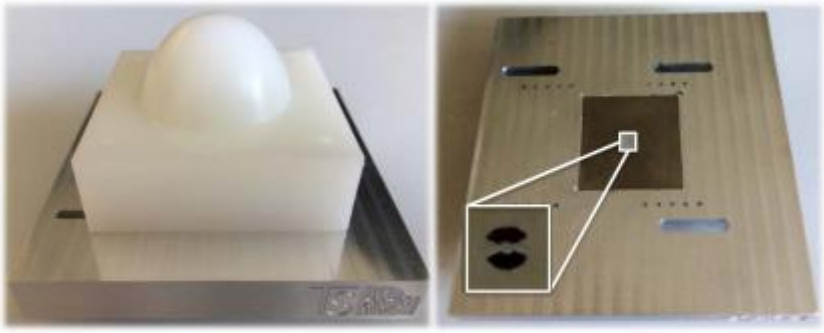

Figure 4.19 The design of [22]

The GO currents of [22] in our frequency is shown in Figure 4.20.

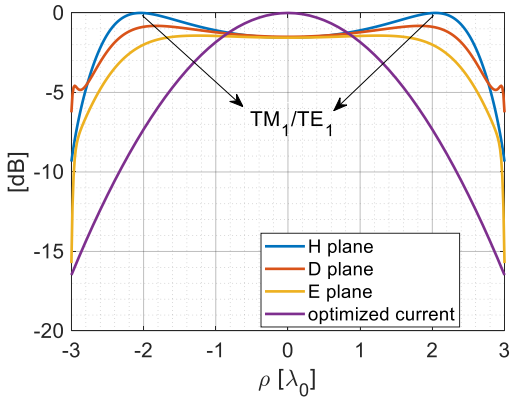

Figure 4.20 The amplitude of the GO current of [22] in our scale and the amplitude of the optimized current distribution

From Figure 4.20, there are two main differences between the GO current and the -16 dB Gaussian current. Firstly, the edge taper level of the GO current is -10 dB, -5dB, and -10dB respectively in the H, D, and E plane, which is less than our taper requirements; also the distribution does not shape as Gaussian beam, which is because of the peaks of TM_1/TE_1 modes.

Let us focus on the taper level first. The primary field inside of the lens based on the design of [22] is shown in Figure 4.21 (a), and the primary fields with $\varepsilon_r = 11.9$ is shown in Figure 4.21 (b).

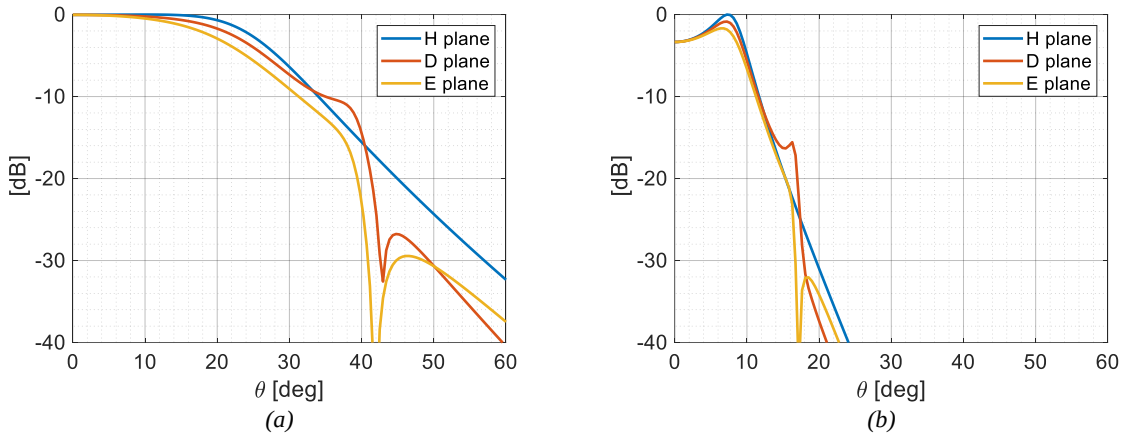

Figure 4.21 The GO currents of lens antenna with (a) $\epsilon_r = 2.3$ and (b) $\epsilon_r = 11.9$ in the H, D, and E plane

From Figure 4.21, the amplitudes of both primary fields decrease with θ. This means that we need to have a wider truncation angle θ_{max} to reach more amplitude taper. The directivity of a LW feed depends on the contrast between the air cavity and the lens material. Therefore, we can find a material with higher ϵ_r that provides more amplitude taper on the lens aperture. From Figure 4.21, one can understand that it is possible to increase the taper level by changing the truncation angle with an increasing the ϵ_r. The truncation angle is shown in Figure 4.1.

We also need to shape the peaks of TM_1/TE_1 modes from Figure 4.20. The direction of the TM_1/TE_1 modes over different thickness of the air cavity, shown in Figure 4.22. From Figure 4.22, the y-axis is the propagation angle of the LW modes, and we can find that this direction changes with the thickness of the air cavity. In principle, if we can find a proper thickness of the air cavity, we can shape the GO current to gaussian distribution. Figure 4.23 shows an example of the GO current if we adjust the air cavity $h_a = 0.4\lambda_0$ and keep other parameters the same as in [22]. Comparing with Figure 4.20 of the original design, Figure 4.23 shapes more like Gaussian beam.

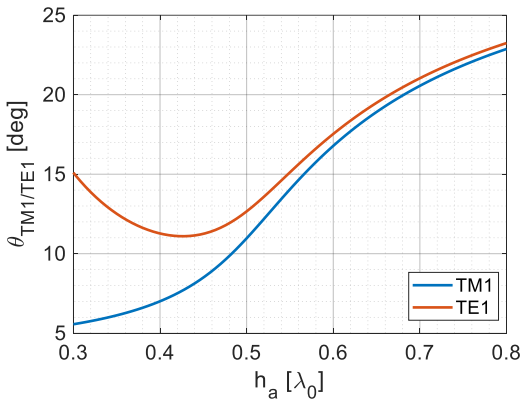

Figure 4.22 The propagation angle of TM_1/TE_1 over thickness of the air cavity

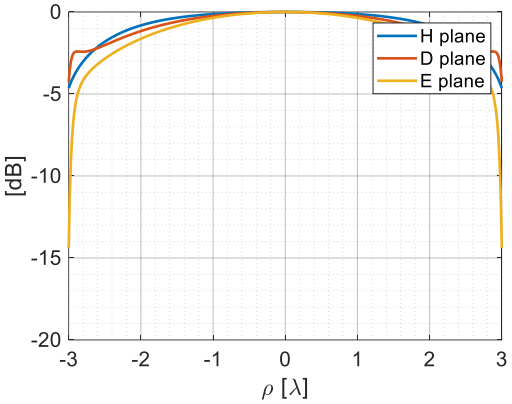

Figure 4.23 The GO current of the lens antenna with $h_a = 0.4\lambda_0$ in the H, D and E plane

It is also essential to find the correct phase center Δz. The phase center is shown in Figure 4.1, located below the ground plane of the LW feed. As introduced above, we are using the elliptical lens antenna to approximate the amplitude of the optimized current distribution. This means that the phase distribution of the GO current should be as constant as possible. We will find the phase center according to multiple simulations with different Δz to find the optimal one that will provide the most constant phase distribution.

Now we understand that we can increase the taper level by increasing the truncation angle θ_{max} or increasing the ϵ_r; we can shape the primary field more Gaussian by adjusting the thickness of the air cavity h_a; and we can adjust the phase center Δz to have the most constant phase distribution. We will use these three approaches to find the optimal parameters that will provide matched GO current. After multiple simulations in MATLAB, considering the agreements of GO current distribution to -16dB Gaussian distribution and the impedance matching, the parameters are chosen as material permittivity $\epsilon_r = 4$, $\alpha = 65.5°$, $\rho_0 = 0.54\lambda_0$, $w = 0.3\lambda_0$, the air cavity $h_a = 0.45\lambda_0$, the phase center $\Delta z = -0.8mm$, the diameter of the lens $D_l = 6\lambda_0$ and the truncation angle $\theta_{max} = 35°$. Where α, ρ_0, w and wg are the geometry parameters of the double-slots iris feed, we keep it the same as the original design; and the ϵ_r, θ_{max}, h_a, Δz are adjusted.

Same as 4.3.1, we also add a ML on top of the elliptical lens antenna to increase the reflection efficiency η_{ref} of the lens, and this will also decrease the impact of the reflections. For the matching layer, its relative permittivity $\epsilon_{rm} = 2$ and thickness $h_m = \frac{\lambda_m}{4}$, where λ_m is the wavelength in the ML material. Since we are not going to fabricate, we did not consider whether the chosen material for the elliptical lens and its ML exist in the real world.

The distribution of the GO current illuminated by this antenna and its performance will be described in Section 4.4.2.

4.4.1.2 Hyperbolic Lens Antenna Design

The geometry of the hyperbolic lens antenna is detail described in [28]. It contains one side of the planar surface and the other side of the hyperbolic surface, and these dielectric lenses can focalize the planar incident fields without any aberration at the focus of the hyperbolic surface. A schematic of the hyperbolic lens is shown in Figure 4.24.

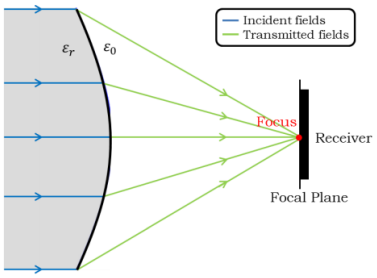

Figure 4.24 The schematic of the hyperbolic lens antenna [28]

From Figure 4.24, the incident waves are focalized at the focus of the hyperbolic lens, where the focus of the hyperbolic lens is defined by the curvature and the material of the lens. The focalization property of the hyperbolic lens only dependent on the relative permittivity of the hyperbolic lens material ϵ_{rh} and the hyperbolic curve. From [28], the curve of the hyperbolic lens is analytically defined by ϵ_{rh} and the focal distance F, and the hyperbolic lens antenna performs constant with different frequency. This allowing us to easily define the hyperbolic lens. Finally, the diameter of the hyperbolic lens is $D_h = 6\lambda$, the focal distance $F = 10\lambda_0$, and the relative permittivity of the lens $\epsilon_{rh} = 2.5$. To reduce the impact of reflections in communication, MLs are added to both side of the hyperbolic lens, with relative permittivity $\epsilon_{rm} = 1.58$ and thickness $h_m = \frac{\lambda_m}{4}$, where λ_m is the wavelength in the ML material. Since we are not going to fabricate this design, we did not consider whether the chose material for the hyperbolic lens and its ML exist in the real world.

Finally, the hyperbolic lens antenna is located on top of the elliptical lens antenna, with distance of one free space wavelength, a view of this antenna system in the CST model is shown in Figure 4.25. This lens antenna will be called as the Gaussian focused lens antenna in the rest of this thesis.

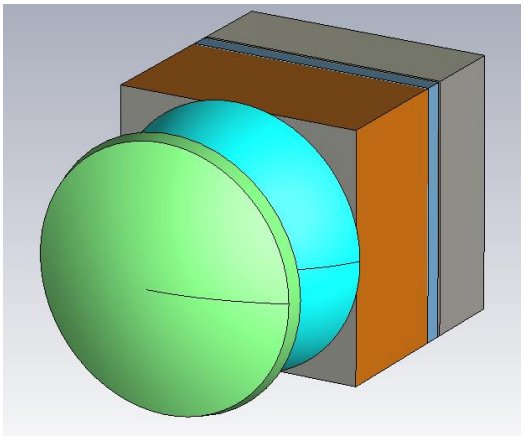

Figure 4.25 The view of the Gaussian focused lens antenna in CST

4.4.2 GO Aperture Performance

Here we will evaluate the GO current distribution of this antenna and calculate the far field, and near field radiated by this GO current, finally we will show the channel matrix. All these simulations take place in MATLAB, as introduced in Section 4.2.2. The primary field and GO current simulations are analytically performed in MATLAB.

4.4.2.1 Performance at 270 GHz

The amplitude and phase of the GO current at 270GHz in the H, D, and E plane are shown in Figure 4.26.

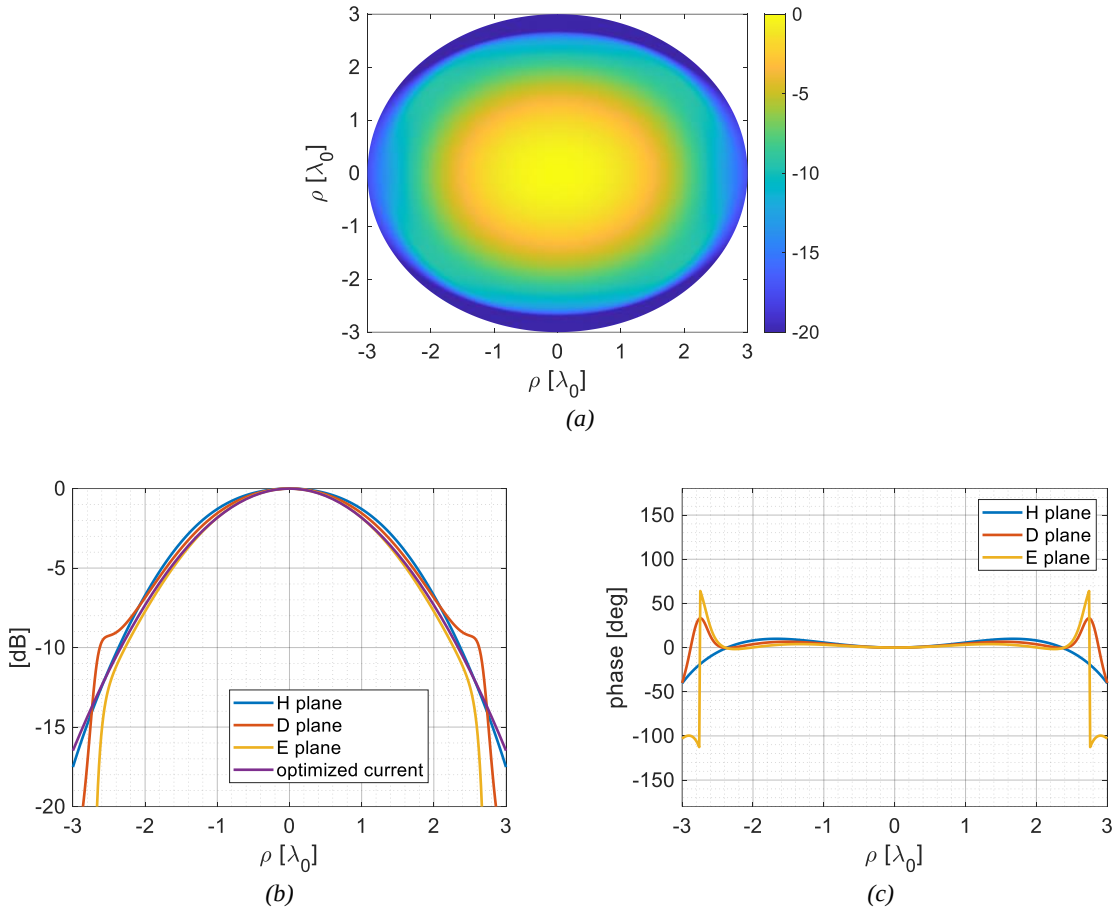

Figure 4.26 The amplitude (a) in 2-D, (b) in 1-D and the (c) phase of the GO current at 270GHz

From Figure 4.26(b), the amplitude distribution of the GO field in H plane is well matched with the amplitude of the ideal current in H plane, and the errors in D and E plane are acceptable since the TM_0 LW mode (the peak in D plane at $\rho = 2.5\lambda_0$) is well suppressed. However, looking at Figure 4.26(c), the phase error is significant (around 40°). This is already the best phase error we can find after multiple simulations with amplitude distribution constant. The way to find have the best phase error is by multiple simulations with different phase center Δz.

Same as Section 4.2.2 for the uniform lens antenna, we are going to compare the difference between the field radiated by the GO currents at 270GHz and the optimized current to the free space in the far field at $r = 1m$ and on a plane in the near field at $d = 10\lambda_0$. These results are shown in Figure 4.27 and Figure 4.28 respectively. As introduced in 4.2.2, Since the elliptical lens antenna only approximates the amplitude distribution, to fairly compare, the phase term of the ideal current distribution $e^{-\frac{jk_0|\vec{\rho}'|^2}{2\cdot 10\lambda_0}}$ is manually multiplied, and the focused GO current calculated as eq. 4.7 is used to calculate the fields.

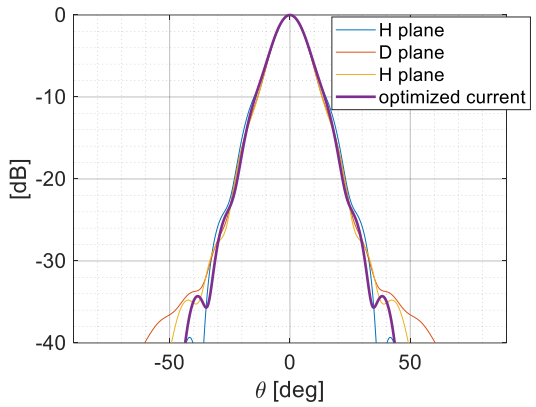

Figure 4.27 The far field pattern radiated the focused GO current at 270GHz in the H, D and H plane, and the far field radiated by the ideal current at 270GHz

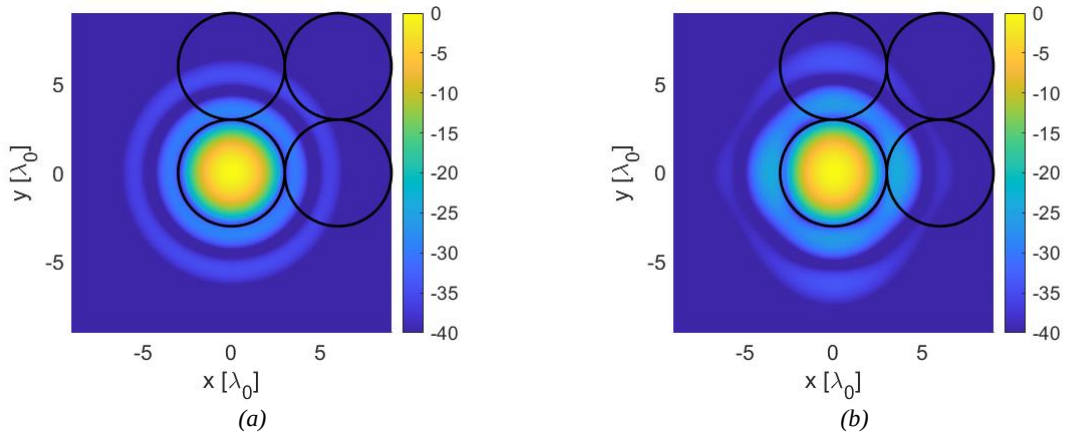

Figure 4.28 The field radiated by the (a) ideal current and (b) focused GO current at 270GHz on 2-D plane with distance of $10\lambda_0$

Since the optimized current is symmetric in H, D and E plane, the far field of only the H plane is shown. From Figure 4.27, the far field patterns of the focused GO current are almost symmetric in the E, D, and H planes, with only the main beam and with almost zero side lobes. For the main beams of these two currents, their beam width is barely different. From Figure 4.28, the field radiated by the optimized current and the one radiated by the focused GO currents are similar on the plane with a near field distance to the aperture, with low side lobe levels on both figures. Figure 4.27 and Figure 4.28 shows that the radiation effects of the ideal current and focused GO current are similar, and the difference is negligible.

Next, we will calculate the channel matrix according to eq. 2.40. Since Figure 4.26 shows a significant error in phase at 270 GHz, we must first calculate the channel matrixes of optimized current and focused GO current at 270 GHz. Besides these two channel matrixes, to study the impact of the phase, we also include the channel matrix of the focused GO current with the correct phase. The focused GO currents with the correct phase are calculated as the product of the absolute value of the GO current of the elliptical lens antenna and the phase term:

$$f_{GO}^{correct\ phase} = \left|f_{GO}^{ell}\right| e^{-\frac{jk_0\left|\vec{\rho}'\right|^2}{2\cdot 10\lambda_0}} \qquad [4.9]$$

Where f_{GO}^{ell} is the GO current of the elliptical lens antenna.

These channel matrices of three different currents are shown in Figure 4.29.

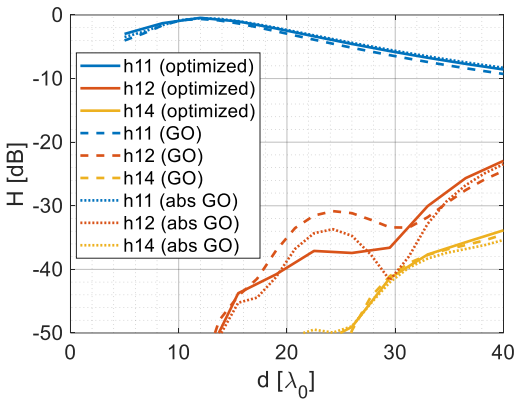

Figure 4.29 The channel matrices of optimized current (solid lines), focused GO current (dash lines) and focused GO current with corrected phase (dot lines) at 270GHz

From Figure 4.29, the couplings h_{11} are the same for three currents, but the interferences h_{12} and h_{14} are different. The difference between the interferences of the optimized current and focused GO current with correct phase are acceptable, which means that the amplitude of the optimized current is well approximated; the difference between the interferences of the focused GO current and the ones of the optimized current is around 8dB in h_{12} when $d \in [20\lambda_0, 30\lambda_0]$, and this is caused by the phase error.

4.4.2.2 Frequency Dependence

Same as Section 4.3.2.2, since the channel matrix is frequency-dependent on the current distribution at each frequency, and the GO current changes over frequency, to study the frequency-dependence of the channel matrix, we need to study the frequency-dependence of the GO currents first. The GO currents at 240GHz and at 300GHz are shown in Figure 4.30 and Figure 4.31 respectively.

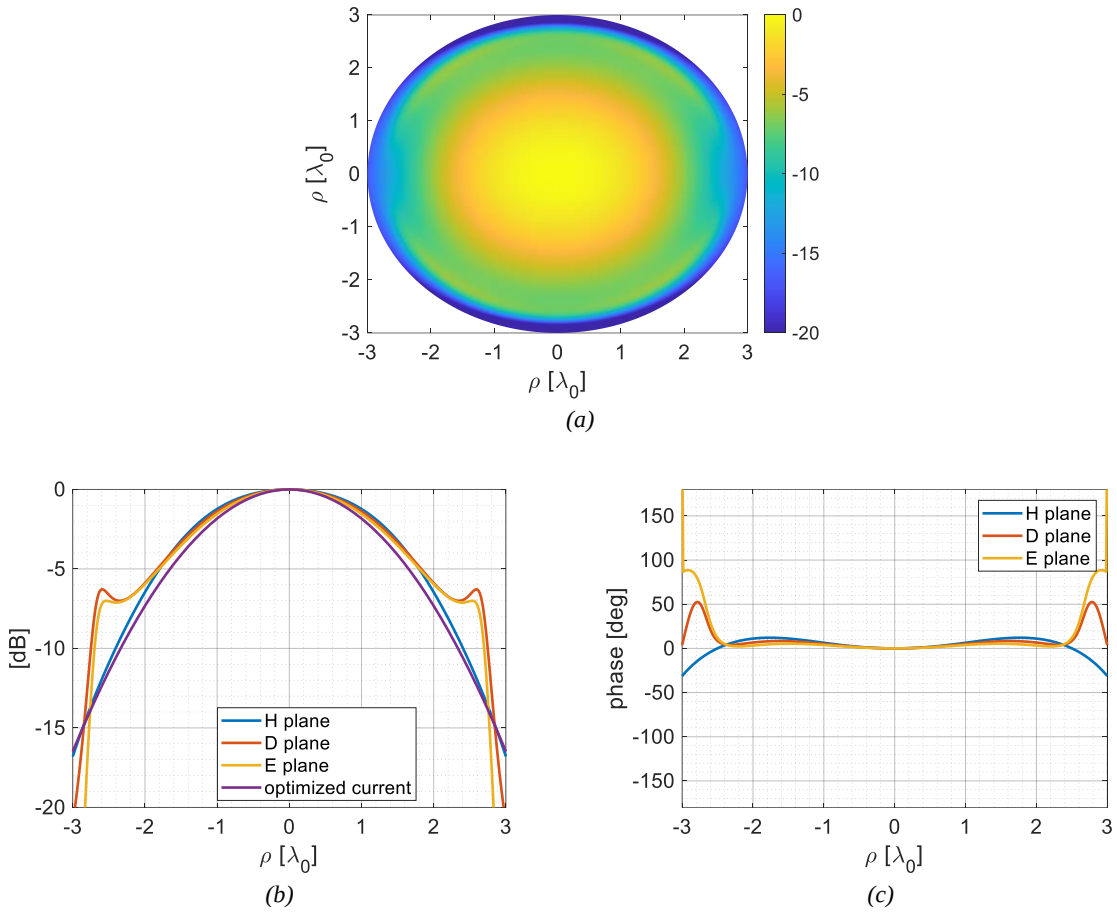

Figure 4.30 The amplitude (a) in 2-D, (b) in 1-D and the (c) phase of the GO current at 240GHz

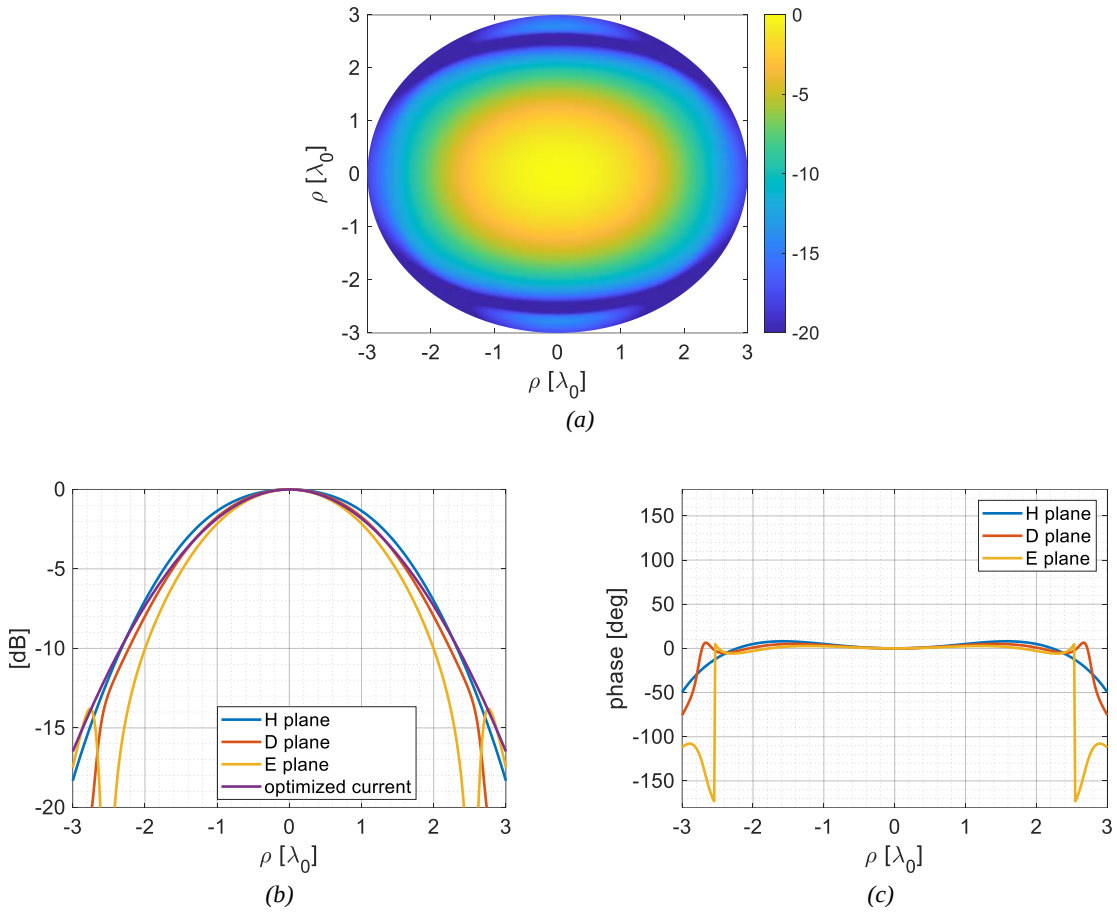

Figure 4.31 The amplitude (a) in 2-D, (b) in 1-D and the (c) phase of the GO current at 240GHz

From Figure 4.30 and Figure 4.31, unlike the GO currents at 270GHz, we find a significant change in amplitude distribution for GO currents in both 240GHz and 300GHz. It is hard to quantify the effect of these changes on the channel matrix only based on the distribution, so we will then calculate the channel matrix over frequency with the GO currents at each frequency to evaluate the effect of the change on currents distribution, shown in Figure 4.32. Since the hyperbolic lens antenna is frequency independent, as introduced in 4.2.2, we can still use eq. 4.7 to calculate the focused GO current, and the GO current of the elliptical lens antenna f_{GO}^{ell} should change over frequencies as Figure 4.26, Figure 4.30 and Figure 4.31. The optimized current distribution is unchanged over frequency to calculate the channel matrix over frequency, always with -16dB amplitude Gaussian taper and focusing at $d = 10\lambda_0$.

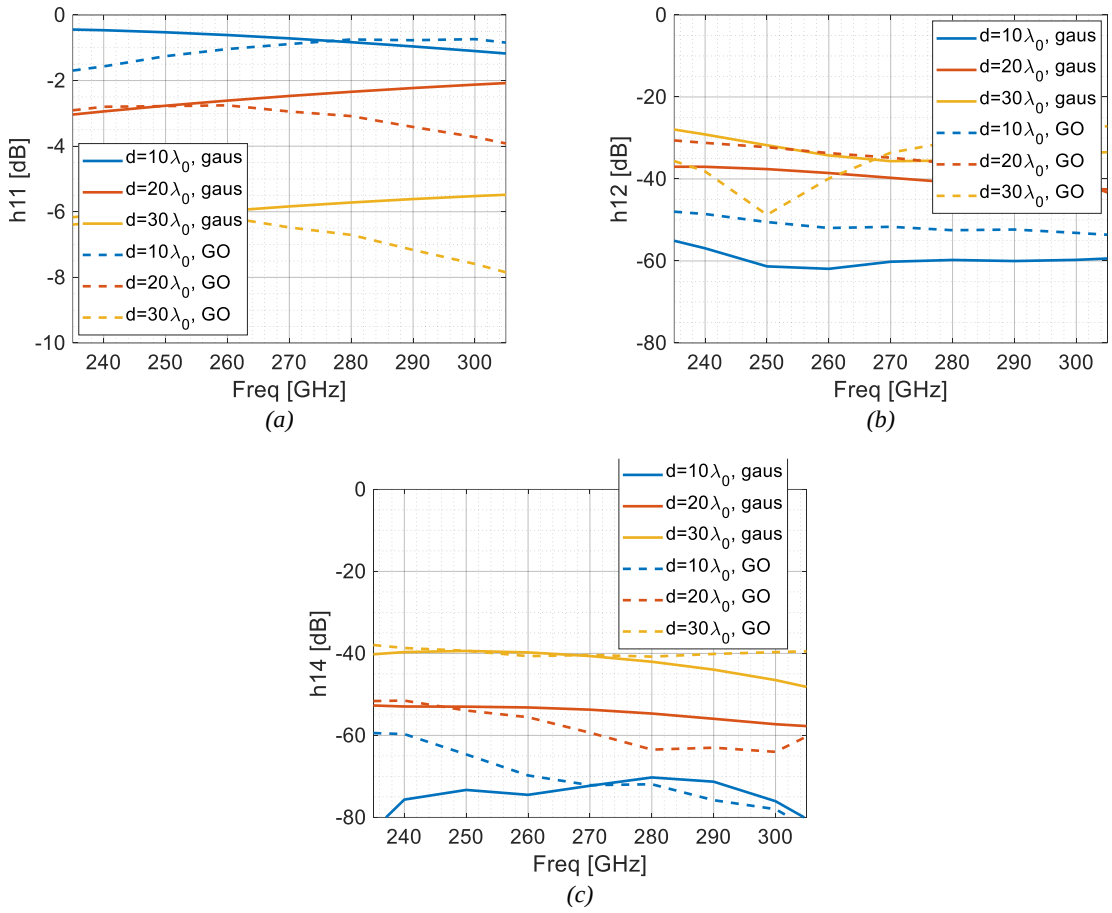

Figure 4.32 The (a) h_{11}, (b) h_{12} and (c) h_{14} of uniform current distribution (solid lines) and of GO current (dash lines) over three link distances

The agreements are not good. We already saw this difference in Figure 4.29, the channel matrix of the GO currents at 270GHz, and from Figure 4.29, the differences between the interference of the GO currents and the optimized currents are around 10dB. Which is similar with the results over frequency in Figure 4.32. Figure 4.29 and Figure 4.32 tell us that the difference is because of the phase error, not the frequency dependence.

To verify that the differences are not from the frequency dependence, we will calculate the spectrally average channel matrix to evaluate the frequency dependence of the antenna. The spectrally average channel matrix is to take the average channel matrix over frequency from Figure 4.32, and then plot over distance. The spectrally average channel matrix is shown in Figure 4.33.

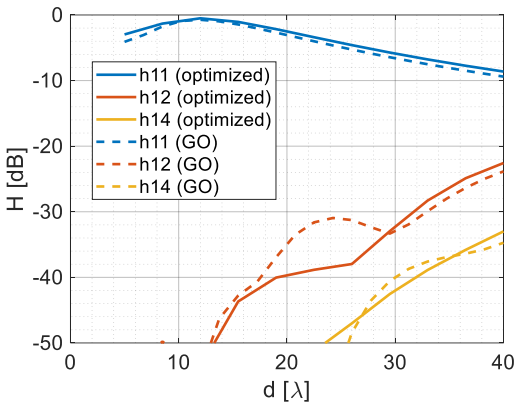

Figure 4.33 The spectrally average channel matrix of optimized current distribution (solid lines) and GO currents (dash lines)

From Figure 4.33, there is a significant increase in h_{12} when applying focused GO current in link distance range $d \in [15\lambda_0, 30\lambda_0]$, and we already knew that this is because of the phase error. In Figure 4.33, the error in interferences is similar with the error in Figure 4.29, furtherly prove that the main contributor of the error is the phase error. Predictably, this increase in interference will decrease the capacity.

4.4.3 CST Simulation for Individual Lens Antenna

Same as Section 4.3.3, we are going to study the results from CST simulation.

4.4.3.1 Reflection Coefficient

The simulation of the reflection coefficient of this LW feed is performed in a time domain solver in CST, shown in Figure 4.34. The background material is filled with dielectric ($\epsilon_r = 4$), and the boundary conditions at the x, y, and z direction are all set as open. The frequency band is limited in $f \in [235GHz, 305GHz]$. The waveguide port is located one wavelength below the feed (in the waveguide shown in Figure 4.36). From the simulation, we can have the S_{11} of the port, where this S_{11} is equivalent to the reflection efficiency Γ, shown in Figure 4.37. From Figure 4.37, the LW feed is impedance matched, with a reflection coefficient Γ below -10dB for the entire frequency band.

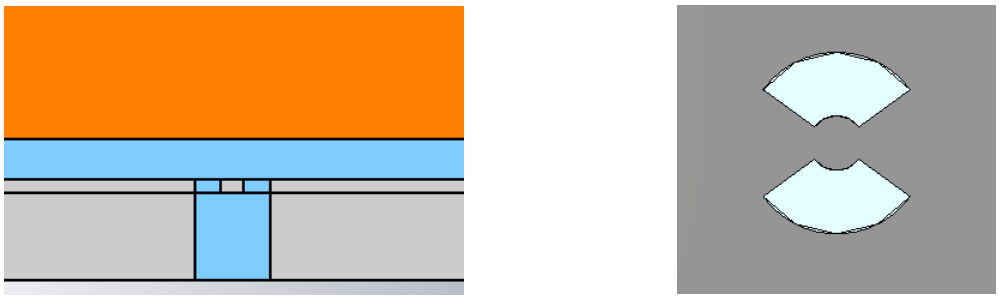

(a) *(b)*

Figure 4.34 The CST simulation of the feed in (a) side view and (b) top view

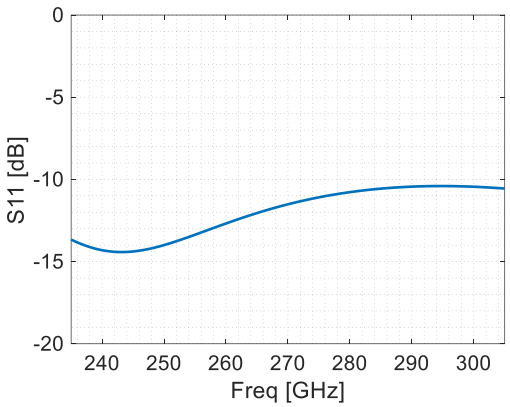

Figure 4.35 The reflection coefficient of the feed

4.4.3.2 Radiation Efficiency

Same as Section 4.3.3.2, we can have the radiation efficiency of this antenna by eq. 2.9. The simulation is performed in the time domain solver, and the simulation duration is truncated as $t = 0.16ns$ to avoid the influence from the reflections. The background material is a vacuum and the boundary conditions are open (add space) in the x, y, and z directions. The frequency band is limited in $f \in [235GHz, 305GHz]$. Same as the simulation of the feeding structure, the waveguide port is located one wavelength below the feed (in the waveguide). The input power is set to be $P_{in} = 0.5W$.

We export the field distribution on the aperture plane from CST to calculate the radiated power. The side view of the simulation and the power distribution at 270 GHz are shown in Figure 4.36.

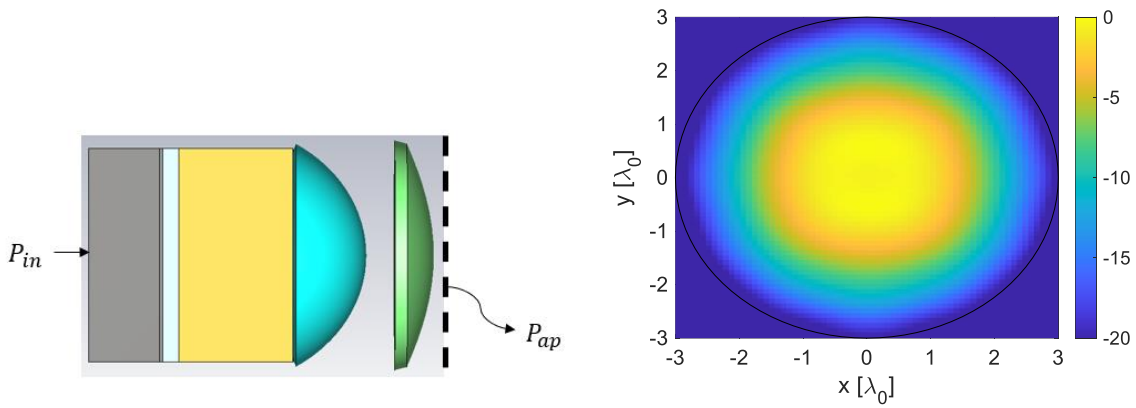

Figure 4.36 The (a) side view in CST and the (b) GO current distribution on aperture at 270 GHz

From Figure 4.36(b), the power distribution in the aperture circle shapes Gaussian. With these simulations, the radiation efficiency of the lens antenna at each frequency is calculated with eq. 2.9, shown in Figure 4.37.

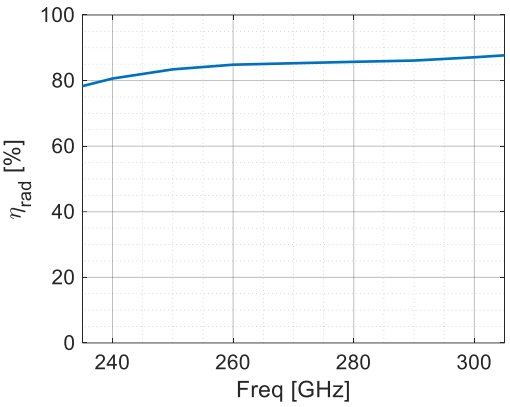

Figure 4.37 The radiation efficiency of the lens antenna

From Figure 4.37, the radiation efficiency is around 85% over frequency. This efficiency will be used in Chapter 5 to compare the channel matrix results and the CST simulation results.

4.4.3.3 Far Field Pattern and Radiated Field in Near Field Range

We can have the far field pattern and field distribution in the near field from this simulation with far-field monitor and field monitor at each frequency. We show an example of the far field pattern at 270GHz in Figure 4.38(a), and the radiated field on a plane on top of the lens antenna with a near field distance $d = 10\lambda_0$ at 270 GHz in Figure 4.38(b).

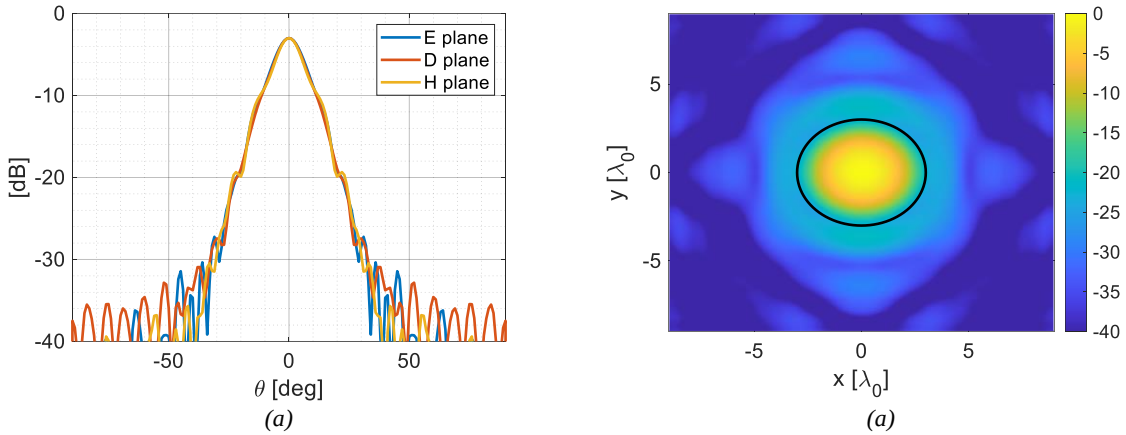

Figure 4.38 The (a) far field pattern and the (b) field distribution on a plane on top of the lens aperture with distance of $d = 10\lambda_0$ (the black circle refers to the position of the aperture) at 270 GHz

Figure 4.38(a) also shows more side lobe than Figure 4.27 when $\theta > 50°$, but this side lobe has less magnitude than the ones in Figure 4.18(a) in Section 4.3.3.3. This is because that to provide -16 dB taper GO currents, the primary waves spill out to the lens cap is weak The Near field results in Figure 4.38(b) also shows less continuous because of reflections.

4.5 Capacity Estimation with GO Currents

Since the goal of this thesis is to find the maximum capacity of the MIMO communication system, we are going to estimate the capacity using the derived focused GO current before performing the full-wave simulations in the next chapter. We will calculate capacities: capacity of uniform current, capacity

of optimized current, and capacity of the focused GO current to approximate optimized current. This will show the validity of the antenna design and the advantage of the proposed optimized current.

Applying all the parameters introduced in Chapter 2 (e.g. input power, noise level, etc) and the channel matrices, the capacities of the optimized current, the focused GO current and the uniform current are shown in Figure 4.39.

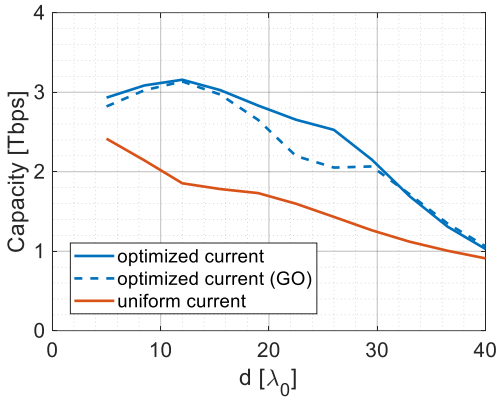

Figure 4.39 The capacities of optimized current (blue solid line), focused GO current of Gaussian focused lens antenna (blue dash line), and uniform current (red solid line) over distance

From Figure 4.39, both optimized current and focused GO current can provide channel capacity more than 3Tbps/s in short distance $d < 15\lambda_0$. In the distance range $d \in [15\lambda_0, 30\lambda_0]$, the focused GO current performs worse than the optimized current, where this error is due to the phase error. But they are both better than the uniform current distribution.

To sum up, in this chapter we successfully designed the lens antenna to synthesize the optimized current distribution with acceptable error on the channel matrix (basically from the phase error). We also find a good antenna to synthesize the uniform current distribution, and then scale it to our frequency and diameter. The comparison in channel matrix and the capacity is well matched, which give us enough confidence to use the Gaussian focused lens antenna for the later full-wave (FW) simulation in CST.

5 FW Simulations of MIMO Lens Arrays in CST

In Chapter 4, we proposed an antenna system consisting of an elliptical lens antenna and a hyperbolic lens antenna, called as Gaussian focused lens antenna, to synthesize the optimized current distribution and studied its behavior in CST. To compare the CST results to those of the MATLAB model, the channel matrix and capacity are evaluated using the GO analysis, also described in Chapter 4. The results of the channel matrix and capacity of GO current are in reasonable agreement with the ones of optimized current. In this chapter, we will study the full-wave (FW) simulations in CST of 2×2 array of Gaussian focused lens antenna, using an array of uniform antenna as a reference, and then compare the results from the CST and the channel matrix of GO current.

To compare the channel matrix based on the GO current with the S-parameters from the FW CST simulations in a fair manner, we need to follow some post-processing steps. These are explained for a SISO system for simplicity, in 5.1. We will then study the FW CST simulations and the results we have from CST for arrays of both the Gaussian focused lens antenna and the uniform lens antenna in 5.2. After, we will validate the channel matrix and the S-parameters in 5.3.

5.1 FW Simulation for SISO and Data Processing

To compare the channel matrix from MATLAB with the S-parameters from CST, we need to follow two data-processing steps. To explain these in a simple way we will use an example of the uniform lens in a SISO system. These data processing techniques, however, are general and can be applied to MIMO scenarios as well with both uniform lens antenna and the Gaussian focused lens antenna.

The SISO scenario which we will use to explain the post-processing steps is shown in Figure 5.1. The Tx and Rx antennas are perfectly aligned and face each other. The antennas are uniform lens antenna, as described in Section 4.3, have a diameter of $D_l = 6\lambda_0$ and are separated by a link distance d. The link distance d is measured from the tops of the lenses which correspond to the location of the apertures, indicated with dashed lines in Figure 5.1, which are used in the MATLAB model.

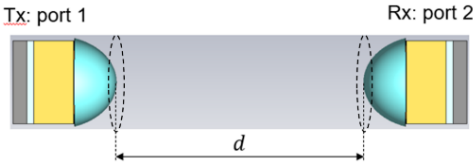

Figure 5.1 Simulation environment of a SISO link consisting of two uniform lens antennas of diameter $D_l = 6\lambda_0$ and separated by a link distance d.

To validate the channel matrix in the interested range, the SISO system with three distances in the interested range $d = 10\lambda_0, 20\lambda_0 \; and \; 30\lambda_0$ is simulated. As the h_{11} only describes the transfer of the signal from the Tx to the Rx antenna, we are interested in comparing this to the S_{21} of a FW CST simulation. The results of the FW CST simulation for the scenario of Figure 5.1 are shown in Figure 5.2 over a frequency band of 235 GHz to 305 GHz. The h_{11} of the GO current of this uniform lens antenna is also shown in Figure 5.2.

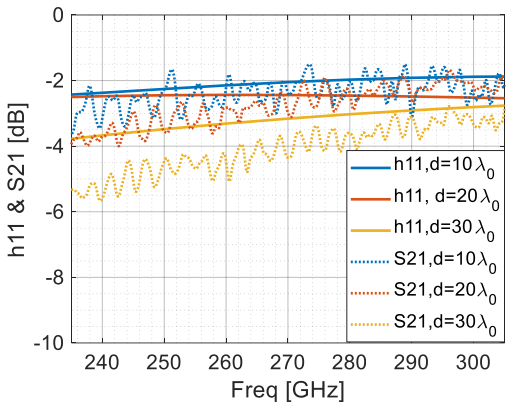

Figure 5.2 The coupling h_{11} of the channel matrix (solid lines) and the S_{21} of a FW CST simulation (dash lines) over frequency for the scenario shown in Figure 3.7.

From the results in Figure 5.2, it is evident that we cannot easily compare the two results. There are two reasons for this: the first is that the S_{21} of CST has a lot of oscillations on the signal and the second is that the h_{11} is higher than the average of the S_{21}. The oscillations on the S_{21} are due to reflections. The MATLAB model does not take these into account which means that to be able to compare the two results, the CST simulation must be time-gated to remove as many reflections as possible. The reason that the power transfer of the MATLAB model seems to be higher than the average of the CST results is due to the assumption made on the available power. In the MATLAB model, we assume that all the power is available directly at the aperture. In contrast, in CST some of the input power will be reflected from the Tx port, and due to spillover loss and reflection loss, not all power will arrive at the location of the aperture. This mismatch in power levels must be corrected. These two steps will be explained in further detail in the following sections.

5.1.1 Time Gating of CST Results

As mentioned previously, to remove the oscillations of S_{21} in Figure 5.2, we can time-gate (TG) the CST simulations. Time gating is a function that can be applied to remove unwanted responses in the time domain. Therefore, one must first study the time domain of the S_{21} shown in Figure 5.2. We show an example of the time domain of S_{21} with distance $d = 10\lambda_0$ in Figure 5.3(a). In this figure, the blue signal corresponds to the input signal of the Tx port in the simulation and the red peaks correspond to the energy received by the Rx port over time. The different peaks correspond to LoS signal and reflections from different origins. They appear at different times because the LoS signal and the reflected signals have different light paths. With the speed of light in the free space c_0, the time needed for the EM wave to propagate through a certain distance d in the material with relative permittivity ϵ_r is calculated as:

$$t = \frac{d}{\frac{c_0}{\sqrt{\epsilon_r}}} \qquad [5.1]$$

With eq. 5.1, the light path for each pulse on Figure 5.3(a) is calculated and the origin of the peaks can be determined. The origins of these signals are explained in the figure on the right of Figure 5.3(b). The LoS signal has the shortest light path, being the first pulse on the received signal, and the reflection signals all come later. We will filter out the reflected signals and only keep the LoS signal.

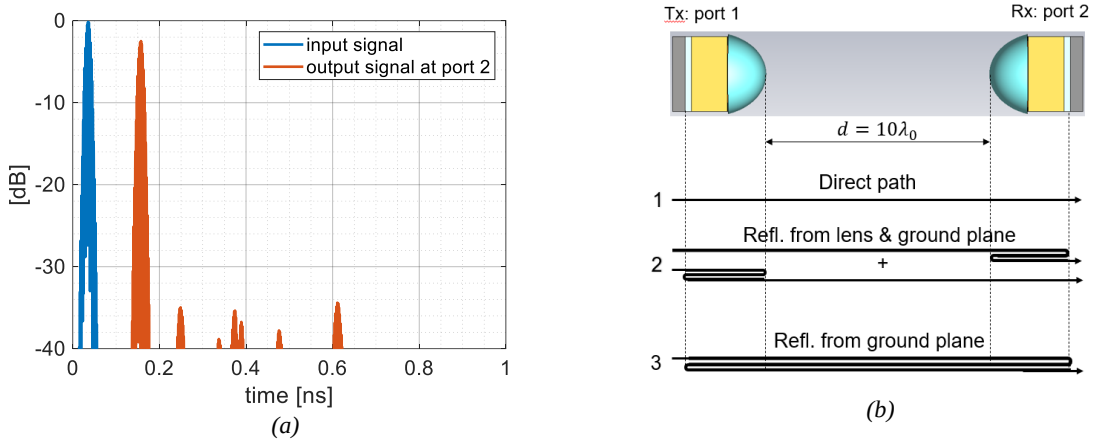

Figure 5.3 The (a) time domain signal and (b) light path for SISO simulation with distance $d = 10\lambda_0$

This information is used to see how large the time-gate window will be. To time-gate a signal, one must choose a specific time t_0 for which the TG function has the following values:

$$f_{TG}(t) = \begin{cases} 1, t < t_0 \\ 0, t > t_0 \end{cases} \quad [5.2]$$

A logical choice, to remove the reflections in the S_{21} is to choose a after the first received pulse (the LoS pulse). The time-domain S_{21} signal is then multiplied by this window:

$$S_{21}^{time\ domain,TG}(t) = S_{21}^{time\ domain}(t) f_{TG}(t) \quad [5.3]$$

For example, in Figure 5.3(a), the time-gating time $t = 0.2ns$. Now we have the time domain S parameter $S_{21}^{time\ domain}$ containing only the LoS signal. We will then apply the Faster Fourier Transform (FFT) to transform $S_{21}^{time\ domain}$ back to the frequency domain.

Figure 5.4 shows the S_{21} before and after TG. It is evident that after the TG the ripple has disappeared. The S_{21}^{TG} is now more or less the average of the S_{21} before TG.

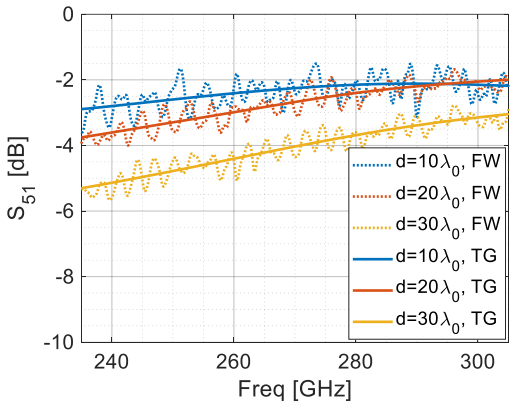

Figure 5.4 The S_{21} of the SISO simulation in CST before and after TG

5.1.2 Power Normalization of Channel Matrix

As mentioned in the introduction, the power levels assumed to be available at the Tx aperture in the MATLAB code are not the same as the power available at the aperture location when running a CST

simulation. This difference is because the coupling h_{11} from the channel matrix model is the coupling between the Tx aperture and Rx aperture, but the S parameter S_{21} from CST after TG is the coupling between the Tx antenna port and the Rx antenna port, and there is a radiation efficiency between the power on the aperture and the power to the antenna port, introduced in Section 2.1.2. In the simplified current-distribution model, the coupling between two apertures is defined as eq. 2.40 in Section 2.2.3. It is repeated below:

$$h_{ij} = \frac{(V_{oc}I_0)^{ij}}{\sqrt{16P_{rad}P_{rad}}} \quad [5.4]$$

Where P_{rad} is the power radiated by the Tx and Rx apertures (note that the current distributions are the same at Tx and Rx and therefore there P_{rad} are the same). By contrast, from the CST simulation, the S_{21} between two ports is:

$$S_{21} = \frac{V_2^-}{V_1^+} \quad [5.5]$$

Where V_1^+ is the input voltage at the Tx port and V_2^+ is the output voltage at the Rx port. Therefore, viewing the CST simulation similarly we can write it as the channel matrix in the following way:

$$h_{ij}^{CST} = \frac{(V_{oc}I_0)^{ij}}{\sqrt{16P_{in}^{CST}P_{in}^{CST}}} \quad [5.6]$$

Where P_{in}^{CST} is the Tx port input power to the CST simulation, as shown in Figure 5.5. The signal with this power level is propagated through the waveguide and lens, giving a specific field at the location of the lens aperture. This field is shown in the middle image of Figure 5.5. It is very different from the perfectly uniform fields used in the MATLAB code as shown in the right-most image of Figure 5.5. The fields on the aperture above the lens (field in the middle of Figure 5.5) can be integrated using, eq. 2.34 in Section 2.2.2, over the aperture are to obtain the power level, P_{ap}^{CST}. The ratio between the CST input power and the power on the equivalent aperture is defined as the radiation efficiency of the waveguide and lens:

$$\eta_{rad} = \frac{P_{ap}^{CST}}{P_{in}^{CST}} \quad [5.7]$$

To be able to compare the results of the TG S-parameters to the channel matrix we must normalize the channel matrix with this radiation efficiency as follows:

$$h^{norm} = \eta_{rad}h \quad [5.8]$$

Where this radiation efficiency η_{rad} is calculated in Section 4.3.3.2 for uniform lens antenna and in Section 4.4.3.2 for Gaussian focused lens antenna.

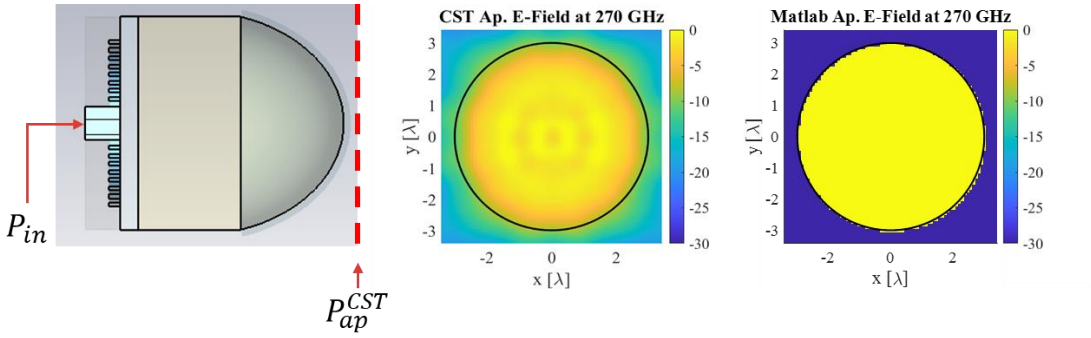

Figure 5.5 The modelled aperture electric field in MATLAB and the actual aperture electric field in CST

5.1.3 Comparison of Channel Matrix and S-Parameters

After time-gating the S parameters and normalizing the channel matrix, we can now compare the two. Let us compare the time-gated S_{21} and the normalized h_{11} over frequency at three distances, shown in Figure 5.6.

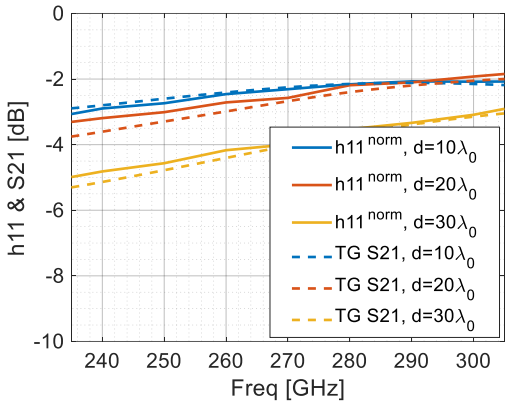

Figure 5.6 The normalized h_{11} and S_{21} after time gating with $d = 10\lambda_0, 20\lambda_0$ and $30\lambda_0$

In Figure 5.6, the normalized h_{11} (solid lines) and the time-gated S_{21} (dash lines) have good agreements, with around 0.4 dB difference in maximum.

Then, we will compare the time-gated S_{21} and the normalized h_{11} at 270GHz over the link distance in Figure 5.7. This shows a good agreement between the two parameters and allows us to use the CST simulations to validate the MATLAB model. This good agreement gives us enough confidence to apply these data-processing steps to the following simulations, lens arrays with both uniform lens antenna and Gaussian focused lens antenna. Since the data-processing steps are the same for the SISO and MIMO with both Gaussian focused lens antenna and uniform lens antenna, we will not introduce this data-processing in the later simulation again.

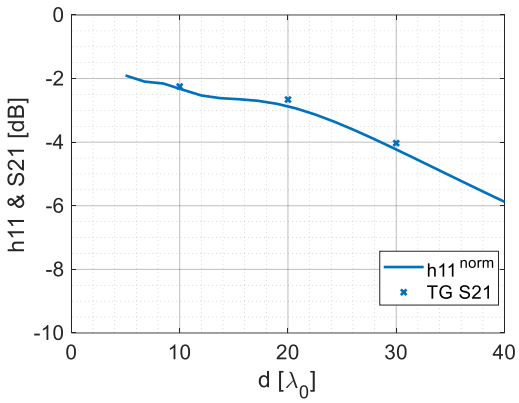

Figure 5.7 Time-gated S_{21} and normalized h_{11} for a single communication link, calculated at $f = 270GHz$, over link distance.

5.2 Full Wave Array Simulations

In this section, we will introduce the FW simulations for 2×2 arrays of uniform and Gaussian focused lens antennas. Since the range of interest for our application is $d \in [10\lambda_0, 30\lambda_0]$, we will simulate in CST at three distances: $d = 10\lambda, 20\lambda, 30\lambda$. The FW simulation environment for both arrays is discussed in Section 5.2.1. The results of these simulations for the uniform lens and the Gaussian focused lens are discussed in Sections 5.2.2 and 5.2.3, respectively. In these sections, the results are also compared to the results of the MATLAB code using the post-processing techniques of Section 5.1. The performance of the two in terms of capacity will be discussed in Section 5.3.

5.2.1 Full Wave Lens Array Simulation Environment

The simulation environment for the 2×2 arrays of the uniform lens antenna is shown in Figure 5.8 and that of the Gaussian focused lens antenna is shown in Figure 5.9. In both cases, the arrays are located in the x-y-plane facing each other and separated by a distance d (between the tops of the lenses). The individual lens antennas used are described in Section 4.3 for Figure 5.8 and the one in Section 4.4 for Figure 5.9. Each antenna is illuminated by a waveguide port. The waveguide ports on the Tx array are numbered 1 through 4, and those on the Rx array are numbered 5 through 8. The reference plane of each port is located one wavelength below the ground plane, in the waveguide.

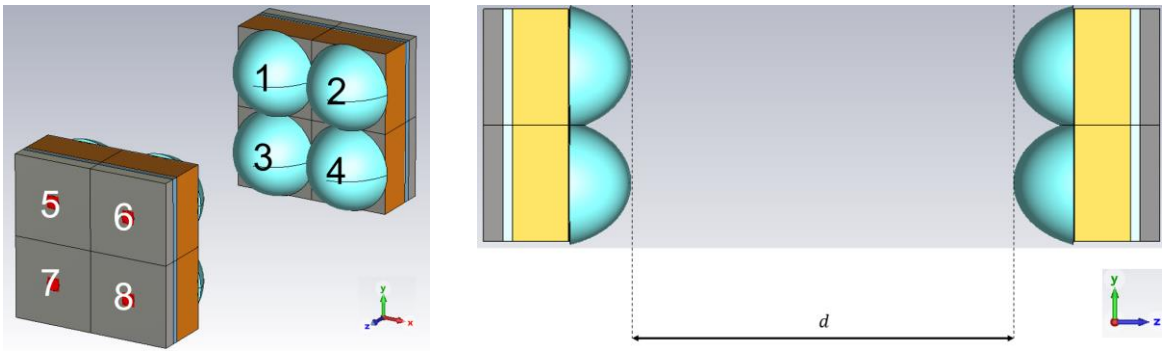

(a) *(b)*

Figure 5.8 The simulation environment for the 2×2 arrays of the uniform lens antenna

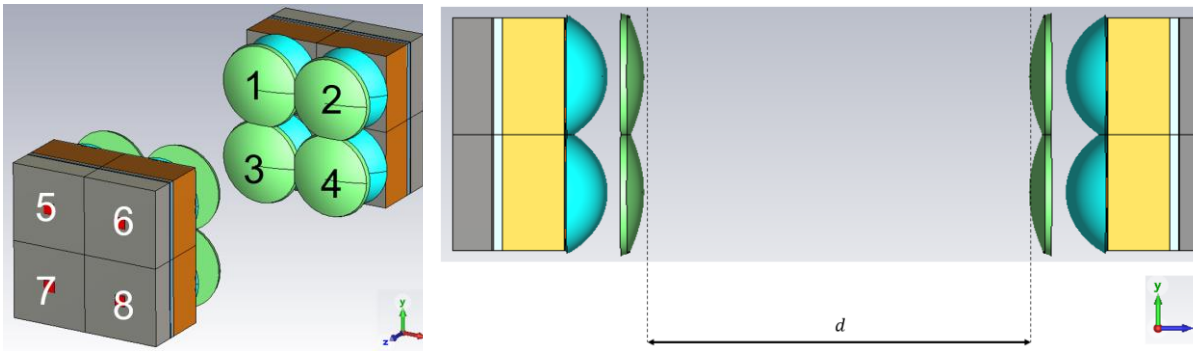

(a) (b)

Figure 5.9 The simulation environment for the 2 × 2 arrays of the Gaussian focused lens antenna

The FW simulation is performed in the time domain solver. The background material is filled with vacuum, and the boundary conditions at the x, y, and z directions are all set as open (add space). The simulation terminates when the energy in the simulation drops to -40dB compared to the input energy. The frequency band is limited in $f \in [235GHz, 305GHz]$. During the simulation port 1 is excited. From this radiated signal, the coupling to all other apertures is retrieved from CST through the S-parameters. The simulations are performed over three distances, $d = 10\lambda_0, 20\lambda_0, 30\lambda_0$.

Due to the symmetry of the array, assuming the GO currents are rotationally symmetric, it is only necessary to excite one port. From this one simulation the S parameters S_{51}, $S_{61}$and S_{81} are sufficient to represent all the S parameters in this simulation as $S_{16} = S_{17}$. The S parameters S_{51}, $S_{61}$and, S_{81} are the ones which will be compared to the channel matrix entries h_{11}, h_{12} and h_{14}. The mapping between the channel matrix and these S parameters are:

$$\bar{\bar{H}} = \begin{bmatrix} h_{11} & h_{12} & h_{12} & h_{14} \\ h_{12} & h_{11} & h_{14} & h_{12} \\ h_{12} & h_{14} & h_{11} & h_{12} \\ h_{14} & h_{12} & h_{12} & h_{11} \end{bmatrix} \rightarrow \begin{bmatrix} S_{51} & S_{61} & S_{61} & S_{81} \\ S_{61} & S_{51} & S_{81} & S_{61} \\ S_{61} & S_{81} & S_{51} & S_{61} \\ S_{81} & S_{61} & S_{61} & S_{51} \end{bmatrix} \quad [5.9]$$

From eq. 5.9, we will compare h_{11} with S_{51}, h_{12} with S_{61}, and h_{14} with S_{81} after data-processing.

5.2.2 Uniform Lens Array

As introduced above, based on the symmetry of the channel matrix and the geometry of the MIMO arrays, S_{51}, S_{61} and S_{81} are sufficient to represent the behaviour of the system. The FW S parameters and the TG S parameters are shown in Figure 5.10 for three different link distances. Since the lenses are very directive, the co-coupling S_{51} is much higher than that of the interferences S_{61} and S_{81},in the array. From Figure 5.10(a) one can see that as the link distance increases, the coupling decreases while the interference increases as expected. It is also obvious that the magnitude of the ripples of the FW signal decreases with link distance. This will be further studied in Chapter 6.

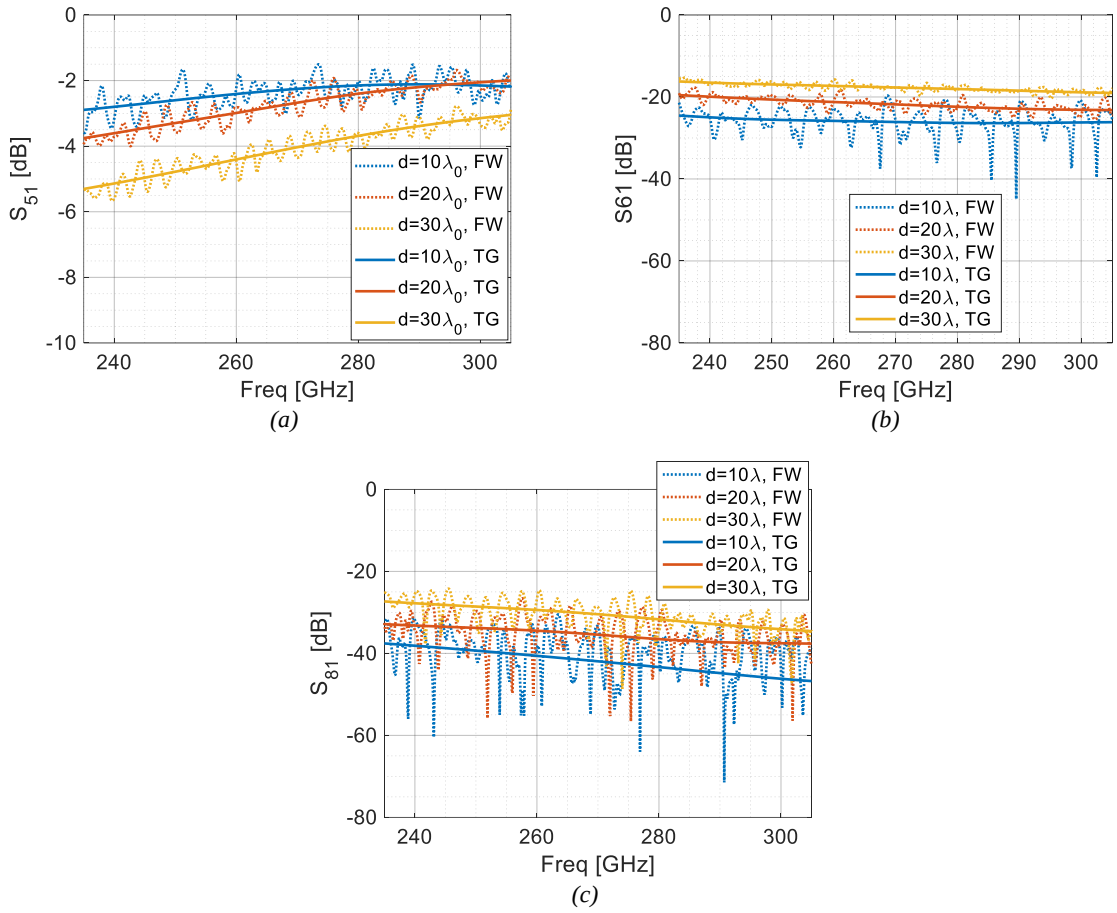

Figure 5.10 The (a) S_{51}, (b) S_{61} and (c) S_{81} of CST simulation for three link distances before (dot line) and after (solid line) time-gating

From Figure 5.10, it can be observed that the FW S-parameters fluctuate around the TG S-parameters. As introduced in Section 5.1, the difference between the FW S-parameters and the TG S-parameters is that the FW S-parameters contain the multi-path signals. These multi-path signals are in form of ripples in frequency domain. Using the normalized channel matrix, calculated using eq. 2.40 from Section 2.2.3, the results from CST and MATLAB for the array can be compared. These results are plotted together, over frequency, in Figure 5.11. Since the comparison of h_{11} is in Figure 5.6 from 5.1.3, we will only show the h_{12} and h_{14} here.

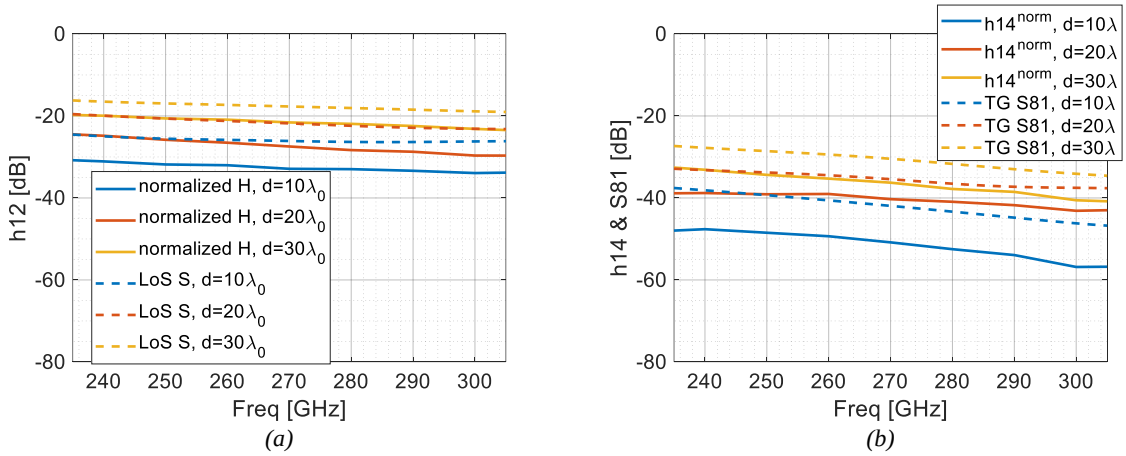

Figure 5.11 The comparison between normalized channel matrix of GO currents (solid line) and time-gated S parameters of CST simulation (dash line) in (a) h_{12} and S_{61} (b) h_{14} and S_{81} for three link distances

From Figure 5.6 and Figure 5.7, the co-coupling pair h_{11} and S_{51} shares a good agreement over frequency after TG and normalization; however, the interference pairs h_{12} and S_{61}, h_{14} and S_{81} have around 5dB difference between the time-gated S parameters and the normalized channel matrix. This might because the GO approximation is not that accurate here.

Fixing the frequency to 270 GHz, the results for the TG S-parameters and the channel matrix are also compared versus link distance. This is shown in Figure 5.12.

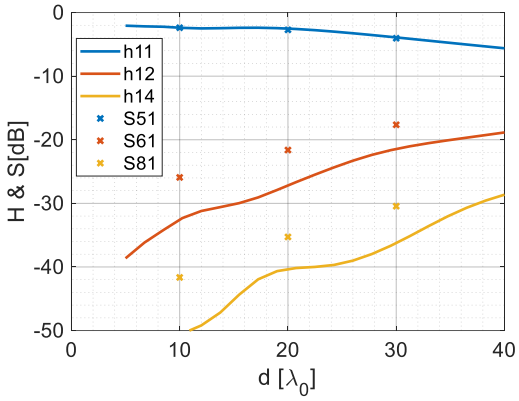

Figure 5.12 The normalized channel matrix of GO current (solid lines) and the time-gated S parameters from CST (cross markers) at 270 GHz over link distances

Figure 5.12 also shows the agreement in co-coupling term and the difference in interference terms, this results basically match with the results from Figure 5.11.

We can calculate the capacity of the uniform lens from the normalized S parameters and the normalized channel matrix from GO current. Applying eq. 2.50 and the parameters introduced in Section 2.3.4, the capacity is shown in Figure 5.13.

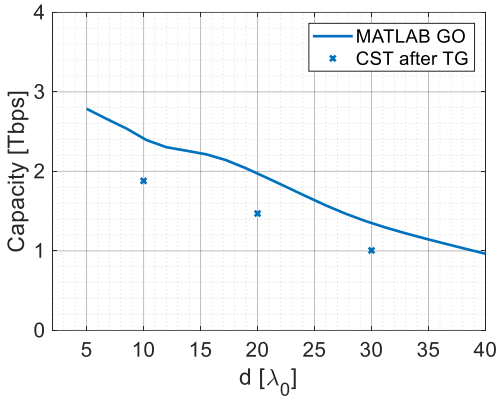

Figure 5.13 The capacities calculated with normalized channel matrix of GO current (solid line) and with time-gated S parameters from CST simulation (cross marker)

Without a good agreement in the channel matrix, the agreement between the capacities from time-gated S parameters and normalized channel matrix from GO current are not good.

5.2.3 Gaussian Focused Lens Array

Similar to the array of uniform lens antennas, the S_{51}, S_{61} and S_{81} are sufficient to represent the behaviour of the system and will be used to compare to the channel matrix in the FW simulation of Gaussian focused lens antenna. These three S-parameters at three distances are shown in Figure 5.14.

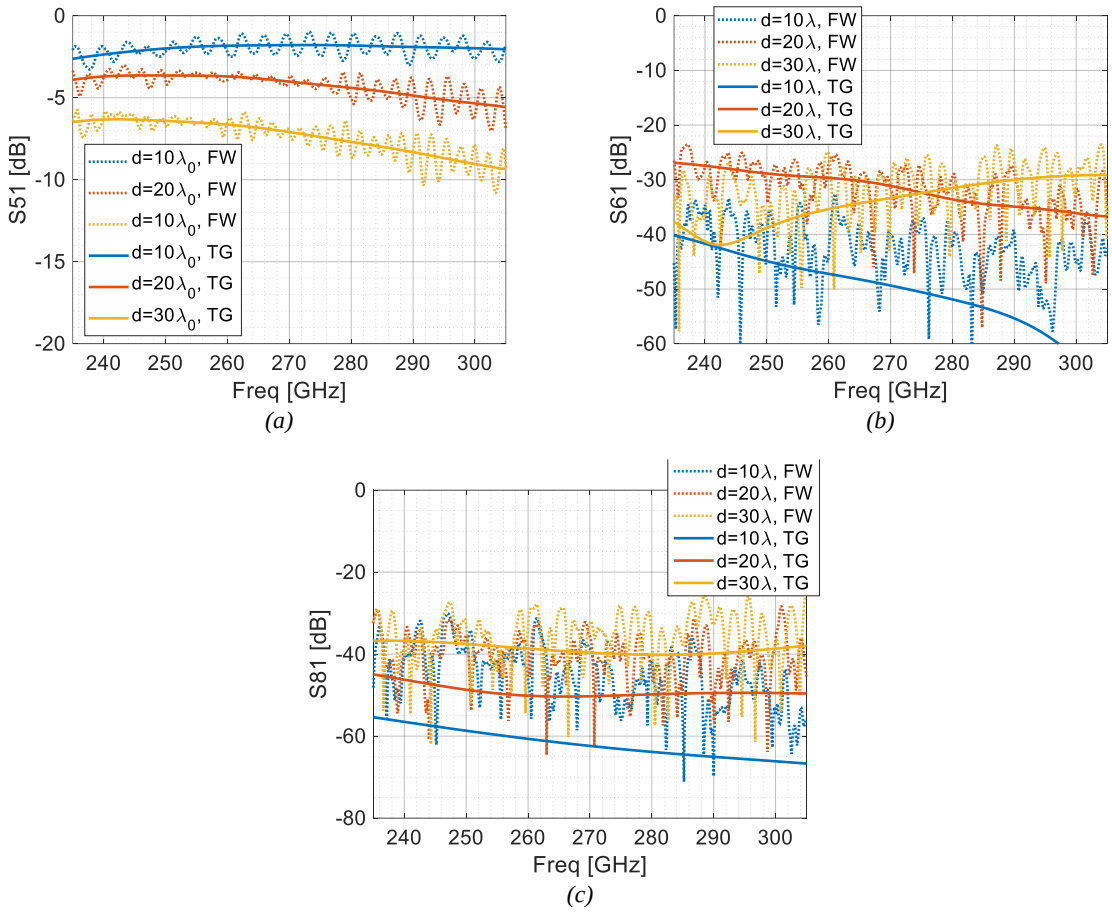

Figure 5.14 The (a) S_{51}, (b) S_{61} and (c) S_{81} of CST simulation for three link distances before (dot line) and after (solid line) time-gating

From Figure 5.14(a), the FW S_{51} fluctuate around the TG S_{51}. However, from Figure 5.14(b) and Figure 5.14(c), unlike the uniform lens, the level of some FW S_{61} and S_{81} are higher than the TG S_{61} and S_{81}. This is because here the LoS interferences are well suppressed, but the multi-path interferences (reflections) are still high, making the multi-path interferences to be the dominating signals. As a result, the multi-path signals take the dominating contribution to some FW S_{61} and S_{81}. With this result, we know that for an array with highly-directive elements, it is not enough only to consider the direct coupling signals, we also need to consider the reflection signals. This will be studied and quantified in Chapter 6.

Same as Section 5.2.3, we will then compare the normalized channel matrix from GO current and the time-gated S parameters from CST over frequency at three link distances, shown in Figure 5.15.

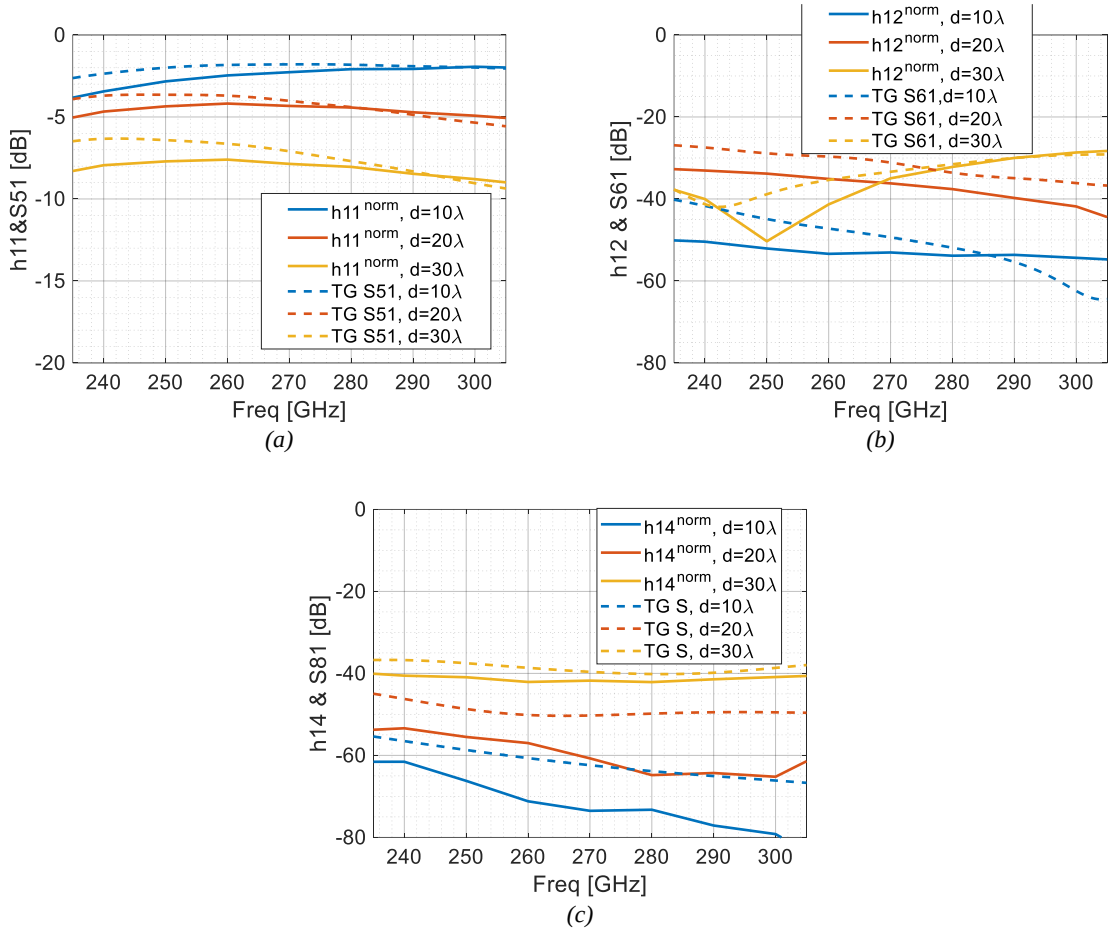

Figure 5.15 The comparison between normalized channel matrix of GO currents (solid line) and time-gated S parameters of CST simulation (dash line) in (a) h_{12} and S_{61} (b) h_{14} and S_{81} for three link distances

From Figure 5.15, the agreements between the normalized channel matrix from GO current and the time-gated S parameters are acceptable. In co-coupling channel, the differences are around 2dB in lower frequency; in interference channels, the differences are around 5dB to 10dB. We find that the difference is especially higher in the interference in the near distance $d = 10\lambda_0$. This might because that the interference code will be not accurate when two misaligned apertures are in a close link distance, and when the coupling level is too low. But we can still trust these results.

Applying the time-gated S-parameters and the normalized channel matrix at 270GHz, the comparison between the time-gated S-parameters and the normalized channel matrix over distance are shown in Figure 5.16.

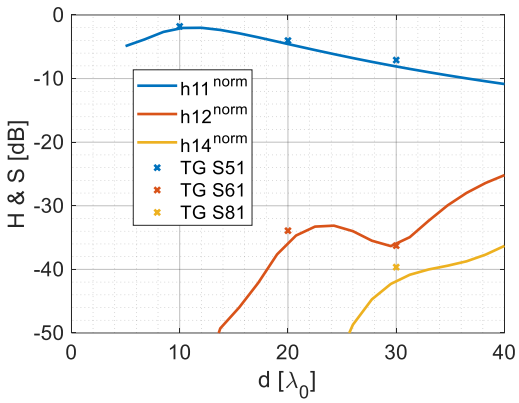

Figure 5.16 The normalized channel matrix of GO current (solid lines) and time-gated S-parameters from CST (cross markers) at 270 GHz

Figure 5.16 shows a good agreement between the channel matrix and the S-parameters at the center frequency. To evaluate the capacity, we need to use the normalized channel matrix and the time-gated S-parameters at each frequency. Applying eq. 2.50 and the parameters introduced in Section 2.3.4, the comparison of the capacities from MALTAB and CST is shown in Figure 5.17.

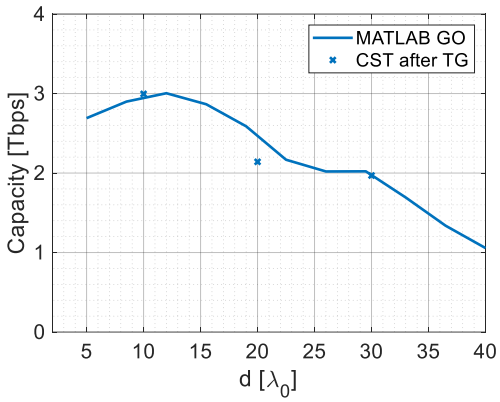

Figure 5.17 The capacities calculated with normalized channel matrix of GO current (solid line) and with time-gated S-parameters from CST simulation (cross markers)

The capacity results in Figure 5.17 shows a good agreement between the S parameters and the channel matrix. Since it takes days to simulate the FW simulation in CST, and we have good agreements at three chosen distance, we can use the capacity from channel matrix results to represent the CST results.

5.2.4 Comparison of Uniform and Gaussian Focused Lens

The comparison of capacity calculated from the time-gated S parameters from simulation in Figure 5.8 (uniform lens antenna) and the one calculated from the time-gated S parameters from simulation in Figure 5.9 (Gaussian focused lens antenna) are shown in Figure 5.18.

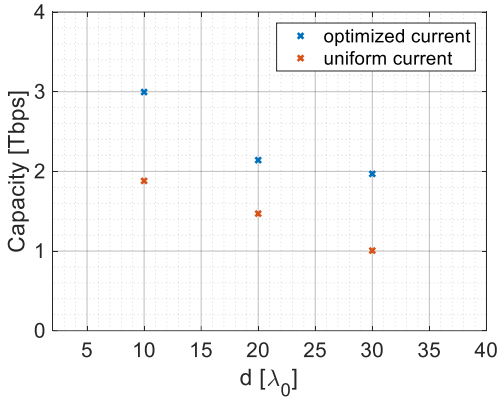

Figure 5.18 The capacities calculated from time-gated S parameters of Gaussian focused lens antenna simulation (blue cross markers), and from time-gated S parameters of uniform lens antenna simulation (red cross markers)

From Figure 5.18, the capacity of the Gaussian focused lens antenna is almost double than the one of the uniform lens antenna in these three distances $d = 10\lambda_0, 20\lambda_0, 30\lambda_0$. At $d = 20\lambda_0$, the improvement is not that significant, and we already knew this is because the phase error, can be fixed with lens shaping in the future.

6 Effect of Reflections in the Radiative Near Field Between Lens Antennas

In Chapter 5, the FW CST simulations of the MIMO array were shown for both the uniform and the Gaussian focussed lens antennas. In the FW results of the direct coupling, many oscillations had to be removed through time-gating to be able to compare the results of the channel matrix. These oscillations are due to reflections in the signal path from, for example, air/dielectric interfaces and the ports of the antennas. These reflections have a large impact on the performance of the communication links and will therefore be studied in this chapter.

We will study the effect of reflections on both of the Gaussian focused lens antenna and the uniform lens antenna in Section 6.1 and Section 6.2 respectively. For each of them, we will study the reflections on the direct coupling path and on the interference paths. It is important to know their origin to find out what causes the reflections for two reasons. Firstly, one could find out if it is possible to remove the object causing these reflections or try to minimize the reflections this causes in future designs. With the knowledge of the origin of the reflections it also becomes possible to model this in the MATLAB code. This chapter will close with a study of the effect of the FW oscillations on the array's capacity. Our channel matrix model does not include the reflections, so in this chapter, we will evaluate the effect of the reflections based on CST simulations.

6.1 Gaussian Focused Lens Antenna Array

In this section we will study the effect of the reflections on direct coupling (co-coupling) for the FW simulation of the Gaussian focused lens antenna in Figure 5.9. As mentioned in Chapter 5, we have the FW S parameters from the simulation in Figure 5.9 and three S parameters from CST S_{51}^{FW}, S_{61}^{FW} and S_{81}^{FW} are sufficient to represent the behavior of the MIMO array based on the symmetry of the channel matrix and the antenna array. After TG, the time-gated S parameters only represent the effect of the LoS path. In particular, S_{51}^{TG} is the S parameter between the desired channel, regarded as the co-coupling ,and S_{61}^{TG} and S_{81}^{TG} are the S parameters between the cross channel, regarded as the interference. The co-coupling is the signal we want, putting as the nominator in eq. 2.52 to calculate the capacity; the interferences are the signal we do not want, putting as the denominator in eq. 2.52. This is the case we applied in Chapter 5, regardless of the reflections.

However, we cannot apply the TG in real time communication, and we need to calculate the capacity with FW S-parameters without TG, where the reflection signals are included. The FW S-parameters from the CST can be separated as the LoS signals and the reflection signals:

$$S_{51} = S_{51}^{TG} + S_{51}^{reff} \quad [6.1]$$

$$S_{61} = S_{61}^{TG} + S_{61}^{reff} \quad [6.2]$$

$$S_{81} = S_{81}^{TG} + S_{81}^{reff} \quad [6.3]$$

Where S_{51}^{TG} is identified as the co-coupling (wanted signal), and S_{61}^{TG} and S_{81}^{TG} are the interferences (unwanted signals) in Chapter 5. The reflection signals always arrive at the receiver with time delay, leading to a significant reduction in capacity. In this section, to study the negative effect of the reflections, we will assume that we cannot deal with the reflection signals and treat these reflection signals as part of the interference (unwanted signals).

In the view of calculating signal level and interference level, in the co-coupling channel, S_{51}^{TG} is the signal and S_{51}^{reff} is the interference; in the cross-coupling channel, both time-gated S parameters S_{61}^{TG} and S_{81}^{TG} and the reflection effects S_{61}^{reff} and S_{81}^{reff} are the interferences:

$$P_{sig}(f) = \sum_{i=1}^{4} P_t(f)\left|h_{ii}^{TG}(f)\right|^2 \left[\frac{W}{Hz}\right] \quad [6.4]$$

$$P_{int}(f) = P_t(f)\left|h_{ii}^{ref}(f)\right|^2 + \sum_{j=1,j\neq i}^{4} P_t(f)\left|h_{ij}(f)\right|^2 \left[\frac{W}{Hz}\right] \quad [6.5]$$

Here the reflection signals are calculated in the interference power. Both LoS and reflections signals in the cross-coupling term are treated as the interference, so we can use the FW S-parameters directly in eq. 6.5; for the co-coupling channel, the LoS signal will be treated as the wanted signal and the reflection signals are treated as the interference, so we need to separate S_{51}^{TG} and S_{51}^{reff}. This will be introduced in Section 6.1.1. Applying the mapping between channel matrix and S parameters shown in eq. 5.9, we can calculate the signal and interference powers to calculate the capacity.

6.1.1 Effect of Reflections

We will first introduce the data processing and study the effect of the reflections in Section 6.1.1.1, and then study the reflection sources in Section 6.1.1.2.

From eq. 6.4 and 6.5, we need to separate the effect of the reflections and the effect of the LoS signal from the FW simulation. We already have the LoS path signals in Figure 5.14 from Section 5.2.3. Now we need the reflection signal. As introduced in Section 5.1.1, the received signals in the time domain contain both the LoS signal and reflection signals. The LoS signal is the first pulse, the rest of the pulses are all reflections. Unlike what we did in Section 5.1.1, we will filter out the pulse representing direct coupling and to obtain only the multi-path pulses. Figure 6.1 shows an example of this time gating with a link distance of $d = 10\lambda_0$.

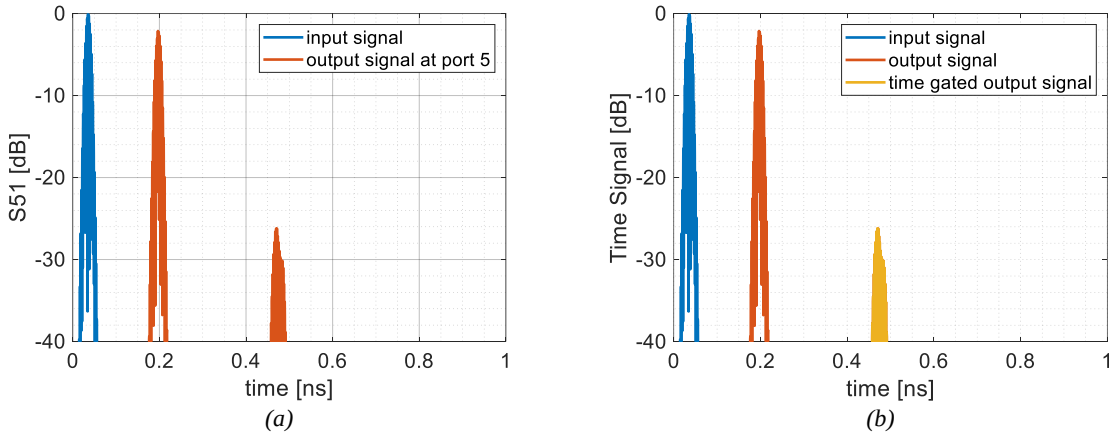

Figure 6.1 The received time signal at port 2 (a) before time gating and (b) after time gating (yellow line)

From Figure 6.1, the first output pulse representing the direct signal is filtered out, and the rest of them remains. Applying the FT onto the time signal after time gating, we can have the S_{51}^{ref} at $d = 10\lambda_0$, $d = 20\lambda_0$ and $d = 30\lambda_0$, shown in Figure 6.2.

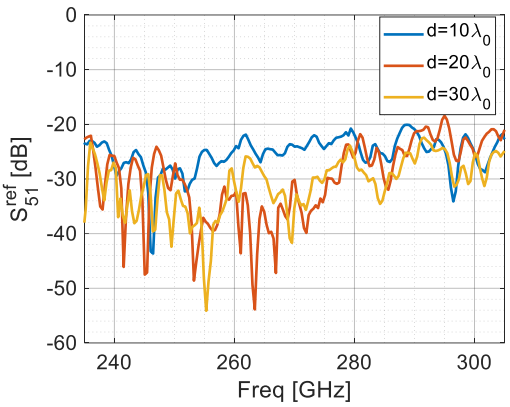

Figure 6.2 The effect of reflections on S51 of Gaussian focused lens array CST simulation in Figure 5.9

From Figure 6.2, the reflection signals are around -20dB with $d = 10\lambda_0$, and being around -30dB with $d = 20\lambda_0, 30\lambda_0$. From Figure 3.18 in Section 3.5.2, the SNIR without reflections of our MIMO communication with optimized currents distribution is around 30dB. This means that the reflection signals will influence the SNIR significantly, and then decrease the capacity. To quantify this negative effect, we will calculate the capacities with and without considering the reflection. We have the capacity without considering the reflections in Chapter 5. To calculate the capacity with reflections, we will use eq. 6.4 and 6.5 to calculate the signal and interference power, and then calculate the capacity based on eq. 2.52.

However, there are two kinds of reflections: the reflections in the co-coupling channel and the reflections in the cross-coupling channel, and both reflections are considered as the interference terms. We need to find which reflection is the dominating reflection that leads to this significant capacity drop. To study that, we decide to calculate the capacity in another case: only consider the reflection on the interference S_{61} and S_{81} but not consider the reflection on the co-coupling S_{51}. Applying the eq 6.4 and 6.5 and eq. 2.52 with $S_{51}^{ref} = 0$, we can have the capacity with reflection in cross-coupling and without reflection in co-coupling. The capacities of the Gaussian focused lens MIMO array in CST with both reflections from co-coupling and from cross-coupling, with reflections from cross-coupling only and without reflections are shown in Figure 6.3.

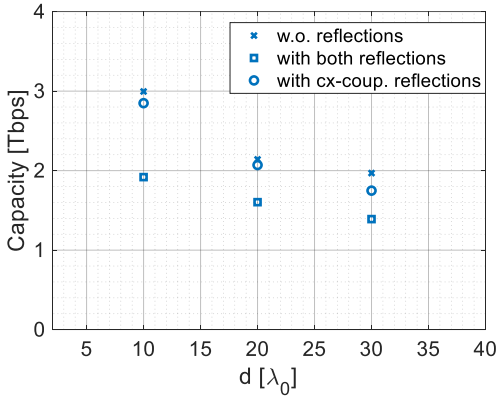

Figure 6.3 The capacities of CST simulation in Figure 5.9 without reflections (blue cross markers), with both reflections in co-coupling and cx-coupling (blue square markers) and with only reflections in cx-coupling (blue circular markers)

From Figure 6.3, adding the reflections from the cross-coupling channel, the capacity does not drop significantly. But if we add the reflections from the co-coupling too, the capacity drops around 50%. So, considering the reflections in our research is essential, and the main negative effect comes from the reflections from the co-coupling channel.

6.1.2 Pulse Analysis

We need to find the source of these reflections by pulse track. To find the light path of each pulse, we will apply eq. 5.1 from Section 5.1.1 to calculate the path length of each pulse, and then find the light path according to the physical distance in CST simulation. Since we knew that the reflections in the co-coupling channel take the dominating effect on the capacity reduction, we will study the co-coupling reflection in Section 6.1.2.1. In case we need to optimize the reflection effect from the cross-coupling channel, we will study the cross-coupling reflection in Section 6.1.2.2.

6.1.2.1 Co-coupling channel

When looking for the source of the reflections, one can start by looking at the time domain of the signal. It is widely known that the reflections in co-coupling channel are stronger when two faced antennas are closer. As a result, we chose the simulation with the closest link distance $d = 10\lambda_0$ to study the reflection in co-coupling. Different from what was done for the time-gating, we are now interested in finding out when the pulses of energy other than that of the direct signal are received by the Rx port.

Reflections are usually caused by an impedance mismatch. Therefore, by looking at the signal path of the link in Figure 6.4, we can see that there are a couple of possible interfaces which could cause the reflections. These are reflections from the ports and the air/dielectric interfaces of the lenses.

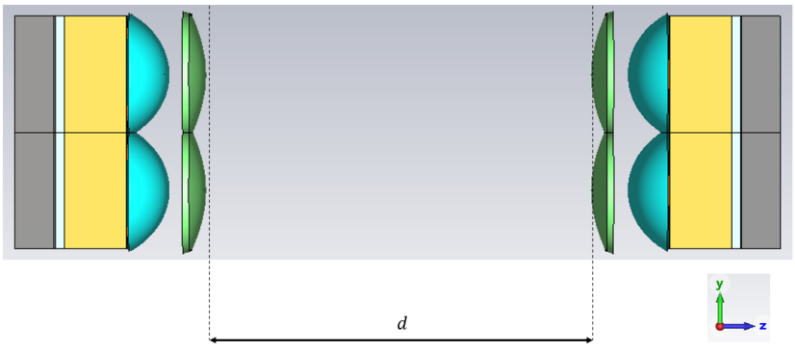

Figure 6.4 The Link of the simulation

There are actually many air/dielectric interfaces that will result in reflections (e.g. top of the elliptical lens, top/bottom of the hyperbolic lens) on the Gaussian focused antenna. Considering the distances between these interfaces are extremely close, the light path of these reflections will be more or less the same, resulting in an overlapped pulse in the time domain. Because of these, we will consider these reflections as one. The TD signal of the FW simulation of the link in Figure 6.4 is shown in Figure 6.5. For both plots, the blue peak represents the input signal to port 1. In Figure 6.5(a) the red peaks represent the energy received over time, by port 2, and in Figure 6.5(b) the red peaks represent the energy received over time, by port 1. Since the ideal SNIR is around 30dB, we are only interested in the reflection signals larger than -40dB, and the dynamic range is set to [-40dB,0].

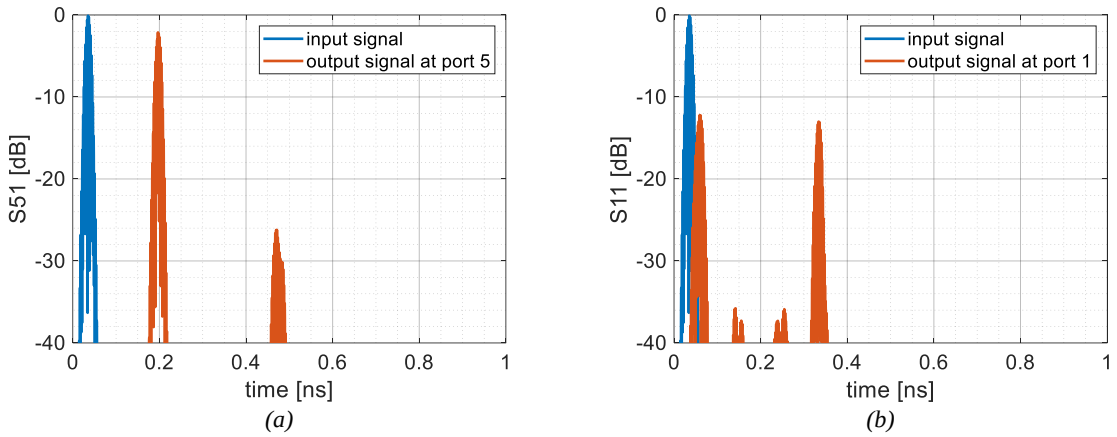

Figure 6.5 TD signal of FW simulation of single link shown in Figure 6.1. (a) the energy received over time by port 2 and (b) the energy received over time by port 1 in the same simulation.

Taking into account the different dielectric constants, ε_r of the lens and ε_0, one can attempt to trace the path of the signals followed by calculating the distance the signals traversed based on the time they were received by port 2 according to eq. 5.1 in Section 5.1.1. The paths corresponding to the 2 peaks in Figure 6.5(a) are shown in Figure 6.6(a). The first, and largest, peak corresponds to the LoS signal. The second peak corresponds to a reflection from both ports before being received by the Rx port.

The reflections of the dielectric/air interface are not presented in Figure 6.5(a). This is because that in the design of the lens we have added matching layers to reduce reflections and thereby increase the radiation efficiency. To show the effect that the matching layer has on the reflections the TD signals for both cases are shown in Figure 6.5(b). Here, the red pulses represent the energy received by port 1.

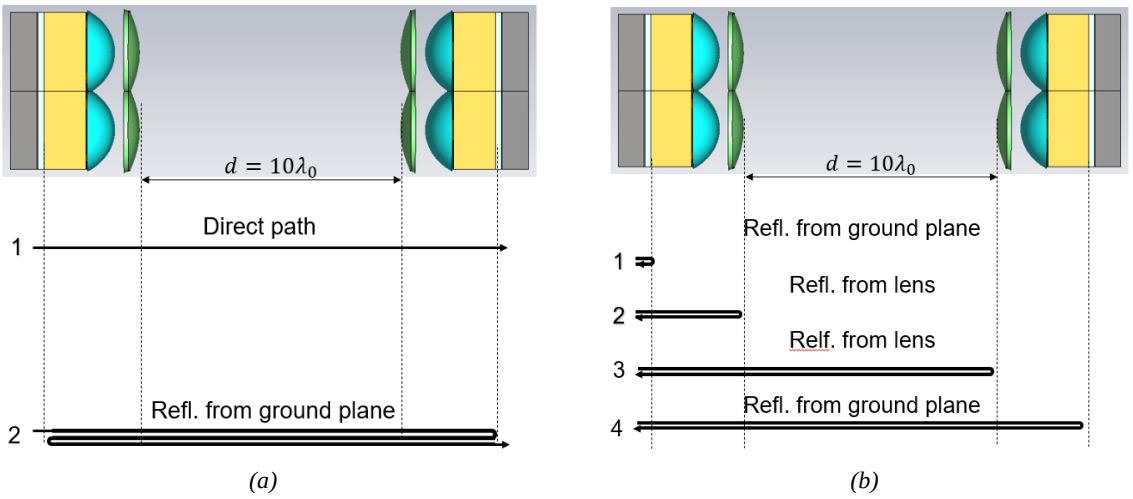

Figure 6.6 Signal path representing (a) the reflections in Figure 2 (a) and (b) the reflections in Figure 6.2 (b) .

Looking at Figure 6.5(b), there are more considerable reflections received by the Tx port compared with Figure 6.5(a). The same analysis of finding the origin of the reflections is shown in Figure 6.6(b). Since the signal paths here are simpler, the first four reflections are considered. The first reflection is due to the matching of the Tx port, the Γ, the second is a reflection from the Tx lens, the third is a reflection from the Rx lens and the fourth is a reflection from the Rx port, the Γ. Since the radiated field in the radiative near field remains very collimated, the power reflected from the Rx port will be significant if it is not well matched. This is therefore a constraint on the design of the Γ of the feeds near field communication.

From these results, it is clear that a matching layer for the lenses and good matching of the feeds are critical in minimizing reflections for communication systems that operate in the radiative near field. As the link distances become larger, For the S_{11}, the reflections from the Rx antenna will decrease, however the reflections from the Tx antenna itself remain; for the S_{51}, the reflections will decrease.

We find that there are two main sources of the reflections: the port and the dielectric-to-air interface. The reflections from the dielectric-to-air interface are already well-suppressed by using a ML, leading to that the reflections from the port being the dominating reflections.

To verify that the reflections in the co-coupling channel are from the port, we can compare the reflection coefficient Γ and the reflection signals. From Figure 4.35, the reflection coefficient Γ of the Gaussian focused lens antenna is around -10dB. With two times reflection from the port of both Tx and Tx ports, the attenuation led by the port reflection is around -20dB. Compared with the level of reflections in Figure 6.1, the level of co-coupling reflections with link distance $d = 10\lambda_0$ is more or less at the same level as the attenuation by reflections, -20dB. This agreement evaluates that the main reflection source is the reflection from the source.

The reflection from the source can be optimized with a better impedance match. To reach the SNIR level of around 30dB, if the reflection coefficient Γ of the Gaussian focused lens antenna is around -20dB, the reflection will not affect the capacity significantly. This gives us enough confidence to solve the multi-path effect problem in our near-field communication scenario without signal processing, by only antenna design, and this will be included in future work.

6.1.2.2 Cross-coupling channel

There are two different interference terms: S_{61} and S_{81}, and we will study the effect of the reflection onto these two.

6.1.2.3 Effect of the Reflections

Unlike in Section 6.1.1, the reflections in co-coupling are stronger with closer link distance, the reflections in the cross-coupling channel are stronger when the distance is further. As a result, we will show an example of time signals of S_{61} and S_{81} of FW simulation with link distance $d = 30\lambda_0$, shown in Figure 6.7(a) and Figure 6.7(b) respectively.

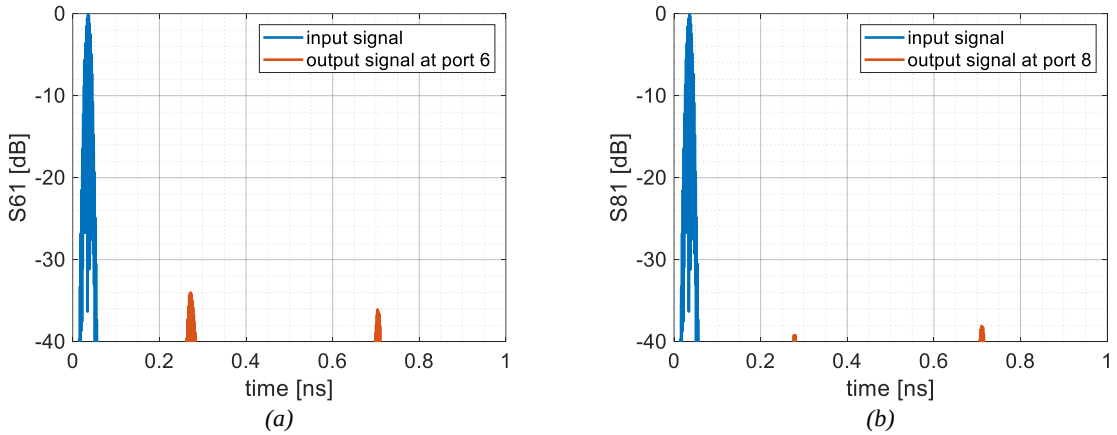

Figure 6.7 TD signal of (a) the energy received over time by port 6 and (b) the energy received over time by port 8 in the simulation in *Figure 5.9*

From Figure 6.7, the LoS pulse is around -35dB in both interferences. However, we can find that the reflection signal levels are more or less the same as the LoS signal levels in Figure 6.7, being 4dB lower in S_{61} and 4dB higher in S_{81}.

From Figure 6.7, the reflection signal is in more or less the same level with the LoS signal, which is impossible if the reflections are from the port. By applying the ray tracing, the reflection paths are shown in Figure 6.8.

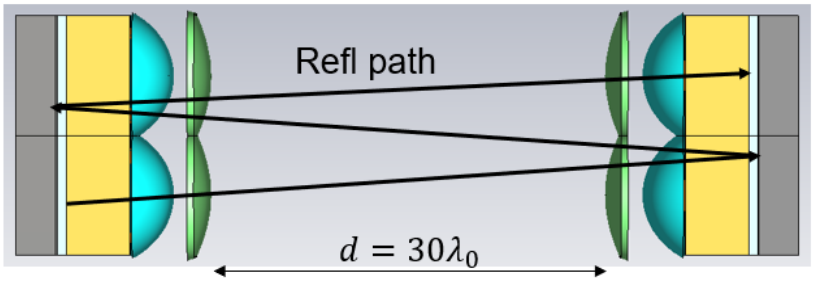

Figure 6.8 Pulse tracking of the reflection signal

From Figure 6.8, the reflection in S_{61} is the reflection from the ground plane. The reflection in S_{81} is is equivalent to the reflection from the ground plane but on a different path, we will not plot it again. This light path is no longer a normal incident on the air/dielectric interface in this case, so the light path should not be straight, but that will be difficult to demonstrate. To efficiently study, we just use a straight line to represent.

We find that the reflection is from the ground plane. However, we cannot fix it by removing the ground plane because it is a critical component in the LW lens antenna. If we need to fix this error, we need to find another way. From Figure 6.3, these reflections will not decrease the capacity significantly, so we can leave this for now.

6.2 Uniform Lens Antenna Array

Same as in Section 6.1, we will study the effect of the reflections on the simulation of the uniform lens antenna array in Figure 5.8. Because the data-processing and reflection sources are the same, we will only show the effect of the reflections in this section, skipping the data-processing and pulse analysis.

Applying the same approach in Section 6.1.1, using TG to filter out the LoS signal in co-coupling S_{51}, the reflection signals in co-coupling S_{51} at $d = 10\lambda_0, 10\lambda_0\ and\ 10\lambda_0$ are shown in Figure 6.9.

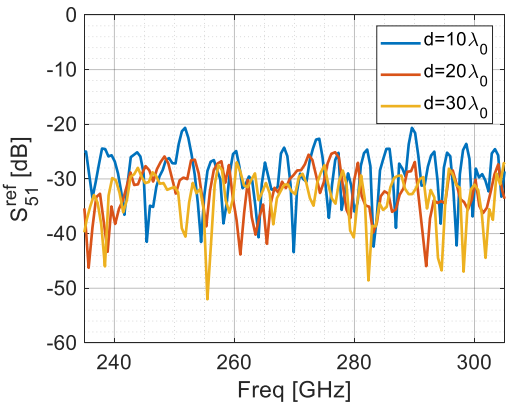

Figure 6.9 The effect of reflections on S51 of uniform lens array simulation in Figure 5.10

From Figure 6.9, the reflection signals are around -30dB. From Figure 2.13 in Section 2.3.3, the SNIR without reflections of our MIMO communication with uniform current is in the range [25dB, 12dB] in the interested link distance range. This means that the reflection signals will influence the SNIR when the link distance is close, and will not when the link distance is far.

Same as Section 6.1, we will show the capacities without reflections, with reflections in the cross-coupling channel and with both reflections in the co-coupling and cross-coupling channel in Figure 6.10 to evaluate the effect of the reflections from different sources.

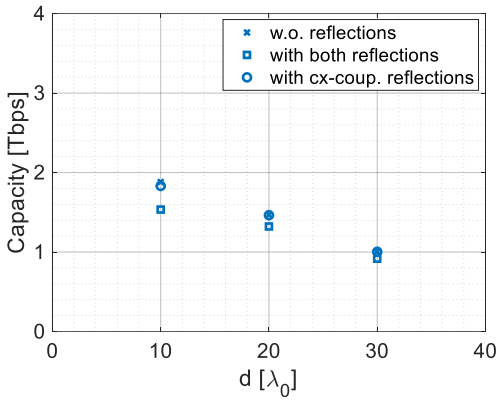

Figure 6.10 The capacities of CST simulation in Figure 5.10 without reflections (blue cross markers), with both reflections in co-coupling and cx-coupling (blue square markers) and with only reflections in cx-coupling (blue circular markers)

From Figure 6.10, if we only consider the reflections from cross-coupling channel, the capacity barely changes. If we consider both reflections, the capacity drops around 20% when $d = 10\lambda_0$, and almost the same when the distance is further. This drop is less than the capacity drop in Section 6.1.1, meaning that for a near field communication system without good interference suppression, better impedance match is not essential.

7 Conclusion and Future Works

Our research applied a well-developed model to calculate and understand the coupling between two apertures which are in the radiative near field of each other. After studying the coupling we found that incoherent arrays can be used without the need for any interference cancellation over a distance we named the incoherent distance $d_i = \frac{d_{ff}}{2}$. For this thesis, looking at the aperture dimension of $6\lambda_0$, this corresponds to a range of $d \in [10\lambda_0, 30\lambda_0]$. By applying the theoretical results in [16] to our model we found the ideal current distribution that provides the highest coupling between two apertures in the radiative near field. This distribution however, has the prolate spheroidal wave function term, requiring numerical evaluations, and depends on the distance between the apertures. It was therefore found that the Gaussian distribution approximates this prolate spheroidal wave function well. Then, We did a parameter study to find an optimal point at which to fix this distribution that will give high coupling over the entire interested range. We called this the optimized current distribution. The optimized current distribution contains amplitude with -16dB Gaussian taper, and phase distribution with meaning of focusing at $d = 10\lambda_0$. The capacity of this optimized current distribution is almost double than the one of the uniform current distribution.

After finding the optimized current distribution, we designed a lens antenna to synthesize this. The lens design consisted of an elliptical lens to realize the Gaussian amplitude distribution and a hyperbolic lens to realize the phase focussing. The GO current and time-gated CST simulations of this lens are in good agreement with the results of the coupling of the optimized current using the MATLAB code. This brings us to the next step, the FW CST simulation of a MIMO array. We simulated the signal and interference level in the array at three distances which all show a good agreement in terms of coupling and capacity. The capacities of the optimal current, both theoretic and FW CST simulations, share a good agreement. The reason that this current distribution has good performance in terms of capacity over range and bandwidth is that the interference is well suppressed as interference is the dominating term that decreases the channel capacity in an array in the radiative near field. As a result, we designed a MIMO array system which, when operated in the radiative near field , could theoretically provide more than 2 Tbps without applying any signal processing which significantly decreases the complexity of the hardware design.

After designing the array, we studied the sources and the effect of reflections which between the two antennas in the radiative near field to offer some design guidelines.

In this thesis we are not focused on the specific design of a single lens antenna or an array since the application and its corresponding requirements were not yet established. The key purpose is to optimize the capacity between two antenna arrays in the radiative near field through optimizing the current distributions used to model them. The study of their performance and way of realizing these lens antennas provide valuable guidelines for future lens array design.

7.1 Contributions

The contributions of this thesis are as follows:

- Study and design of a realizable aperture current distribution which significantly increases the capacity by maximizing the coupling and minimizing the interference between arrays operating in the incoherent region.
- Lens antenna design which approximates the fields of the ideal aperture current distribution.

- Validation of the results of the MATLAB channel matrix model through full-wave simulations in CST.
- Study of the origin of reflections in a radiative near field communication link and the extent of their effect on capacity.

7.2 Limitations

Although this thesis has provided valuable insights into the near field lens antenna array design, it is important to acknowledge the limitations of our study.

- The design of the elliptical lens antenna shows a significant phase error even though we have a good agreement between the channel matrix model and the FW simulation from CST. This phase error led directly to a loss of 0.5Tbps from the theoretical values when we use the Gaussian focused lens antenna.
- The design of the Gaussian focused lens antenna consists of two separate lenses, and elliptical lens for the amplitude distribution and a hemispherical lens for the phase focusing. This is not the most effective lens design since it is not convenient to assemble it during manufacturing and to use in real applications. Therefore a different way of implementing the phase focusing, must be used.
- In this thesis, the effect of reflections was studied, seeing a significant contribution from the reflections, but did not try to reduce the effect of the reflections.
- When the layout of the array changes, the optimized current distribution in this thesis will not be the optimal one.

7.3 Future Work

To improve the model of the near field coupling we should work to address these limitations. Some logical steps are as follows:

- Shape the lens surface to fix the phase error.
- Integrate the elliptical and the hyperbolic lens to have an integrated lens antenna.
- As introduced in this thesis, we already found that the main reflections are from the lens port, so we can decrease the reflections by improving the impedance match of the lens antenna. Apart from that, since the antenna beam in the near field is collimated, the transmission and reflection in the near field can be modelled as a transmission line.
- Properly design the layout (e.g. exciting the nearby channels with orthogonal polarization) and the number of elements for the array based on different applications.
- Some studies in our research group suggest that the higher-order Gaussian modes could provide better co-coupling and less interference in an the array. We can apply these higher-order Gaussian modes to find the optimized current distribution using the same approach as in this thesis.
- In this thesis we are only using an EM point of view to study the capacity and did not include any signal processing or consider any hardware (e.g. RF chips, duplexing plan, etc.). We can

consider the design as a whole system with signal processing hardware design, and then have the final design.

Bibliography

[1] T. S. Rappaport et al., "Wireless Communications and Applications Above 100 GHz: Opportunities and Challenges for 6G and Beyond," in IEEE Access, vol. 7, pp. 78729-78757, 2019, doi: 10.1109/ACCESS.2019.2921522.

[2] IEEE Standard for High Data Rate Wireless Multi-Media Networks, Amendment 2: 100 Gb/s Wireless Switched Point-to-Point Physical Layer, IEEE Standard 802.15.3d-2017 (Amendment to IEEE Standard 802.15.3-2016), Oct. 2017, pp. 1–55.

[3] J. Kim, S. Jeon, M. Kim, M. Urteaga and J. Jeong, "H-Band Power Amplifier Integrated Circuits Using 250-nm InP HBT Technology," in IEEE Transactions on Terahertz Science and Technology, vol. 5, no. 2, pp. 215-222, March 2015, doi: 10.1109/TTHZ.2014.2387259.

[4] R. Weber, A. Leuther, R. Lozar and H. Massler, "Full H-Band LNA in 35 nm mHEMT Technology with Constant Current Bias Control," 2020 15th European Microwave Integrated Circuits Conference (EuMIC), Utrecht, Netherlands, 2021, pp. 9-12.

[5] A. S. H. Ahmed, U. Soylu, M. Seo, M. Urteaga and M. J. W. Rodwell, "A compact H-band Power Amplifier with High Output Power," 2021 IEEE Radio Frequency Integrated Circuits Symposium (RFIC), Atlanta, GA, USA, 2021, pp. 123-126, doi: 10.1109/RFIC51843.2021.9490426.

[6] D. Müller, A. Tessmann, A. Leuther, T. Zwick and I. Kallfass, "A H-Band vector modulator MMIC for phase-shifting applications," 2015 IEEE MTT-S International Microwave Symposium, Phoenix, AZ, USA, 2015, pp. 1-4, doi: 10.1109/MWSYM.2015.7166927.

[7] Y. Jeon, H. Kim, Y. Jang and J. Jeong, "Design of waveguide-based H-band source module using InP HBT integrated circuits," 2022 IEEE International Symposium on Radio-Frequency Integration Technology (RFIT), Busan, Korea, Republic of, 2022, pp. 154-155, doi: 10.1109/RFIT54256.2022.9882486.

[8] M. Arias Campo et al., "H-Band Quartz-Silicon Leaky-Wave Lens With Air-Bridge Interconnect to GaAs Front-End," in IEEE Transactions on Terahertz Science and Technology, vol. 11, no. 3, pp. 297-309, May 2021, doi: 10.1109/TTHZ.2021.3049640.

[9] K. Medrar et al., "H-Band Substrate-Integrated Discrete-Lens Antenna for High Data Rate Communication Systems," in IEEE Transactions on Antennas and Propagation, vol. 69, no. 7, pp. 3677-3688, July 2021, doi: 10.1109/TAP.2020.3044382.

[10] X. Lu, Y. Chen, S. Guo and S. Yang, "An Electromagnetic-Transparent Cascade Comb Dipole Antenna for Multi-Band Shared-Aperture Base Station Antenna Array," in IEEE Transactions on Antennas and Propagation, vol. 70, no. 4, pp. 2750-2759, April 2022, doi: 10.1109/TAP.2021.3137511.

[11] E. G. Larsson, O. Edfors, F. Tufvesson and T. L. Marzetta, "Massive MIMO for next generation wireless systems," in IEEE Communications Magazine, vol. 52, no. 2, pp. 186-195, February 2014, doi: 10.1109/MCOM.2014.6736761.

[12] Lizhong Zheng and D. N. C. Tse, "Diversity and multiplexing: a fundamental tradeoff in multiple-antenna channels," in IEEE Transactions on Information Theory, vol. 49, no. 5, pp. 1073-1096, May 2003, doi: 10.1109/TIT.2003.810646.

[13] N. Llombart and S. O. Dabironezare, "Feasibility Study of Quasi-Optical MIMO Antennas for Radiative Near-Field Links," in IEEE Transactions on Antennas and Propagation, vol. 70, no. 8, pp. 7073-7083, Aug. 2022, doi: 10.1109/TAP.2022.3168724.

[14] P. H. Siegel, "Terahertz technology," in IEEE Transactions on Microwave Theory and Techniques, vol. 50, no. 3, pp. 910-928, March 2002, doi: 10.1109/22.989974.

[15] O. Edfors and A. J. Johansson, "Is Orbital Angular Momentum (OAM) Based Radio Communication an Unexploited Area?," in IEEE Transactions on Antennas and Propagation, vol. 60, no. 2, pp. 1126-1131, Feb. 2012, doi: 10.1109/TAP.2011.2173142.

[16] G. Borgiotti, "Maximum power transfer between two planar apertures in the Fresnel zone," in IEEE Transactions on Antennas and Propagation, vol. 14, no. 2, pp. 158-163, March 1966, doi: 10.1109/TAP.1966.1138660.

[17] C. E. Shannon, "A mathematical theory of communication," in The Bell System Technical Journal, vol. 27, no. 3, pp. 379-423, July 1948, doi: 10.1002/j.1538-7305.1948.tb01338.x.

[18] R. G. Gallager, Information Theory and Reliable Communication, vol. 2. New York, NY, USA: Springer, 1968.

[19] G. D. Boyd and H. Kogelnik, "Generalized confocal resonator theory," in The Bell System Technical Journal, vol. 41, no. 4, pp. 1347-1369, July 1962, doi: 10.1002/j.1538-7305.1962.tb03281.x.

[20] S. Takeshita, "Power transfer efficiency between focused circular antennas with Gaussian illumination in Fresnel region," in IEEE Transactions on Antennas and Propagation, vol. 16, no. 3, pp. 305-309, May 1968, doi: 10.1109/TAP.1968.1139177.

[21] N. Llombart, G. Chattopadhyay, A. Skalare and I. Mehdi, "Novel Terahertz Antenna Based on a Silicon Lens Fed by a Leaky Wave Enhanced Waveguide," in IEEE Transactions on Antennas and Propagation, vol. 59, no. 6, pp. 2160-2168, June 2011, doi: 10.1109/TAP.2011.2143663.

[22] M. Arias Campo, D. Blanco, S. Bruni, A. Neto and N. Llombart, "On the Use of Fly's Eye Lenses with Leaky-Wave Feeds for Wideband Communications," in IEEE Transactions on Antennas and Propagation, vol. 68, no. 4, pp. 2480-2493, April 2020, doi: 10.1109/TAP.2019.2952474.

[23] S. Bosma, N. van Rooijen, M. Alonso-delPino and N. Llombart, "A Wideband Leaky-Wave Lens Antenna With Annular Corrugations in the Ground Plane," in IEEE Antennas and Wireless Propagation Letters, vol. 21, no. 8, pp. 1649-1653, Aug. 2022, doi: 10.1109/LAWP.2022.3176884.

[24] D. F. Filipovic, S. S. Gearhart and G. M. Rebeiz, "Double-slot antennas on extended hemispherical and elliptical silicon dielectric lenses," in IEEE Transactions on Microwave Theory and Techniques, vol. 41, no. 10, pp. 1738-1749, Oct. 1993, doi: 10.1109/22.247919.

[25] N. T. Nguyen, N. Delhote, M. Ettorre, D. Baillargeat, L. Le Coq and R. Sauleau, "Design and Characterization of 60-GHz Integrated Lens Antennas Fabricated Through Ceramic Stereolithography," in IEEE Transactions on Antennas and Propagation, vol. 58, no. 8, pp. 2757-2762, Aug. 2010, doi: 10.1109/TAP.2010.2050447.

[26] H. Zhang, S. O. Dabironezare, J. J. A. Baselmans, and N. Llombart, “Focal Plane Array of Shaped Quartz Lenses for Wide Field-of-view Sub-millimeter Imaging Systems, ” IEEE Trans. Antennas Propag., 2023, submitted.

[27] H. Zhang, S. O. Dabironezare, G. Carluccio, A. Neto and N. Llombart, "A GO/FO Tool for Analyzing Quasi-Optical Systems in Reception," 2019 44th International Conference on Infrared, Millimeter, and Terahertz Waves (IRMMW-THz), Paris, France, 2019, pp. 1-2, doi: 10.1109/IRMMW-THz.2019.8873950.

[28] H. Zhang, “A GO/FO Tool for Analyzing Quasi-optical Systems in Reception”, http://resolver.tudelft.nl/uuid:997558e6-7f32-493a-9f84-57895636db28

[29] M. Arias Campo, “On the Design of Fly’s Eye Lenses at Sub-THz Frequencies for Wideband Communications”, https://doi.org/10.4233/uuid:a9bb41e0-3d2a-4028-a218-bd85f2053545

Appendix. Square Gaussian Focused Lens Antenna with $\epsilon_r = 6.4$

We design a Gaussian focused lens antenna to approximate the optimized current distribution using elliptical lens material with higher relative permittivity $\epsilon_r = 6.4$. With higher ϵ_r, the beam of the primary field is narrower, and the critical angle is wider, allowing us to truncate the elliptical lens antenna to a square aperture. Adding a hyperbolic lens with a square aperture on top of the elliptical lens antenna, the entire antenna system is shown in Figure 0.1. For our convenience, we will call this antenna as the square Gaussian focused lens antenna.

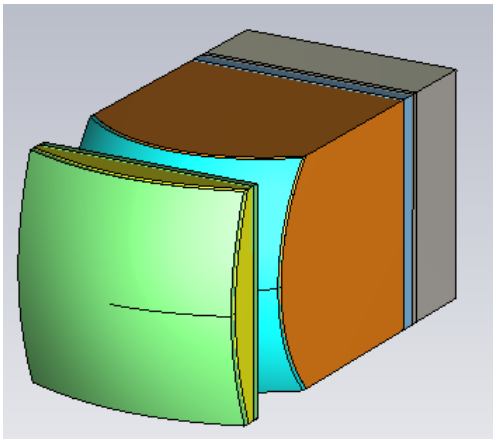

Figure 0.1 The Gaussian focused lens antenna with $\epsilon_r = 6.4$ dielectric in the elliptical lens antenna

This square Gaussian focused lens antenna is the same with the one in Section 4.4 but with different materials, truncations, and parameters. The elliptical lens antenna is still fed by the double-slot iris feed as shown in Figure 4.2 from Section 4.1. The parameters of this antenna are chosen as: $\epsilon_r = 6.4$, $\alpha = 54°$, $\rho_0 = 0.54\lambda_0$, $w = 0.3\lambda_0$, the cavity $h_a = 0.45\lambda_0$, the phase center $\Delta z = -1.8mm$, the diameter of the lens $D = 6\lambda_0$ and the truncation angle $\theta_{max} = 22°$. The meaning of these parameters is introduced in Section 4.4.1. The truncation angle θ_{max} is defined as the truncation angle in the E and H planes, and the truncation angle in other directions is different to truncate a square aperture. The diameter of the lens D_l is the side length, being $6\lambda_0$. We also add a ML on top of the elliptical lens, with relative permittivity of the lens $\epsilon_{rm} = 2.53$ and thickness $h_m = \frac{\lambda_m}{4}$, where λ_m is the wavelength in the ML material.

As for the hyperbolic lens, the parameters are: diameter of the hyperbolic lens $D_h = 6\lambda$, the focal distance $F = 10\lambda$, and the relative permittivity of the lens $\epsilon_{rh} = 2.5$. We also add ML on both sides of the hyperbolic lens, with relative permittivity $\epsilon_{rm} = 1.58$ and thickness $h_m = \frac{\lambda_m}{4}$, where λ_m is the wavelength in the ML material. The hyperbolic lens is assembled op top of the elliptical lens antenna with a distance of one wavelength in free space. Because we already introduced the designing steps in Section 4.4 detail (e.g. GO currents, field radiated by GO currents, etc.), and the differences between this antenna and the antenna in Section 4.4 are only the material and truncation, we will skip the description about the performance of the GO currents and move to CST simulation directly. The description will not be as detailed as in Chapter 4.

This antenna is well impedance matched in the frequency band $f \in [250GHz, 320GHz]$, and the reflection coefficient Γ is shown in Figure 0.2. The simulation of the reflection coefficient of this LW

feed is performed in a time domain solver in CST, the same as what we did in Figure 4.35, but with different parameters.

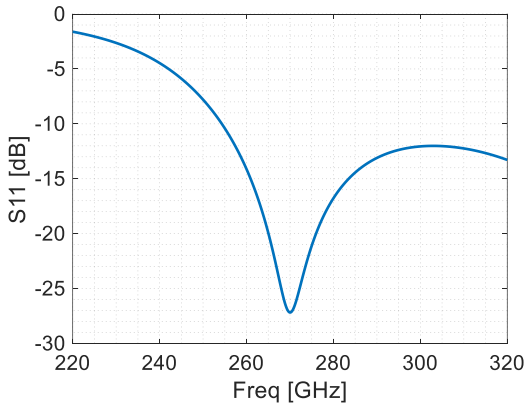

Figure 0.2 The reflection coefficient of the feeding structure

From Figure 0.2, The square Gaussian focused lens antenna is well matched in range $f \in [250GHz, 320GHz,]$, and the reflection coefficient Γ is lowest at 270GHz, around -27 dB.

Then we will plot the current distribution at 270GHz from the CST simulation, and the view of the CST simulation is shown in Figure 0.1. The simulation environment is the same as the one in Section 4.4.3.2 but with different parameters. The current distribution is shown in Figure 0.3.

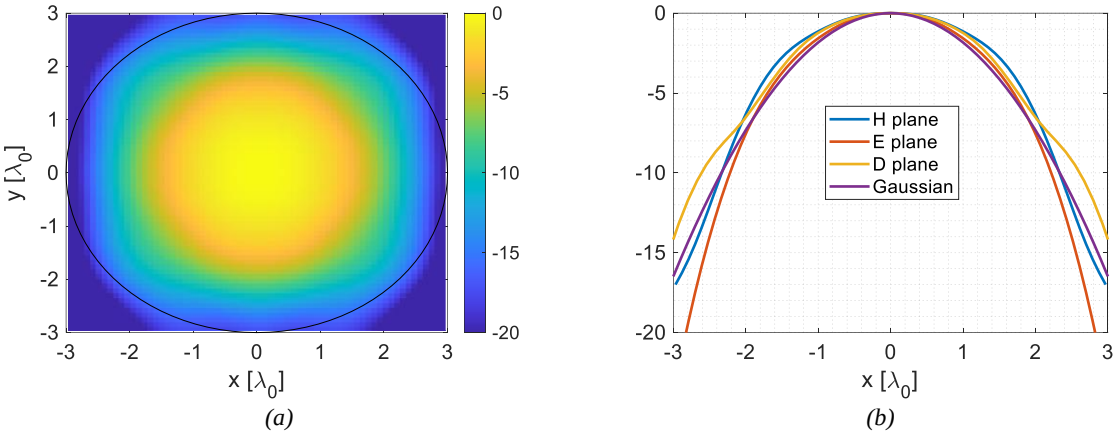

Figure 0.3 The current distribution in (a) 2-D and in (b) H, E and D plane

With this square Gaussian focused lens antenna, we can simulate the MIMO simulation in CST. The view of the MIMO arrays communication in CST is shown in Figure 0.4.

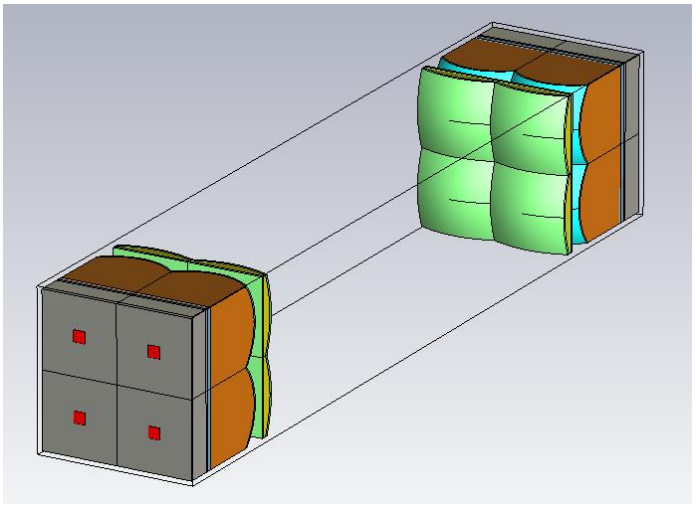

Figure 0.4 The view in CST simulation for MIMO communication

From Figure 0.4, comparing with the array of circular Gaussian focused lens antenna in Figure 5.9, there are no PEC on top of the square array, and the array aperture is filled with four antenna apertures. As introduced in Chapter 6, we need to decrease the reflections.

However, since we use a denser material with relative permittivity $\epsilon_r = 6.4$, it requires more mesh grid for CST to simulate the MIMO coupling in Figure 12.4. Because of this, we cannot simulate Figure 0.4 with our computing resource. To still simulate in CST, we plan to simulate the MIMO coupling with 1×2 arrays. This is because the interference S_{81} is negligible compared with the interference S_{61}, and we can assume this interference as 0. The MIMO coupling with 1×2 arrays are shown in Figure 0.5.

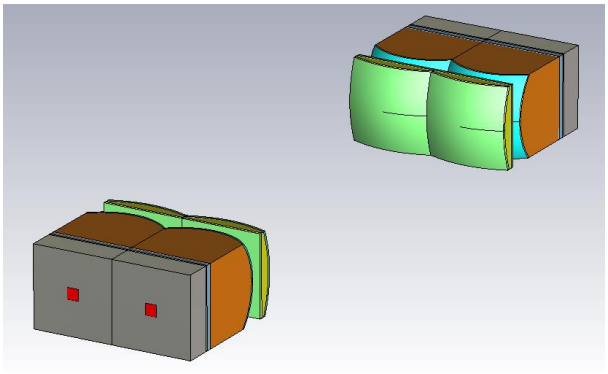

Figure 0.5 The view in CST simulation for 1×2 *MIMO communication*

This directly halves the calculation domain. It also allows us to add a symmetry plane, further halving the calculation domain. In total, the required calculation of Figure 0.5 is one-quarter of the simulation of Figure 0.4. The FW simulation is performed in Time Domain Solver. The background material is filled with vacuum, and the boundary conditions at x, y, and z direction are all set as open (add space). The simulation terminates when the energy in the simulation drops to -40dB compared to the input energy. The frequency band is limited in $f \in [250GHz, 320GHz]$. During the simulation port 1 is excited. From this radiated signal, the coupling to all other apertures is retrieved from CST through the S-parameters. The simulations are performed over three distances, $d = 10\lambda_0, 20\lambda_0, 30\lambda_0$.

The S_{51} and S_{61} of this simulation at three distances before and after TG are shown in Figure 0.6.

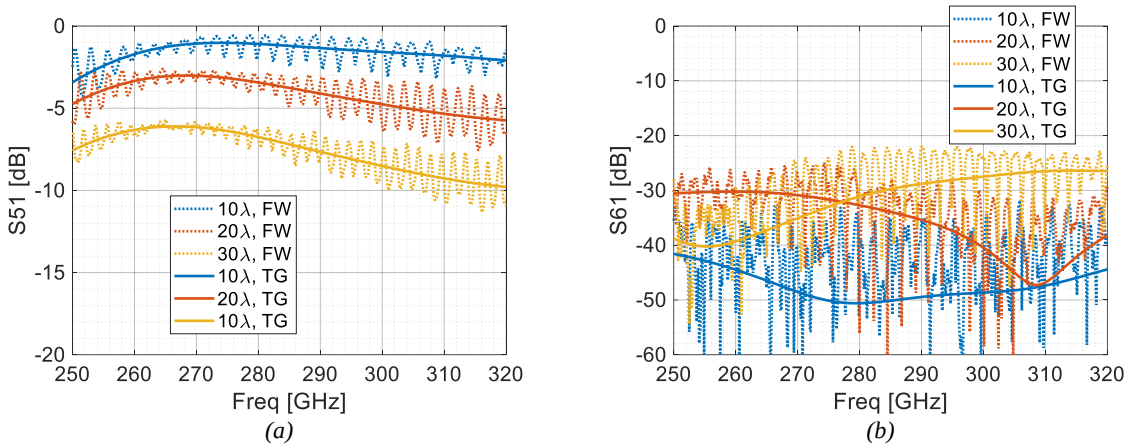

Figure 0.6 The (a) S_{51} and (b) S_{61} of CST simulation in Figure 12.5 for three link distances before (dot line) and after (solid line) time-gating

With the S parameters and the channel matrix, we can apply the same approach introduced in Chapter 5 to calculate the capacity of this antenna with the S parameters. We will compare this capacity with the capacity of the circular Gaussian focused lens antenna in Chapter 5. The capacities are shown in Figure 0.7. the S_{81} for both antenna arrays are set to zero in Figure 0.6.

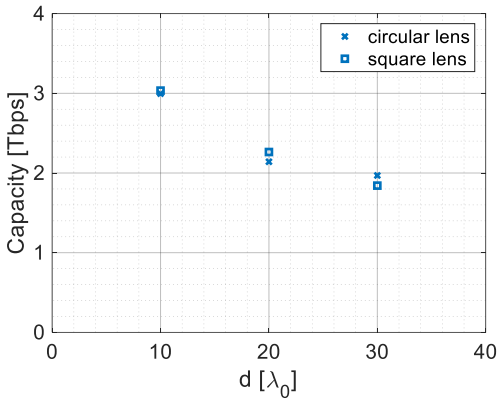

Figure 0.7 The capacities of the MIMO array with S parameters of circular Gaussian focused lens antenna (cross markers) and S parameters of square Gaussian focused lens antenna (square markers)

In Figure 0.7, the capacities of these two antennas are almost the same, showing a good agreement between these two antenna designs. It is important to note that the frequency range we used to calculate the capacity for the circular Gaussian focused lens antenna is [235GHz, 305GHz], and the frequency range for the one for square Gaussian focused lens antenna is [250GHz, 320GHz]. This give use enough confidence to scale our lens antenna to H-band with high accuracy. Another difference is that the reflection coefficient, but the capacities are almost the same. This tells us that the reflection coefficient Γ does not affect the capacity without reflections a lot, and this Γ will only be a problem for the reflection issues.